Helsinki University of Technology Radio Laboratory Publications
Teknillisen korkeakoulun Radiolaboratorion julkaisuja
Espoo, October, 2001 REPORT S 250

METHODS FOR MEASURING RF RADIATION PROPERTIES OF SMALL ANTENNAS

Clemens Icheln

Dissertation for the degree of Doctor of Science in Technology to be presented with due permission for public examination and debate in Auditorium S4 at Helsinki University of Technology (Espoo, Finland) on the 16th of November 2001 at 12 o'clock noon.

Helsinki University of Technology
Department of Electrical and Communications Engineering
Radio Laboratory

Teknillinen korkeakoulu
Sähkö- ja tietoliikennetekniikan osasto
Radiolaboratorio

Distribution:
Helsinki University of Technology
Radio Laboratory
P.O. Box 3000
FIN-02015 HUT
Tel. +358-9-451 2252
Fax. +358-9-451 2152

© Clemens Icheln and Helsinki University of Technology Radio Laboratory

ISBN 951-22- 5666-5
ISSN 1456-3835

Otamedia Oy
Espoo 2001

Preface

The work on which this thesis is based was carried out at the Institute of Digital Communications / Radio Laboratory of Helsinki University of Technology. It has been mainly funded by TEKES and the Academy of Finland. I also received financial support from the Wihuri foundation, from HPY:n Tutkimussäätiö, from Tekniikan Edistämissäätiö, and from Nordisk Forskerutdanningsakademi. I would like to thank all these institutions, and the Radio Laboratory, for making this work possible for me. I am especially thankful for the many ideas and helpful guidance that I got from my supervisor professor Pertti Vainikainen during all my work.

Of course I would also like to thank the staff of the Radio Laboratory, who provided a pleasant and inspiring working atmosphere, in which I got lots of help from my colleagues - let me mention especially Stina, Tommi, Jani, Lorenz, Eino and Lauri - without whom this work would not have been possible.

And finally I want to say thanks for the encouragement I got from my parents during the last years, and for the patience my beloved Anna-Maj showed during all this time.

Espoo, October 11, 2001,

(Clemens Icheln)

Abstract

In this work significant improvements for measurements of the radio-frequency (RF) radiation properties of small antennas have been proposed and investigated. The main focus is on electrically small antennas as used in mobile communications systems. The methods proposed and evaluated in this thesis allow the minimisation of the dimensions of measurement chambers, and the methods also allow pattern measurements with a minimised error from the RF feed cable and thus lower measurement uncertainty.

The first two parts of the work relate to measurements performed in especially small chambers. The aim is to provide an alternative measurement environment to large, fully anechoic chambers in the special case of *small* antenna calibrations. The use of small chambers such as GTEM cells and small anechoic chambers is proposed. Both options have been constructed and investigated by both simulations and measurements. The results show that a GTEM cell allows the reliable measurement of the radiation pattern and 3-dB bandwidth of small antennas with a low directivity and a dynamic range of less than 20 dB. A small anechoic chamber with the largest dimension of 2.5 m was built during the work for this thesis. The results obtained when measuring the 3-D radiation pattern, efficiency and the gain of a small handset antenna in that small anechoic chamber show further that far-field measurements in such a small anechoic chamber does not result in greater measurement uncertainty than results obtained in conventional large anechoic chambers.

Finally, the influence of the RF feed cables on the radiation characteristics of a small antenna under test has been reduced by a novel method. This method is based on a multi-frequency balun that efficiently suppresses the propagation of leakage and parasitic currents on the shielding of the RF feed cable. The effect of the balun has been thoroughly investigated by means of computer simulations and measurements with a prototype. Both the far field and the near field have been analysed to yield a comprehensive set of figures of merit, showing that the presented balun decreases the measurement uncertainty much better than other commonly used measures against cable effects, such as ferrite beads. The balun cannot only be used in radiation-pattern measurements in large or small anechoic chambers, but also in radio-channel measurements, in near-field scans and in Standard Absorption Rate (SAR) measurements.

TABLE OF CONTENTS

List of Symbols

A	aperture
C	capacitance
c_0	speed of light in vacuum
d, D	distance, width
d_{FF}	distance for far-field conditions
E	electric field strength
E_{far}	electric field strength in far field
E_r	radial component of electric field strength
E_θ	theta-component of electric field strength
E_ϕ	phi-component of electric field strength
e_{rel}	relative error
f	frequency
f_{res}	resonance frequency
h, H	height
H	magnetic field strength
G	antenna gain
G_{max}	maximum gain
G_θ	theta-component of antenna gain
G_ϕ	phi-component of antenna gain
I	current
k	wave number
K, K_E	constants
L, l	length
l_a	length of antenna
m	length of RF cable in simulations
n	a constant
P	power
P_{in}	input power
P_{rr}	re-reflected power
$P_{rad,tot}$	total radiated power
r, R	distance, radius

S_{11} reflection coefficient

S_{21} transmission coefficient

t, T thickness, width

w, W thickness, width

x,y,z Cartesian coordinates

ε' (ε_r') real part of the (relative) permittivity

ε" (ε_r") imaginary part of the (relative) permittivity

ε_0 permittivity of free space

δ small variation

Ø diameter

ϕ azimuth angle

λ wavelength

μ' (μ_r') real part of the (relative) permeability

μ" (μ_r")imaginary part of the (relative) permeability

μ_0 permeability of free space

η free-space impedance

ρ, $\rho_{1/2}$ reflection coefficients

θ elevation angle

List of Abbreviations

3-D	Three-Dimensional
AUT	Antenna Under Test
DOA	Direction of Arrival
DUT	Device Under Test
EFIE	Electric Field Integral Equation
EMC	Electromagnetic Compatibility
EPS	Expanded Polystyrene (Styrofoam)
FAC	Fully Anechoic Chamber
FEM	Finite Element Method
GTEM	Gigahertz Transverse Electromagnetic Mode
GSM	Global System for Mobile communications
HP	Horizontal Polarisation
HUT	Helsinki University of Technology
IDC	Institute of Digital Communications
MEG	Mean Effective Gain
MOM	Method of Moments
NRC	Nokia Research Center
RF	Radio Frequency
RMS	Root Mean Square
SAR	Standard Absorption Rate
TEM	Transverse Electromagnetic Mode
VP	Vertical Polarisation
XPD	Cross-Polarisation Discrimination

1. Introduction

The reliable determination of the direction- and frequency-dependent RF-radiation characteristics of small radiating devices is an important research subject in the field of radio engineering. For instance in future mobile communications systems the behaviour of handset antennas has to be determined in order to optimise their performance in their working environment. An antenna can be characterised by several figures: the three-dimensional radiation pattern, the radiation efficiency, and the bandwidth for instance with respect to a given maximum return loss at the input port of the antenna. Usually these characteristics are determined for the antenna mounted on the handset and placed in a free-space environment. However, measuring the radio channel also in the actual propagation environments where mobile handsets are used has become an increasingly important research field [1]. The principle of mean effective gain (MEG) calculations is to weigh the antenna 3-D gain pattern with the 3-D spatial direction of arrival (DOA) distribution of the incident radio waves in the radio channel [2]. The typical frequency range of current and nearest future mobile communications systems covers approximately 0.8 GHz to 5 GHz.

Radiation-pattern measurements during the design of new small antennas for the use in mobile handsets and the final calibration of those antennas require an environment with a well-defined electromagnetic field strength at the position of the antenna under test (AUT). By rotating the AUT around two axes while recording the signal at the port of the antenna, a full 3-D radiation pattern can be obtained. From the 3-D pattern the total radiated power and the directivity of the antenna can be obtained [3, pp. 112-113]. If also the input impedance of the antenna is measured, the efficiency and gain of the antenna can also be derived from the measurements.

To excite a well-defined field at the measurement position, typically a calibrated electromagnetic field source is placed in an environment with practically no reflections from surrounding objects. A fully anechoic chamber (FAC) is such a free-space measurement environment. In a FAC all walls are completely covered by RF absorbing material, and no conducting surfaces are present. Thereby, high field homogeneity of ± 0.5 dB can be obtained over a very wide frequency range. This homogeneity is required by antenna calibration standards [3, pp. 19-20]. In excellent anechoic chambers field homogeneity as good as ± 0.1 dB can be achieved. Hereby, the measurement of the directly transmitted electromagnetic field is possible without considerable interference from reflected fields.

The absorber lining constitutes the main part of the installation costs of anechoic chambers. A typical distance between the antenna under test (AUT) and the measurement antenna is 3 – 5 m, or even more. Distances between the antennas and the walls, as well as between the antennas and the floor and ceiling, are typically 1 – 3 m. The dimensions of anechoic chambers are therefore quite impressive, leading to substantial costs. When performing measurements of small antennas for mobile communications systems alternatives with much smaller dimensions and hence lower installation costs seem preferable. Also in terms of accessibility a small chamber is

preferable, as the choice of a location for instance inside a building may be easier than with a large chamber. Hereby the availability of the test chamber for the antenna designer can clearly be increased, which allows a more flexible design of new, small antennas, which are - unlike large antennas - not usually designed according to well-known rules and solutions, but instead by experimental verifications during every design step, or with several different prototypes. Motivated by this, the feasibility of using especially small chambers in antenna measurements is presented in this thesis, together with limits for their use in terms of dimensions, frequency range and measurements uncertainties. In Chapter 3 the applicability of the Gigahertz Transverse Electromagnetic Mode (GTEM) cell to small-antenna measurements with certain restrictions is verified by several measurements of small antennas. Chapter 4 relates to the feasibility of decreasing the size of small anechoic chambers to table-top size. The chapter contains a theoretical investigation of the effects of bringing measurement antenna and AUT, as well as sidewalls and AUT very close to one another. Furthermore, a small anechoic chamber W × L × H = 2.50 m × 2.50 m × 2.40 m was designed, constructed and evaluated by measurements. Several figures of merit show the feasibility of this small chamber for small-antenna measurements.

In Chapter 5 the special problem of measurement errors caused by RF feed cables attached to small antennas or mobile handsets is covered. RF feed cables typically cause considerable changes in the radiation characteristics of the AUT during measurements of its radiation characteristics, when contrasted to the ideal case of an isolated AUT such as a mobile handset in a user's hand. The problem caused by RF cables is basically independent of the environment and therefore exists both in large and small anechoic chambers. Common ways widely used to solve this problem are contrasted with a multi-frequency current choke, which is presented here as a new, more efficient solution to minimise the measurement uncertainties caused by RF feed cables. The application of the sleeve-like choke resembles the so-called balun that is known from literature and was introduced as a transformer between an unbalanced feed structure and a balanced antenna in [4, pp. 43-25 – 43-27], [5, pp. 217 – 220], and [6, pp. 38 – 40]. The current choke presented here is therefore called balun throughout this work. The mechanisms of the choke/balun are thoroughly investigated with help of computer simulations and measurements. The designs of a single-band and a dual-band balun are presented together with several figures of merit to prove their better performance in antenna measurements when contrasted with widely used ferrite beads.

2. The situation of small-antenna measurements today

The experimental determination of the RF radiation characteristics requires quite different considerations depending on the size of the antenna being measured. Large antennas are characterised for their gain, efficiency, and 3-D radiation pattern typically inside large anechoic chambers or possibly on open area test sites that fulfil certain requirements as to their free-space like characteristics. In the case of (electrically) large antennas we often talk about directive antennas with directivities (or a mainlobe-to-sidelobe ratio) of 10 – 20 dB, or in some cases up to 30 dB. For large antennas the requirements for the measurement environment are considered mainly in the area(s) illuminated by the antenna, which consequently is the only area in which the radiated fields need actually be measured to obtain a comprehensive picture of the relevant radiation properties such as gain and beamwidth. With electrically small antennas the matter is quite different, as we can expect a much lower directivity, and therefore the measurement environment is important in all directions seen from the AUT. The implications this has on measurement set-ups and uncertainties will be discussed in the following but first an overview over the typical methods/environments used for (small) antenna measurements is given.

One of the common alternatives to the far-field measurements is the near-field measurement. Here, the far-field radiation pattern and efficiency of an antenna are determined by probing only the near field on e.g. a planar or on a spherical surface. The use of a spherical array of identical antennas shortens the lengthy scanning process [7]. Nevertheless, near-field measurements require a considerably more complicated measurement and data analysis process to yield far-field data [8], [9] than direct far-field measurements. Planar near-field scans are also performed to evaluate the current distribution on the surface of an antenna [6, pp. 82 – 83], e.g. during its design process. Near-field scans are furthermore performed when the specific absorption rate (SAR) in the user of a mobile handset is measured [10], [11] in order to fulfil consumer-product regulations [12], [13]. When only the bandwidth and efficiency are of interest, the well-known Wheeler Cap method [14] or a single-mode-waveguide measurement environment [15] is sufficient. Wheeler-cap-like measurements require considerably less effort than far-field radiation pattern measurements and yield only a few of the characteristics of an antenna, but they are useful for an initial evaluation during the design process of a new antenna. Another method that yields only a few antenna parameters is the mode-stirred chamber, a multi-mode oversized resonator in which a very large number of waveguide modes enables the measurement antenna to collect the total radiated power from the AUT. Thus, in a mode-stirred chamber the efficiency of an antenna [16], [17], [18] or an antenna diversity system [19] can be determined. Especially for the design of new antennas computer simulations are a useful means to investigate radiation characteristics. Also in SAR evaluations one often reverts to computer simulations for estimating the SAR value of a mobile phone [11]. However, in order to determine all the relevant radiation characteristics of small antennas accurately, far-field measurements are typically performed as a final step.

If the influence of the user's body on the radiation of a mobile handset needs to be taken into account, phantom heads, hands and torsos are available to simulate the user during a measurement. A statistical approach with several real test-persons is sometimes preferred as it was noted in [20] that for different test-persons variations in the mean effective gain (MEG) of up to 10 dB can be encountered. The above-mentioned waveguide-like measurement environments are not suitable for this kind of large, lossy AUT; instead, near/far-field measurements are required in this case. One exception is the measurement of the total radiated power in the mode-stirred chamber, which allows the calibration of the multi-resonant chamber for the presence of lossy material [16], [17], [18].

If we now look at far-field measurements with the electrically small complex platform of a small antenna mounted on a mobile handset the matter is quite different than with large antennas, i.e. when the overall size of an antenna is a wavelength or less. In this case no distinct main beam exists, and the radiation pattern generally contains no narrow lobes [21, p. 203]. The dynamic range of the radiation pattern is typically not more than 10 – 20 dB when the maximum dimension of the DUT is smaller than $\lambda/2$. Therefore, the measurement environment is important in all directions seen from the antenna under test. Additionally, the fact that in 3-D measurements the DUT needs to be rotated makes the cable placement even more critical. This leads to two major problems in whichever measurement environment used. Firstly, positioners - needed for the automated rotation of the antenna in the external field - become considerable scatterers when they are exposed to the almost omnidirectional fields of the DUT, no matter which way the DUT is mounted. Most positioners in anechoic chambers are additionally sized large enough to hold also large antennas and therefore present an even more massive obstruction for the radiated fields. Additionally the proximity of the DUT to the positioner and its usually massive cover of lossy, RF absorbing material may even pose a source of reactive near-field interaction that is most undesirable in radiation measurements as it affects the far-field pattern considerably. There are however approaches that provide a very well hidden positioner (i.e. motor), namely if the elevation scan is performed by a moving measurement antenna or a fixed array of antennas, following a half sphere around the DUT, which itself is merely rotated in azimuth direction. This set-up allows mechanically much more easily the (vertical) separation of the DUT and its positioner [22].

The second, more persistent problem with small (handset) antennas, both in near-field and far-field measurements, is the cabling needed to connect the antenna to a signal generator, or a network analyser in order to obtain the complex transmission coefficient between the antennas. Usually, the reflection coefficient at the input port of the antenna(s) is recorded, too. The RF feed cables can cause considerable changes in the input impedance measured at the port of the antenna, in the surface-current distribution on the DUT, and in the radiation characteristics of the DUT when contrasted with the case of the DUT ideally floating in free-space, or with the standard mode of operation where the mobile handset is operated by its own internal transceiver, possibly being held by the user's hand. Due to their small size in wavelengths mobile handsets are typically quite omnidirectional as mentioned above. Thus, a measurement RF cable attached to the DUT in whichever way may always be in a relevant direction and hereby affect the characteristics of the DUT. The fact that

in 3-D measurements the DUT needs to be rotated makes the cable placement even more critical. Furthermore, owing to the RF cable attached to the handset antenna the measurement set-up does not resemble the standard mode of operation, i.e. the mobile handset operated by its own internal transceiver, possibly being held by the user's hand. This is especially relevant as antennas used in portable handsets are operated with the chassis of the handset acting as a ground reference without resembling an infinite ground plane that would form a perfect mirror image of the antenna. Actually, a handset with a monopole or patch antenna can be considered to consist of typically two distinct radiating structures or current distributions: the antenna element with confined current distribution, and the phone chassis resembling a thick dipole and supporting the respective current distribution [23], [24]. This makes the surface currents on the chassis especially sensitive to conducting extensions like an RF cable.

Two mechanisms can be noted to cause the errors in the measured radiation pattern or antenna gain, namely owing to the outer shield of the RF cable acting as:

a) a secondary radiator driven by surface currents leaking from the conducting surface of the handset (Fig. 1), and
b) a passive conducting scatterer/reflector, that re-radiates part of the transmitted electromagnetic fields.

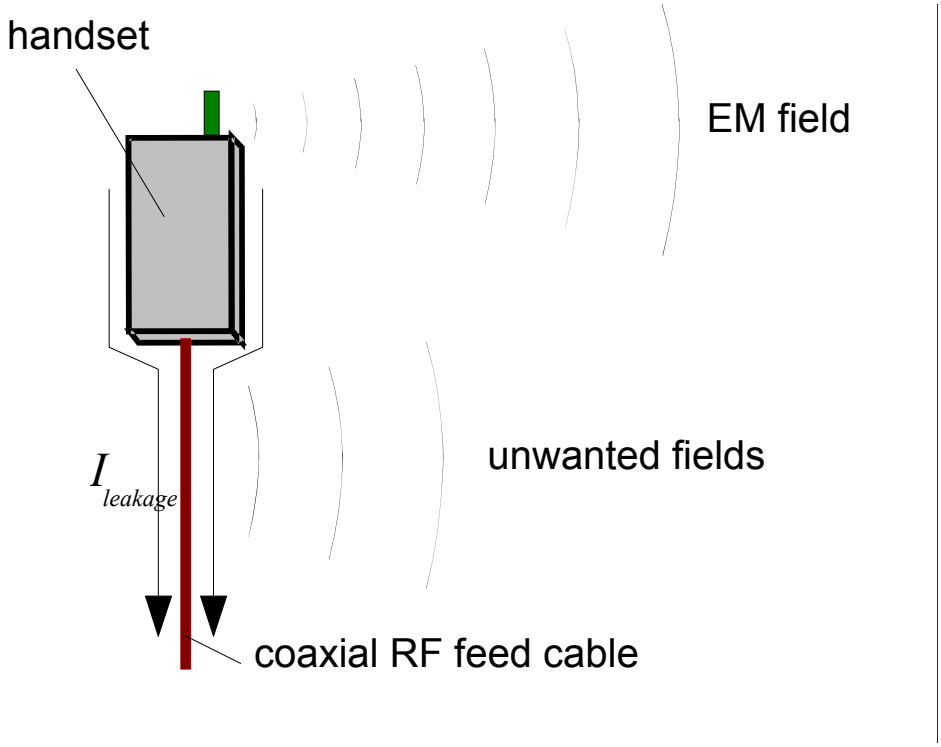

Fig. 1: Illustration of influence of RF feed cable on radiated fields of AUT

It was found in [25], [26] that a feed cable (vertically positioned) introduces errors of up to 10 dB in the measured radiation characteristics of large antennas with vertical polarisation. This can be mainly accounted to the passive scattering. Several ferrite chokes around the cables absorb much of the energy approaching the cable (while reflecting some of it) and hereby reduce the cable-related effect significantly. Also in

measurements of small antennas ferrite chokes are commonly used, which may be better than leaving the RF cable as is, but for the following reasons ferrites should not be considered an ideal solution: Due to the typical low directivity of small antennas, the leakage currents on the RF cable become at least as relevant as cable reflections [27]. These surface currents on the RF cable shield are partly reflected but also absorbed by the ferrite chokes. At certain frequencies, depending on dimensions and material properties, ferrite beads even act as resonators [28]. This considerably affects the total radiated power of the antenna when contrasted with the standard mode of operation. Consequently, the current drain that the choke represents perturbs the current distribution on the surface of the handset on which the antenna is mounted, and thus the radiation pattern is affected. Since the mean effective gain (MEG) has gained increasing attention lately, the effect of the radiation pattern on the MEG in antenna performance of mobile handsets has also been studied [29]. As in the MEG calculation certain parts of the 3-D gain pattern can get emphasized, an accurate, undistorted gain pattern can be of even greater importance than in the calculation of the traditional radiation efficiency.

Other solutions for free-space measurements are based on a set-up free of electrical feed cables. Placing a free-running miniature transmitter inside the DUT, or using the internal transceiver in case of a functional mobile handset [17], can achieve this. As the phase of the transmitter cannot be synchronised this set-up allows only field-amplitude measurements. In order to retrieve the phase information the fields have to be measured either in two separate surfaces consecutively [30], or with two probes simultaneously [31], and a near-field to far-field transformation is required. Also, the input impedance of the antenna cannot be measured with the internal transmitter.

A more sophisticated approach is the use of an optical link connecting the AUT to the measurement equipment through an electrically almost invisible glass fibre [32], [33], [34], and [35]. This measurement approach requires a miniature electro-optical coupler inside the handset. For return-loss measurements the electroabsorption transceiver seems like a promising device [36], as it is quite compact and a full-duplex device. The miniaturisation of the electro-optical system is a very challenging task, as it has to keep up with the decreasing size of modern and future mobile handsets, which might in the nearest future even be built into a watch-like device. Furthermore, temperature stability, power ratings as well as the dynamic range of optical systems do not always fulfil the requirements of small-antenna measurements or especially radio-channel measurements. Thus, even though in some small-antenna measurements optical systems may be a useful alternative, in many cases the use of conventional RF cables is the preferred method, provided the cable problem is minimised.

The big advantage of the use of several sleeve-like chokes along the feed cable in order to decrease its scattering area was first mentioned in [37], where also the typical bandwidth of 10 % was stated. The ability of a quarter-wave sleeve placed on the antenna feed cable close to the handset, to stop the surface currents from accessing the feed-cable surface at the connection to the handset was utilised in [38] in input-impedance measurements over a very narrow band (1%). In both cases the functionality of the balun was not investigated further. Only in [39] and [40] the

balun was thoroughly investigated and its design optimised for its usability in radiation measurements of mobile handsets. As opposed to ferrite chokes the balun is lossless. Although it is band-limited the balun is a valuable means to reduce the effect that the leakage currents along the RF cable have on the antenna radiation. Current and future mobile handsets operate at two or more frequency bands. Measuring the radiation characteristics of the multiple-band antenna by conveniently performing one wide frequency sweep requires multi-frequency baluns as were introduced in [41]. The usefulness of the dual-band balun in measurements of the far-field pattern and in near-field/SAR measurements was shown. The balun is also compared with the commonly used ferrite beads, and it is shown that the balun provides a new improved means to significantly decrease uncertainty in small-antenna measurements. The balun in combination with the use of small measurement chambers like the GTEM-cell or small anechoic chambers may in future be considered a useful measurement set-up for quick and inexpensive, yet reliable and accurate, measurements of the far field or the near field of small antennas.

3. GTEM cell and small antenna measurements

When performing measurements of small antennas, a measurement environment with much smaller dimensions than that of a standard anechoic chamber seems preferable. Not only in term of installation costs, but more importantly in terms of accessibility smaller chambers are preferable. By using unconventionally small measurement chambers it would be possible to perform quick measurements of small antenna characteristics in decentralised, or eventually even portable, table-top sized measurement environments situated close to the developers of new antennas. Hereby, faster assessment of the behaviour of e.g. the mobile handset in operation would be possible. The need for this faster assessment lies in the design process of small antennas, which is quite different from their larger counterparts. To design large antennas typically well-known reference book approaches are used. For the complex platform of a small antenna mounted on a mobile handset on the other hand no such standard design approaches are available. Therefore, small antennas are often not conceptionalised on the drawing board but instead by experimental methods, optimising the antenna performance with help of computer simulations or several measurements of proto-types. Here, the importance of having an easily accessible, easily available, and yet reliable measurement environment is becoming more important. In this chapter the usability of a 2.1 m long GTEM-cell in antenna measurements is evaluated.

3.1. The GTEM-cell

The principle of the GTEM cell is the generation of a uniform electric field inside a shielded environment by operating an expanded transmission line in the TEM mode. At the narrow end of the cell a standard coaxial connector provides a port to the transmission line. From that the transmission line is transformed into a flared rectangular coaxial line (see Fig. 2). At the wide end of the cell a wideband termination section matches the TEM mode over the frequency range of the cell. The flared shape of the GTEM cell and its wideband termination section ensure that no resonances disturb the uniformity of the field in the testing volume, which is situated under the center conductor near the termination section. The size of the equipment that can be measured inside a GTEM cell is typically less than a tenth of the size of the cell itself. In EMC measurements the GTEM cell is accepted as a sufficient tool for radiated susceptibility tests, as well as for measurements of radiated emissions. From this the idea arose to use the GTEM cell to characterise small antennas. This is however not an obvious procedure, as the requirements for the field homogeneity in EMC tests are less stringent (± 3 – 4 dB) than in antenna measurements (± 0.1 – 0.5 dB). Furthermore, one would expect a strong influence of the metal cell walls on the radiation characteristics of the antenna, as well as - possibly multiple - reflections that would affect the measured radiation pattern. In [42] it was shown that these effects are negligible in a conventional TEM cell. According to [43] the gain of an antenna can be measured in a GTEM cell with an average accuracy of better than ± 1 dB. Both articles also mention that reciprocity is fulfilled, i.e., the antenna under test may be used as the transmitter or receiver without changing the result. So in this part of this thesis the possible application of a GTEM cell to small antenna measurements was more thoroughly evaluated. Test

measurements of radiation patterns with several small antennas were carried out and compared to reference measurements. The analysis focuses on the dynamic range of the GTEM cell, as well as on the isolation properties between co- and crosspolarisation. Field probe measurements were used to analyse the field homogeneity inside the GTEM cell.

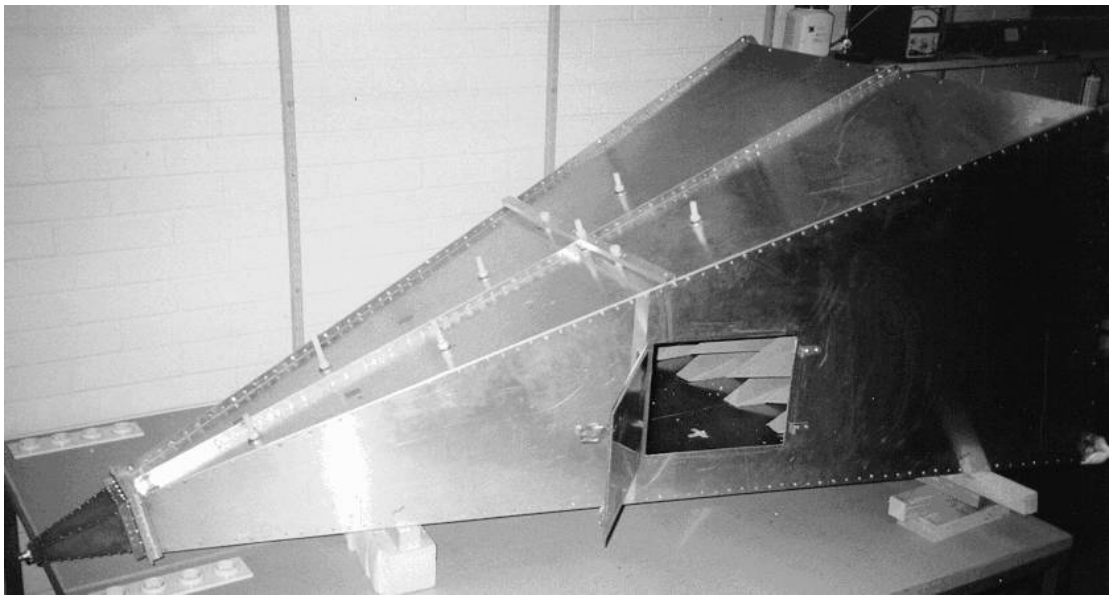

Figure 2: The GTEM cell at the Radio Laboratory of HUT, as used in the antenna measurements. The coaxial input port is at the tip (in bottom left corner of this picture).

3.2. Measurements of field patterns of moderately directive narrow-band patch antennas

The radiation patterns of three small patch antennas and a small helix antenna were measured at frequencies between 0.9 and 3.8 GHz. The set-up of the antenna measurement inside the GTEM cell is described in Fig. 3. A vector network analyser was used to record the transmission coefficient (S_{21}) between the input port of the GTEM cell and the input port of the antenna as a function of frequency and rotation angle.

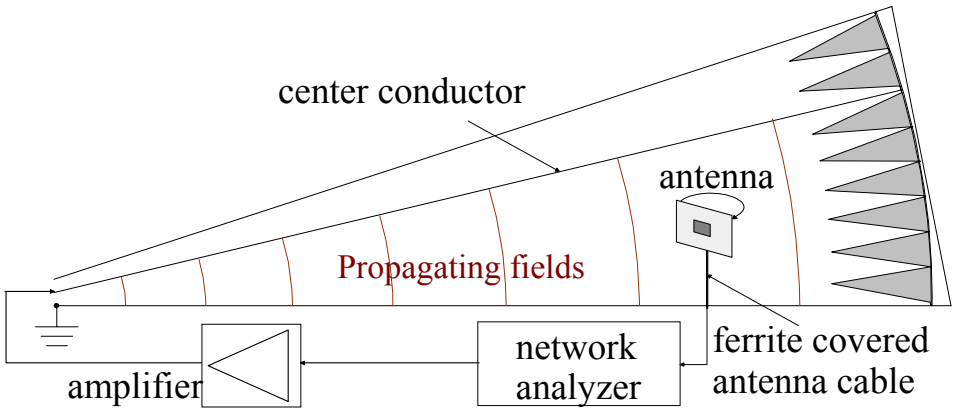

Figure 3: Antenna measurement set-up inside GTEM cell.

The radiation pattern of a small λ/2 patch antenna (Fig. 4a) was measured at 3.76 GHz in the GTEM cell and for comparison in a fully anechoic chamber. At that frequency the reflection coefficient of the termination section of the GTEM cell is about -19 dB (see Fig. 5). A good correspondence of the main lobe patterns can be seen (see Fig. 6) and the 3 dB beamwidth can be determined. However, the minima and the back lobe region suffered from the limited dynamic range of the GTEM cell. In this case a maximum front to backlobe ratio of only around 20 dB could be measured. Next, the radiation pattern of a λ/4 patch antenna (Fig. 4b) was measured at 1.92 GHz where the reflection coefficient of the cell is -21.5 dB. As seen in Fig. 7, the main beam shape is reproduced quite well and the front to backlobe ratio of around 20 dB can be determined. Finally, the radiation pattern of a small helix antenna [45] was measured. The 30 mm long antenna was mounted on a metal case with the shape and size of a mobile phone, i.e. 140 × 40 × 15 mm^3. It was rotated in one of its elevation planes. The measurement was performed at 900 MHz where the reflection coefficient of the cell is about -34 dB. The typical characteristics of a mounted antenna can be seen (Fig. 8), i.e. two slightly downwards directed lobes and a minimum at 180°. However, the interferences from the two lobes and their reflections form the termination section of the GTEM cell prevent the accurate recovering of the exact radiation pattern in this case.

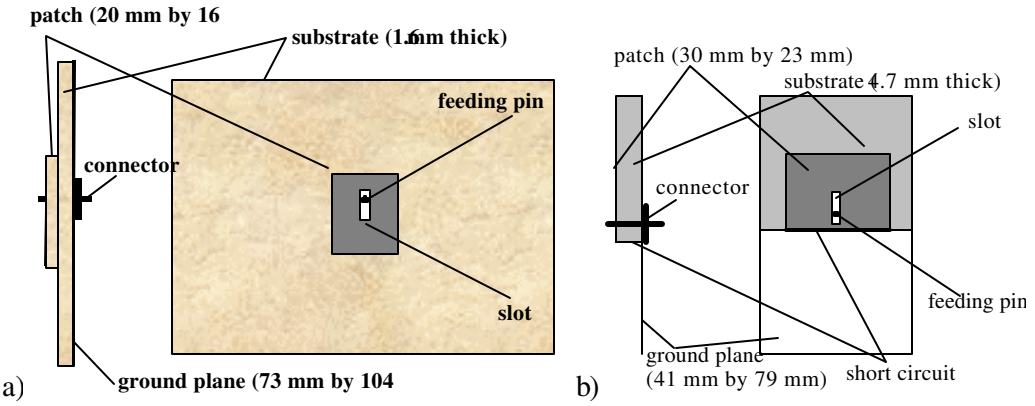

Figure 4: The two experimental patch antennas used in the measurements, a) a λ/2 patch antenna f_{res} = 3.76 GHz and b) a λ/4 patch antenna [46] f_{res} = 1.92 GHz.

The presented results show, that the shape of the main lobe of small antennas can be measured quite accurately without further calibration of the GTEM cell. Thereby e.g. the 3-dB bandwidth of the antennas could be determined quite accurately. However, the minima and the back lobe region suffered from the limited dynamic range of the cell, i.e. a front to back lobe ratio of only 20 dB could be measured. The power reflection coefficient of the termination of the cell is about –20 dB (Fig. 5). So, when the main lobe is directed towards the back of the cell, and the directivity of the antenna is in the area of 20 dB or more, the interference between direct and reflected field is dominant and the information about the back lobe level can not be recovered.

Another limitation in the usability of this moderately large GTEM cell (length: 2.1 m) became apparent during the helix antenna measurement, i.e. equipment with the size of a larger mobile phone (~150 mm long) could not be rotated around all the axes

without affecting the field homogeneity inside the testing volume. The GTEM cell of this moderate size can therefore not replace the anechoic room to obtain a complete 3-dimensional radiation pattern for mounted mobile-handset antennas. With a larger GTEM cell one would lose the size advantage of the GTEM cell. However, since the overall length of current and future mobile terminals is often clearly below 100 mm, also due to integration of the antenna, this limitation is negligible in many cases.

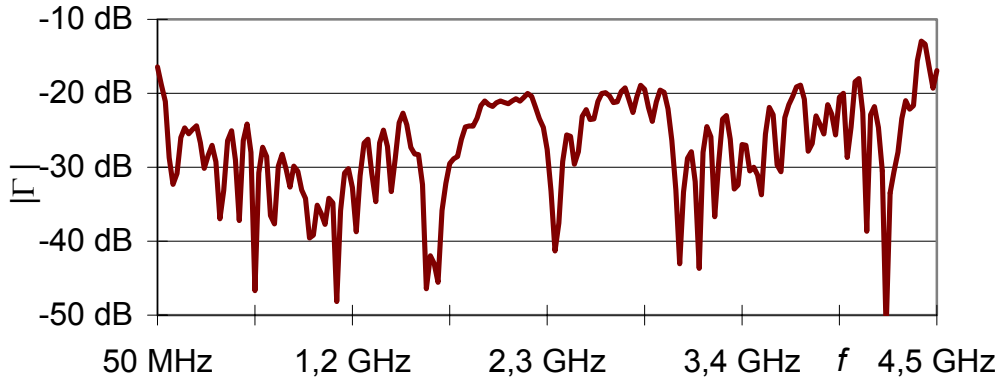

Figure 5: Magnitude of the reflection coefficient Γ of the termination section in the GTEM cell.

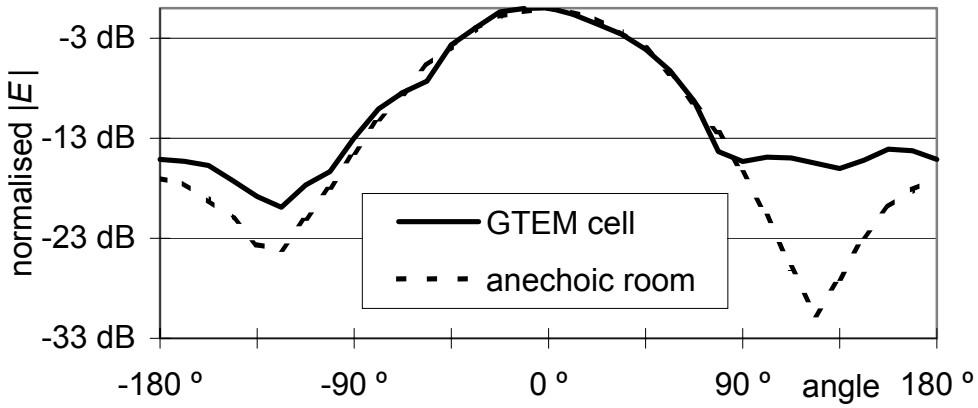

Figure 6: Normalised field strength in the *H*-plane radiation pattern of a λ/2 patch antenna at 3.76 GHz [44].

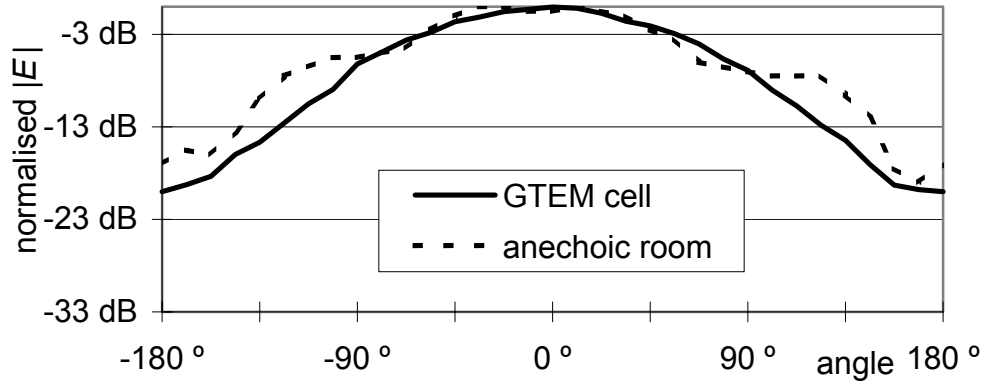

Figure 7: Normalised field strength in the *H*-plane radiation pattern of a λ/4 patch antenna at 1.92 GHz [44].

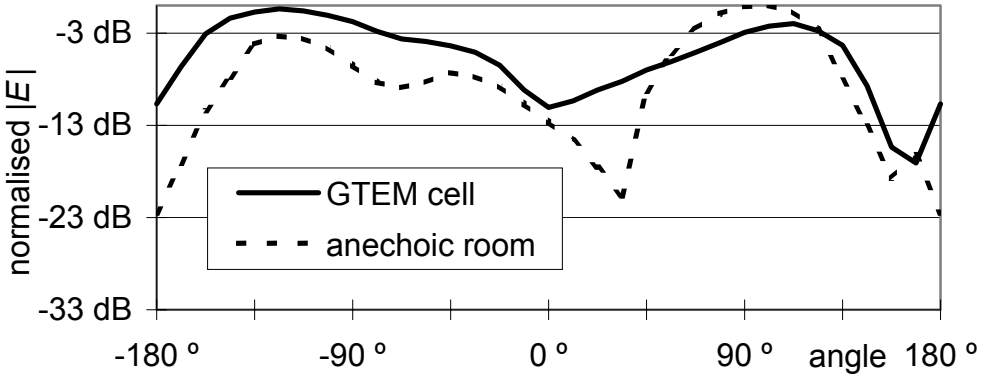

Figure 8: Normalised field strength in the elevation plane radiation pattern of a helix antenna on a metal case at 900 MHz (0 ° is towards zenith) [44].

3.3. Measurements of antennas with special characteristics in their radiation pattern

The results obtained in the measurements with a modified patch antenna that contained two parallel parasitic patches proved the good isolation of the GTEM cell between co- and crosspolarisation, which is an important factor in measurements of mobile phone antennas. The coplanar triple-patch antenna used at 1.6 – 2 GHz is shown in Fig. 9.

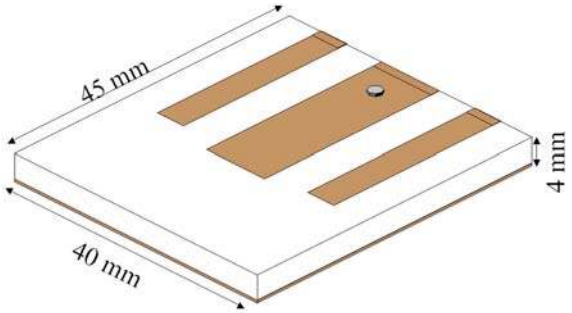

Figure 9: Triple-patch used in measurements at 1.6 – 2 GHz, with one active patch in the centre and two parasitic patches.

The parasitic patches of the antenna cause the radiation to turn the polarisation as a function of frequency, i.e. at around 1.82 – 1.83 GHz the horizontally polarised fields are stronger than the vertically polarised fields. The band with the dominant horizontal polarisation could clearly be determined in the GTEM cell (see Fig. 10). The measurements in the GTEM cell and in a FAC were made comparable by doing a parallel reference measurement with a monopole probe in both GTEM cell and anechoic chamber. The difference of the two curves obtained from the monopole in GTEM cell and FAC, was added to the patch antenna curve that was measured in the GTEM. Hereby, the frequency response of the GTEM cell was partly compensated.

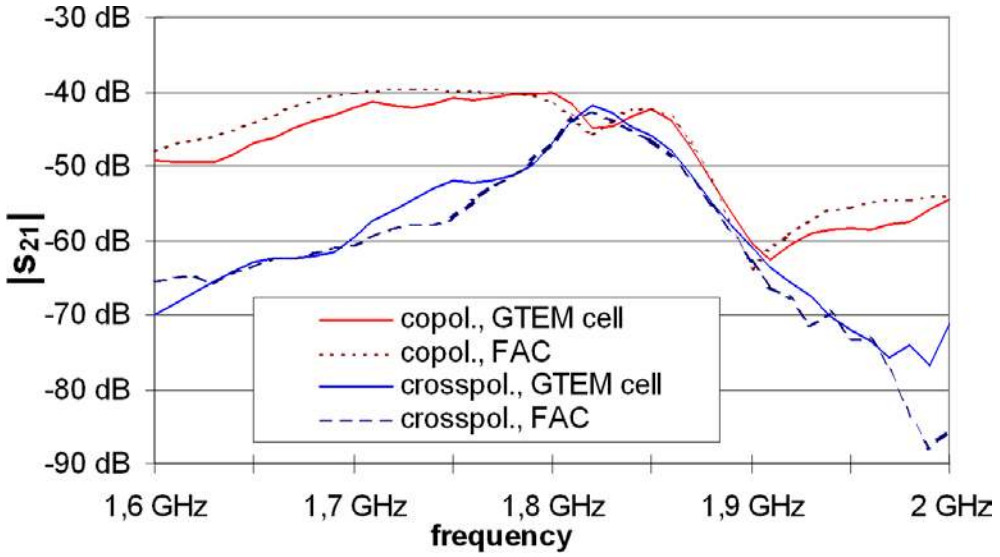

Figure 10: Comparison of the co-polarised and cross-polarised E-field of the triple-patch antenna in the GTEM cell (solid) and in the fully anechoic chamber of IDC (dotted, dashed).

3.4. Field uniformity in the testing volume at frequencies above 1 GHz

The field homogeneity of an antenna test site is an important factor in the evaluation of a measurement site. Therefore, measurements of the field homogeneity in the testing volume of the 2.1 m long GTEM cell at IRC (Fig. 2) were performed. The vertical field strength at the centre of the testing volume and the field strength at positions towards the sidewalls of the cell were measured with a vertical monopole probe place consecutively on five feed-throughs in the bottom wall of the GTEM cell (see Fig. 11). An increasing field inhomogeneity of more than ±1 dB can be seen at frequencies above 2 GHz (Fig. 12).

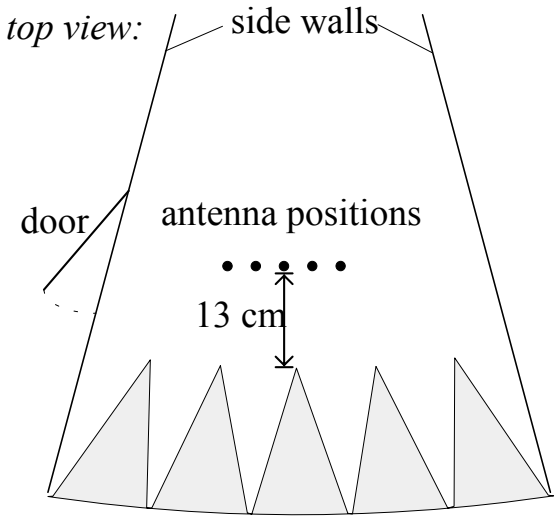

Figure 11: Measurement set-up when determining the field homogeneity inside the test volume of the GTEM cell.

Reflections from the termination of the cell, as well as higher order modes excited by the objects inside the GTEM cell [47], are reasons for the field fluctuations in the testing area. In the GTEM cell used in these measurements the test volume is situated 1.3 m from the input port of the cell. At this position the height between centre conductor and bottom wall is 390 mm. In this case, at 1 GHz theoretically $^1/_3$ of the power in the testing volume propagates in higher order waveguide modes (see Fig. 13). These higher order modes deteriorate the field homogeneity inside the testing volume. When the antenna is the transmitter, the position of the antenna has an influence on which higher order modes are excited. For a patch antenna this means that different areas of the antenna surface couple to different modes. Furthermore, the higher order modes cannot propagate all the way to the input port of the cell, as the decreasing cross sectional dimensions of the waveguide raise the cut-off frequency continuously until only the TEM mode can propagate further. The energy is partly transferred back into lower modes and finally reaches the port in the TEM mode, or it is reflected back towards the termination of the cell. This loss of energy that is not measured at the port of the cell affects the measurements. The amount of energy in the cell that may be propagating in higher order modes increases with frequency. This fact limits the useful frequency range for the desired application of the GTEM cell.

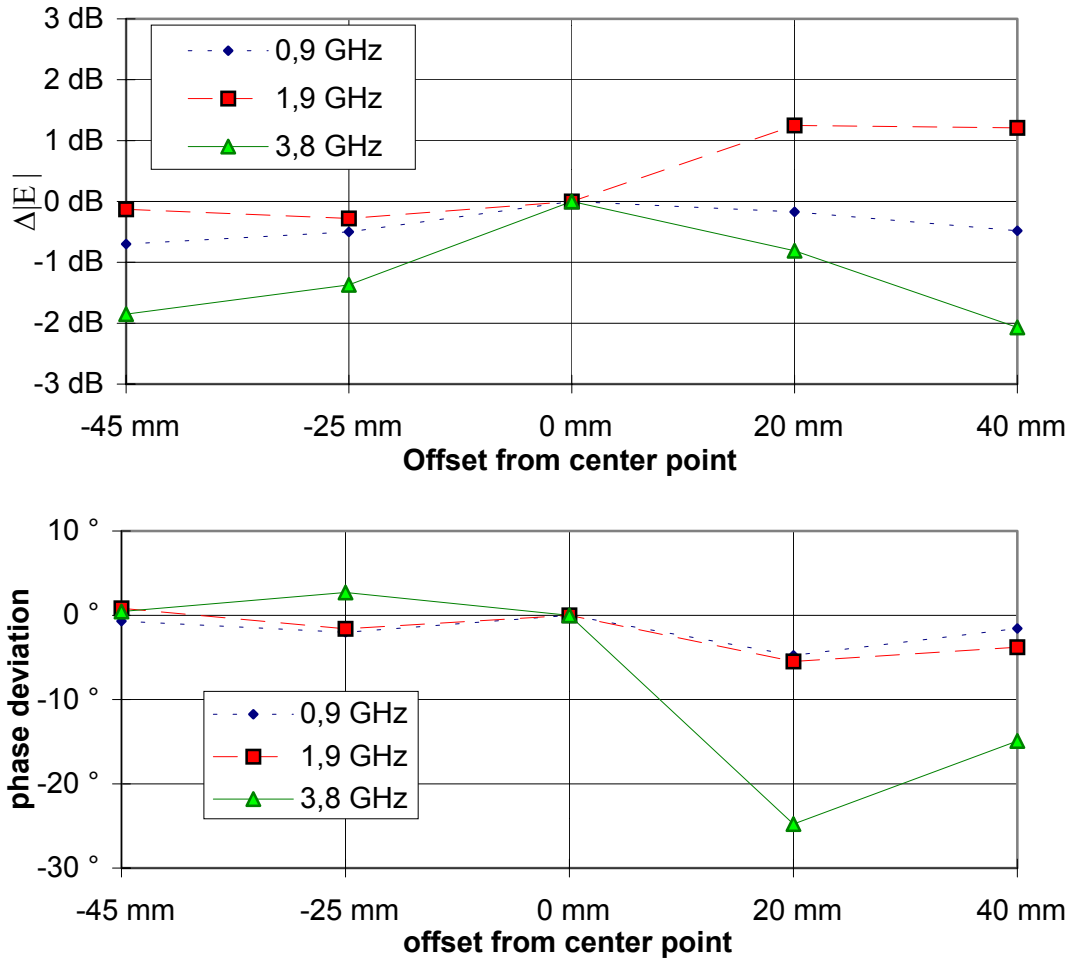

Figure 12: Measured E-field and phase variations along a line perpendicular to the longitudinal axis of the GTEM cell. Field strength and phase were normalised to the centre point of the test volume.

At 0.9 GHz the measured field homogeneity seen in Fig. 12 is good enough for the measurements of small e.g. patch antennas or complete mobile handsets. For such small antennas one can furthermore expect a directivity less than 20 dB so the limited dynamic range of the cell discussed above is not an obstacle. However, with an increased field inhomogeneity in the cell and a more directive behaviour of a small antenna, measurements at 1.9 GHz have to be analysed carefully, and above 2 GHz the 2.1 m long GTEM cell does not appear to be a suitable device for antenna measurements. This fact is not likely to change with a different overall size of the GTEM cell. A larger cross section will only increase the probability of higher order modes, while a smaller cross section will impose a too small limit to the size of the measurable antenna. As a point of reference, the nominal testing volume inside the 2.1 m long GTEM cell is about 130 mm high and a typical mobile handset is about 90 - 110 mm long.

At frequencies below 0.9 GHz, where e.g. some pager systems operate, one can expect the field homogeneity inside the GTEM cell not to be distorted more than seen at 0.9 GHz. Rather in the opposite, as the cut-off frequencies of the higher order modes are beyond these low frequencies. However, at lower frequencies the quality of the wideband termination has to be taken into consideration, because the radiation termination by the RF absorbers becomes less effective at lower frequencies. This effect can be expected to be considerable only below 400 – 500 MHz for cases where medium sized or large RF absorbers are used for the termination [48]. So, already a medium sized GTEM is a useful tool for small-antenna measurements from about 400 – 2000 MHz.

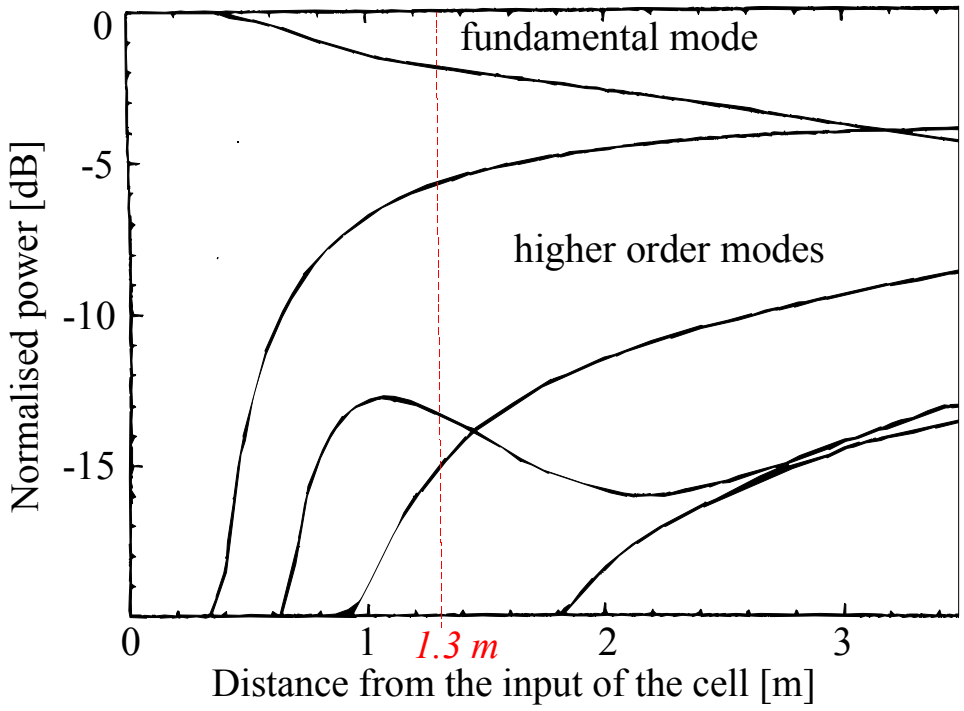

Figure 13: Power distribution in fundamental and higher order modes in a GTEM cell at 1 GHz [47].

3.5. Antenna efficiency measurements in a GTEM cell

In Chapter 2 several measurement techniques were described that yield the radiation efficiency of an antenna. In the case of mobile handset antenna often the efficiency of a handset together with a human head model is needed, which cannot be achieved in the conventional Wheeler Cap method [14] or a single-mode-waveguide measurement environment [15]. The size of the radiating object must be small enough to fit into the cap or waveguide, which again is sizewise limited by the first cavity or waveguide resonance, respectively. Also, the inclusion of a lossy body like the phantom head would violate the concept of the Wheeler Cap.

Alternatively, during the last years reverberating chambers have been increasingly used for efficiency measurements. As opposed to the Wheeler Cap the principle of reverberating chambers builds on the existence of cavity resonances as a means of averaging the radiated power. Therefore the chamber and the AUT are not limited in size. The inclusion of lossy material in the measured object is possible [16], [17], [18] but not unproblematic, as the resonances change and thus the calibration of the empty cell becomes inaccurate. The use of TEM cells for total radiated power measurements has been presented in [51]. Generally, the use of waveguides overcomes the limitation of the Wheeler Cap method in terms of size of the antenna, as well as the limitation of the reverberating chamber in terms of including lossy material. This is due to the fact that waveguide measurements rely on actually measuring the radiation itself and integrating the 3-D patterns to obtain the total radiated power. Even if it involves the time consuming measurement of the 3-D radiation pattern, the use of GTEM cells in efficiency measurements of small antennas seems like a very promising alternative to measurements in large anechoic chambers. In order to be able to include a head model in the measurement the size of the GTEM cell might have to be increased with all the consequences mentioned in Section 3.3, but this would still provide a less expensive environment than a fully anechoic chamber.

4. Small anechoic chambers and the characterisation of small antennas and mobile handsets

Because of the limitations mentioned in the previous chapter affecting the usability of the GTEM-cell in antenna measurements, an alternative measurement environment also with small dimensions is considered. In this chapter the feasibility of drastically decreasing the dimensions of commonly used fully anechoic chambers is investigated for the use of small-antenna measurements at around 1 – 3 GHz. This will allow a more flexible design of new, small antennas, which are - unlike large antennas - usually designed by experimental verifications during every design step, or with several different prototypes.

Table-top sized anechoic chambers can be implemented in a straight-forward manner at frequencies of several GHz, where the wavelength is only of the order of 10 – 50 mm. Such an anechoic chamber, even movable, was designed. e.g. in [52]. With dimensions as small as $2.25 \times 1.2 \times 1.2$ m^3, the chamber that was designed for the frequency range above 18 GHz showed good results in antenna measurements. However, at RF frequencies with wavelengths of 100 – 500 mm the feasibility of such a small chamber is not obvious since the dimensions of the room are much closer to the order of the wavelength. The limitations in using small anechoic chambers for antenna measurements are discussed in this chapter. Limits for the distance between the measurement antenna and the DUT, as well as for the distance between the RF absorbers and the DUT ([49], [50]) are given in Sections 4.1 and 4.2, respectively. In Section 4.3 the design and construction of a small anechoic chamber at IDC is described, and field homogeneity measurements as well as radiation pattern measurements of a small antenna are performed to evaluate and document the good performance of the described chamber in comparison with standard large anechoic chambers.

4.1. Effect of the small distance between the antennas

The minimum possible distance between the AUT and the measurement antenna is an important factor that will yield a lower limit for the size of an anechoic chamber. This minimum measurement distance depends on several factors.

First of all a certain minimum desired ratio between the far field and the near field of the AUT should be defined. This ratio can be calculated e.g. for a single electric dipole directly as a function of distance. The vertical electric field strength excited by an electric dipole is

$$E_\theta = K_E \cdot \sin\theta \cdot \left| \frac{j}{kr} + \frac{1}{k^2 r^2} - \frac{j}{k^3 r^3} \right| \qquad (1)$$

[53, p.135] at a distance r, where $K_E = IL\eta k^2 (4\pi)^{-1} e^{-jkr}$, with the current I on the dipole of length L, the free-space wave impedance $\eta = 120\pi$, and the wave number $k = 2\pi f/c_0$.

One can then estimate for the case of a small antenna the minimum measurement distance that is necessary to reach a certain dominance of the far field term, i.e. the $1/kr$ term in (1). By assuring that the measurements can with sufficiently small uncertainty be considered far-field measurements one will not have to perform a near-field to far-field transformation.

A small radiator can be described with a combination of complex-excitation electric and magnetic dipoles with random orientation. Due to the random orientation the near-field terms, i.e. the $1/k^2r^2$ and the $1/k^3r^3$ terms in (1), can be in phase with the far-field term. Now the worst-case relative error in the assumed far field due to the near field at the position of the measurement antenna with all terms being in phase can be estimated to be

$$e_{rel} = \frac{\left| \frac{1}{kr} \right|}{\left| \frac{1}{kr} + \frac{1}{k^2 r^2} + \frac{1}{k^3 r^3} \right|} . \qquad (2)$$

At 900 MHz and a measurement distance of 1 m (2) yields an error of 5.6% or ±0.47 dB, which will have to be taken into account for the estimation of the total measurement error. At a distance of 0.5 m the near-field error can be up to almost 1 dB, which would be a generally unacceptable error margin for antenna calibrations. For comparison, the near-field error at 5 m distance is <0.1 dB. At 1.8 GHz the error at 1 m decreases to 0.22 dB, and at 5 m measurement distance it would even be smaller than 0.05 dB (see Table 1).

Table 1: Possible inaccuracy due to far field assumption, at 900 MHz and 1.8 GHz.

Frequency	d = 5 m	d = 1 m	d = 0.5 m
900 MHz	±0.093 dB	±0.47 dB	±0.96 dB
1.8 GHz	±0.043 dB	±0.022 dB	±0.44 dB

Not only the influence of the assumed far-field condition in the transversal field, but also the influence of the radial field component of the near field

$$E_r = 2K_E \cdot \cos\theta \cdot \left| \frac{1}{k^2 r^2} - \frac{j}{k^3 r^3} \right| \qquad (3)$$

[53, p.135] has to be taken into account. The radial field (3) reaches its maximum at that angle (namely at $\theta = 0$) where the transversal component has its minimum. Therefore, the radial near field might influence the detection of the nulls in the radiation pattern of an antenna. For instance at 900 MHz and 1 m distance the maximum level of the radial component is 19.5 dB below the maximum level of the transversal component.

Most antennas that are used as measurement antennas have very good polarisation purity between transversal and radial fields. In case of a horn antenna it is still possible that a small portion of the radial field couples into the antenna especially at the edges of the aperture where the radial field produces a small vertical field component in the aperture. However, the power distribution of the electric fields across the aperture of the horn does not support that waveguide mode and attenuates the radial component strongly. Thus, at the feed of the horn only the transverse far-field component of the coupled fields is detectable.

The measurement antenna is likely to be a larger antenna, e.g. a horn antenna with a certain aperture. If a spherical wave is assumed to propagate from the AUT, the flat aperture of the measurement antenna will be illuminated by wavefronts with different phases in the centre and the corners of the aperture (see Fig. 14). This phase error is investigated in the following, for the case of a wideband corrugated horn antenna with an aperture of 245×142 mm^2.

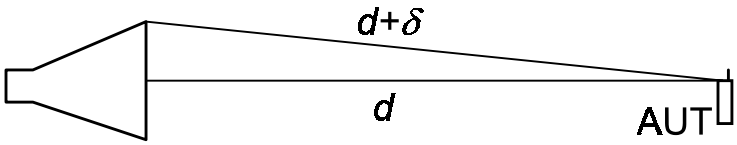

Figure 14: The aperture of the measurement antenna is illuminated by wave fronts with a phase difference of δ/λ.

Seen from the AUT, the different areas of the horn antenna aperture - like centre and corners of the waveguide - are effectively situated at different distances. Depending on the distance between the two antennas, the phase error and amplitude error due to this ranging distance is significant or negligible.

Usually a distance of $d_{FF1} = 2D^2/\lambda$ or $d_{FF2} = 4D^2/\lambda$ denotes the sphere that forms the border between the Fresnel zone and the so-called Fraunhofer region in which far-field conditions are valid [54] and [55, p. 60, pp. 809-810]. D denotes the maximum dimension of the antenna, d_{FF1} comes from the area of EMC while the stricter limit d_{FF2} is more commonly used in antenna measurements. This means at 900 MHz for the horn antenna with an aperture $A = 245 \times 142$ mm^2 that the Fresnel zone limit is $d_{FF1} = 485$ mm or $d_{FF2} = 970$ mm. Apparently, the near-field conditions do not stop abruptly to be valid, as little as the far-field conditions are abruptly valid beyond this border sphere. Rather one should think

of a border region between the Fresnel and Fraunhofer regions, within which far-field conditions may be assumed with a certain error margin that has to be taken into account.

According to [18] for the same antenna and at distances larger than $4D^2/\lambda = 970$ mm we can expect the ratio of the measured gain to the gain at an infinite distance to be about 0.99, i.e., an inaccuracy of 1% which is acceptable for a gain measurement, Whereas, for $d > 2D^2/\lambda = 485$ mm the ratio is 0.94, i.e. an error of 6 % is made. Another effect of phase variation along the aperture of the measurement antenna is, that nulls in the radiation pattern are partially filled. In Fig. 15 the effect is illustrated for distances $2D^2/\lambda$, $4D^2/\lambda$ and an infinite difference [3, p.21]. At these distances the phase error is 22.5° and 11.25°, respectively. Small antennas generally do not show a strong directivity and the exact position of nulls or the exact level of side-lobes below 20 dB are usually not very important in mobile handsets. So, to set the limit for the measurement distance at $d > 4D^2/\lambda$ is perfectly sufficient.

It should be noted that also the AUT could cause uncertainties in the ranging distance due to its varying phase centre. A small mobile handset should on the first glance be rotated around the feed point of its antenna, since the phase centre of a monopole antenna on an infinite ground plane is at its feed point. However, due to the finite size of the chassis the handset antenna does not produce the symmetric radiation pattern of a dipole. The mobile handset is rather a combination of the antenna element with confined current distribution, and the phone chassis resembling a thick dipole and supporting the respective current distribution [23] [24], which means that the location of the phase centre varies as a function of frequency, at lower frequencies it is closer to the centre of the handset since the chassis is then a more efficient radiator than the electrically short antenna, at higher frequencies close to the feed point of the antenna, which is then in length closer to $\lambda/4$. In the case of small distances between the AUT and the measurement antenna, changes in the location of the phase centre during the rotation of the AUT cause considerable variations in the effective measurement distance. The knowledge of the accurate distance is an important factor in the calibration, because the path loss between the two antennas determines the correction coefficient for the transmission coefficient when measuring the gain of the AUT.

At 5 m measurement distance the deviation in the location of the phase centre of the AUT is usually neglected. This is reasonable, as the phase centre only varies within the dimensions of the antenna and a possible phone chassis, which is typically located at the centre of the measurement sphere. The length of modern mobile handsets is around 80 mm - 120 mm without the antenna. As the electric field strength E is proportional to $1/r$, the displacement of the phase centre along the chassis to e.g. 50 mm from the antenna can lead to a worst case inaccuracy in the field strength (and in the gain that is based on the assumed ranging distance) of about 1% i.e. less than ± 0.09 dB. However, when measuring the same mobile handset at e.g. 0.5 m, the changing phase centre could cause a relative error in ranging distance of up to 10%, i.e. a field strength inaccuracy of ± 1 dB, which would be unacceptable for antenna calibrations.

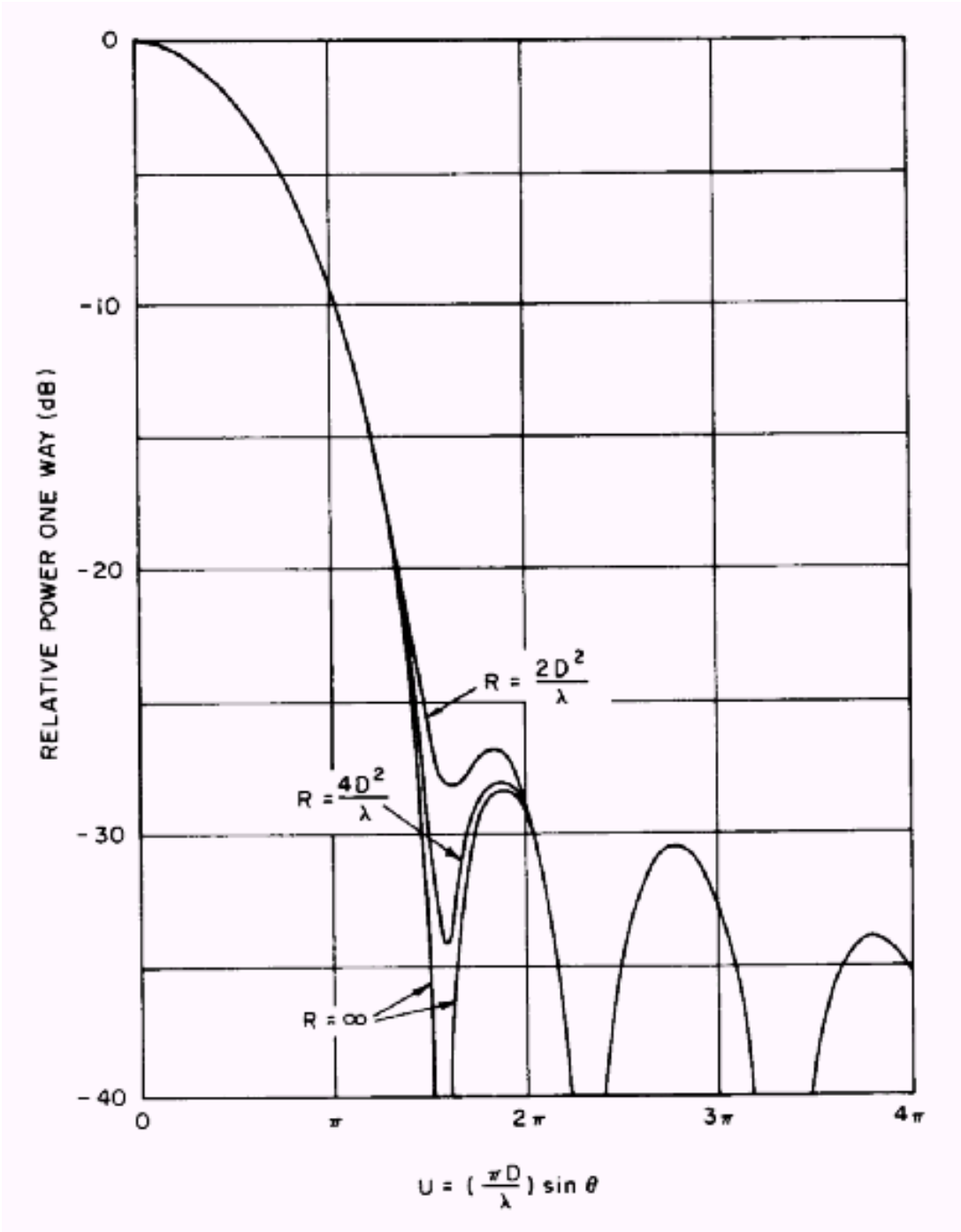

Figure 15: Calculated radiation patterns illustrating the effect of phase errors encountered in measuring patterns at the ranges R indicated [56, pp. 14-10].

At a distance of 1 m between the antennas and making the optimistic assumption that the actual displacement of the phase centre from the feed point of the antenna may be about 10 mm, the relative ranging-distance error causes acceptable inaccuracy in the measured amplitude of the E-field of ± 0.09 dB. However, it has to be noted, that the phase centre of the radiation may vary considerably depending on the frequency, especially for multi-frequency devices [23], [24] as was discussed above. So in order to get as close as possible to the above-calculated relative ranging-distance error with

e.g. a dual-frequency device at 1 m measurement distance one could as a rule of thumb perform the rotation around a point between the feed point of the antenna and the physical centre of the handset (Unless the measurements are performed separately for both frequency ranges, in which case the centre of rotation should be chosen individually and according to the estimated location of the phase centres given above).

The position of the phase centre is much more difficult to determine when the measured AUT is placed in the anechoic chamber together with a human head model. A head model can be used to take into account the influence of the user on the efficiency and radiation pattern of the handset during operation. The head model represents basically a relatively large, round and lossy body. Even if it therefore does not resemble a secondary radiator or a dielectric lens, it may still work as a small reflector at the frequencies that are discussed here (i.e. > 900 MHz). The antenna of a handset in operation is usually situated about 20 – 30 mm from the head of the user. The effective phase centre of the antenna-reflector combination may be anywhere between these points, i.e. up to about 30 mm from the feed point of the antenna. Then the above-mentioned displacement of the phase centre by only 10 mm may not be valid anymore. Instead, one has to expect the inaccuracy due to the variance in the phase centre position to be around ± 0.1 ... 0.26 dB (see Table 2).

Table 2: Field strength inaccuracy in case of displacement of the phase centre from the antenna feed point, *d* = measurement distance.

Displacement	d = 5 m	d = 1 m	d = 0.5 m
10 mm	±0.02 dB	±0.09 dB	±0.18 dB
30 mm	±0.05 dB	±0.26 dB	±0.54 dB

As a last point the influence of multiple reflections between the apertures of the two antennas may have to be taken into account [1, p. 17]. In mobile communications systems, resonant type antennas are used, such as helix or patch antennas. At resonance such an antenna transforms most of the incoming radiated energy into an electric signal at its port, and vice versa. However, the antenna still reflects or scatters some part of the incident wave. At smaller distances d between the antennas the transmitting antenna will cover a greater solid angle seen from the receiving antenna, i.e. it is exposed to more of the scattered field reflected back from the receiving antenna than for a larger distance. Also the free-space attenuation of the scattered fields at distance d is smaller than for conservative measurement distances of several meters. So, when two antennas face each other at 1 m, those multiple reflections might not simply be neglected as is done for larger measurement distances and have to be investigated.

The aperture of the horn antenna described above is A_1 = 35000 mm^2 and the back scattering from the horn antenna aperture is assumed to be around 50 %, i.e. $\rho_1 = 0.5$. The worst-case aperture of a small radiator can be estimated to be in the range of A_2 = 500 mm^2 and the worst-case back scattering from this antenna aperture is assumed to be 50 %, i.e. $\rho_2 = 0.5$. The scattered fields can be assumed to propagate spherically

from the antenna apertures and thus the scattered power density at a distance d is $1/4\pi d^2$. In the case of the horn antenna the gain has an effect on the propagation of the scattered fields, i.e. the power will be partly directed towards the direction of the DUT. For the horn antenna in question the gain in the discussed frequency range is around G_1 = 10 dB. The ratio of the power P_{in} that is directly received by one of the antennas and the power P_{rr} that is reflected twice (once from the receiving antenna and then back from the transmitting antenna) can be estimated as

$$\frac{P_{rr}}{P_{in}} = \frac{\rho_1 A_1 G_1 \cdot \rho_2 A_2}{(4\pi d^2)^2} \approx -55 \text{ dB}, \qquad (4)$$

where d = 1 m measurement distance. This low interference level can be neglected during antenna measurements.

As a final conclusion it can be said, that of all error sources that are related to the small distance between the antennas, the assumption of far-field conditions introduces the largest inaccuracy to the antenna measurements, as it is almost ± 0.5 dB at 900 MHz and 1 m measurement distance. For 1.8 GHz this effect is again negligible, however, when a head model is included in the antenna measurements of mobile handsets, the unknown exact position of the phase centre may contribute up to ± 0.26 dB inaccuracy in the measured field strength at 1 m measurement distance.

4.2. Effect of RF absorbers in the vicinity of small antennas

Another limiting factor for decreasing the size of a small anechoic chamber is the distance between the absorbers and the AUT. The distance between the antennas cannot be decreased arbitrarily for two reasons. At a too short distance the carbon loaded foam will be situated in the reactive near field of the antenna, whereby the current distribution on the antenna and also on the chassis may change, and hence the whole radiation pattern of the handset might change. The second reason is that, when the distance between antenna and sidewalls decreases, the incidence at the sidewalls between the two antennas becomes increasingly grazing. At such non-normal incidence the reflection coefficient of the absorbers gets poorer (Fig. 16). Hence, a stronger interference pattern between direct and reflected field is caused which affects the measured radiation pattern. Both measurements and computer simulations were used to investigate these two effects.

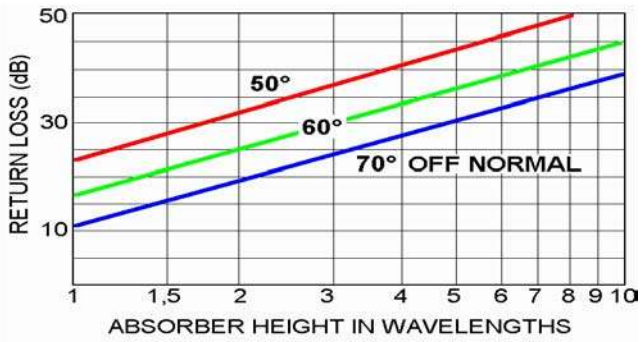

Figure 16: Return loss vs. angle of incidence for pyramidal absorbers [57]

Measurements of the radiation pattern of antennas are usually performed in a large anechoic chamber in order to avoid reflections from nearby objects, because interferences from the reflections would affect the field pattern. The use of small anechoic chambers for the radiation pattern measurement of small mobile handset antennas is desirable as was discussed above. A lower limit for the dimensions of an anechoic chamber is set by the possible proximity of absorbing material to the antenna under test (AUT). Also the use of other small chambers such as GTEM cells has been discussed in the previous chapter. However, their disadvantages are the limited dynamic range due to reflections from the termination and the limited frequency range due to higher order modes.

The handset antennas used in mobile communication systems are often small compared to the wavelength. When we consider the complex platform of a handset with a monopole or patch antenna as the radiating structure [23], [24], the physical length of the radiator is less than a wavelength. Such electrically small antennas usually show a relatively small directivity of below 10 dB. In order to characterise their three-dimensional radiation characteristics, like the total radiated power, with sufficient accuracy, the angular distance between the different measurement planes should be smaller than 90º. For electrically large antennas an angular distance of 90º is a typical value, resulting in three principle-plain cuts.

4.2.1. Transmission coefficient measurements

The test measurements were performed inside a large anechoic chamber to reduce the influence of external sources and objects. A patch antenna with a ground plane size of 45 mm × 40 mm and a F/B ratio of 4.5 dB was placed in front of RF absorbers (type: RANTEC EMC-24CL) with 3×3 pyramidal absorber cones, back plane dimensions of 610 mm × 610 mm and a thickness of 610 mm from tips to back plane. The resonance frequency of the patch was 1.8 GHz.

To obtain maximum variation in the measured field the measurement antenna was placed in the back lobe of the patch antenna where the field strength is considerably lower than in the main lobe. The absorbers were placed in the main lobe in order to maximise the strength of the reflected field (Fig. 17). To achieve maximum interaction between antenna and absorbers, the antenna was situated at the height of

the centre absorber tip. By moving the absorbers the distance from the tip to the antenna was decreased starting from 1 m, until the absorber tip touched the dielectric material of the patch antenna. Then the antenna was moved 100 mm sideways so that it could be placed inside the absorber structure, which is denoted in Fig. 17 by negative distance.

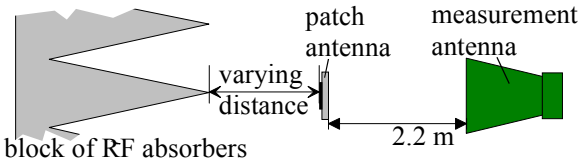

Figure 17: Measurement set-up for transmission measurements with the AUT (a quarter-wave patch antenna) positioned close to the resistive absorbers.

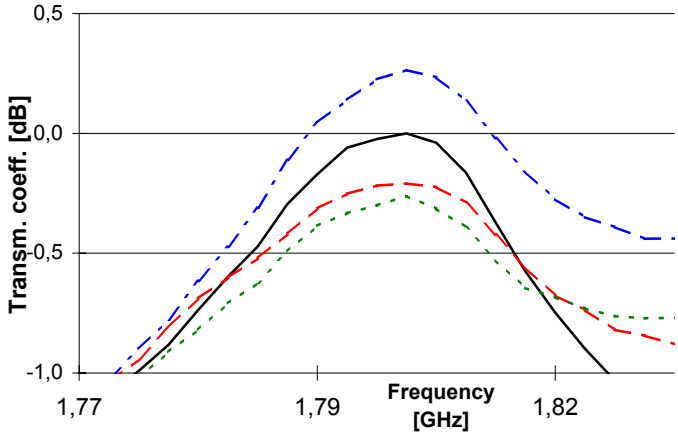

Figure 18: Measured normalised transmission coefficient in the back lobe of the AUT for different distances *d* from the absorber tips, solid line: *d* = 1 m, dashed line: *d* = 0.1 m, dotted line: *d* = 0, dash-dot line: *d* = -0.1 m (i.e. antenna is inside absorber structure).

In the transmission measurement the measurement antenna picked up the field in the back lobe (180 degrees from broadside) of the patch. The measurement results can be seen in Fig. 18. As close as 100 mm no considerable change in the back lobe was observed, i.e., the fluctuations stay within ±0.25 dB. Even when the antenna is moved into the absorber structure, an overall deviation of only ±0.3 dB is seen. The fluctuations were identified as an interference pattern between back lobe and reflected front lobe. It was also noticed that the changes in the input impedance and quality factor of the antenna were negligible.

4.2.2. EM-field computer simulations

The influence of the absorbers was simulated using finite-element method software. The set-up was similar to the one used in the measurements (Fig. 19). A simulation space of $1 \times 0.25 \times 0.25$ m^3 was used. Absorbing boundaries were used to calculate the far field, and two symmetry planes were used to decrease the simulation space.

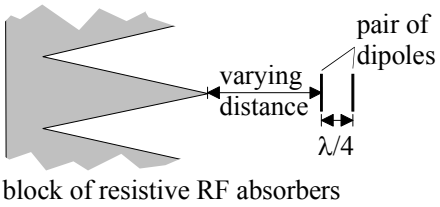

Figure 19: Simulation set-up similar to the one for transmission measurements with a pair of dipole antennas positioned close to resistive absorbers.

The relative complex permittivity of the absorbers used in the simulations was $\varepsilon_r' = 2$, $\varepsilon_r'' = 3$ at 1.8 GHz [58]. Two 10 mm long current dipoles were excited with $I = 1$ mA and a phase difference of 29º. Their physical separation was $\lambda/4 = 41.7$ mm. This resulted in a main lobe pointing towards the absorbers and a front to back lobe ratio of 4.5 dB, i.e. the same value as the patch antenna had in the measurements. As the main idea of the simulations was not the design of the antenna, the two-dipole model was preferred to a patch-antenna model, in order to concentrate the computational resources on the propagating fields and not on the antenna model.

The dipole pair was situated at 6 distances between 39 and 143 mm from the absorber tip. The calculated far field in Fig. 20 shows a similar fluctuation in the back lobe of the antenna as in the measurements. The fluctuations stay within ±0.25 dB when the distance from the centre of the dipole pair and the tip of the absorber is larger that 102 mm.

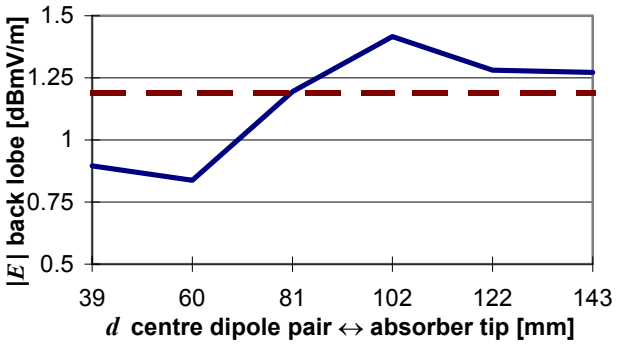

Figure 20: Simulated electric field in 10 m distance, in the back lobe of a pair of phased current dipoles ($\Delta\phi$ = 29º) at 6 distances from the tips of the absorbers (solid line), theoretical field strength (dashed).

To verify a sufficiently large dynamic range of the simulations to show fluctuations of this order, the phase difference of the dipole pair was changed to 90º. Hereby, theoretically a back-lobe level of zero is achieved. The field in the back lobe should thus be only that part of the main lobe that is reflected from the absorbers. As can be seen in Fig. 21, the field strength in the back lobe, normalised to the front lobe level, oscillates between approximately -34 dB and -43 dB. This can be estimated to be caused by two signals with normalised levels of about -37.5 dB and -44 dB. The higher signal would cause a ripple of about 0.2 dB in the case of 4.5 dB front- to back ratio, which is in close agreement with the results in Fig. 20. The level is also very well in the range of the plane-wave reflection coefficient of the absorbers. The lower

signal is obviously caused by the inevitable inaccuracy of the simulation, but is very low showing the high dynamic range of the calculation.

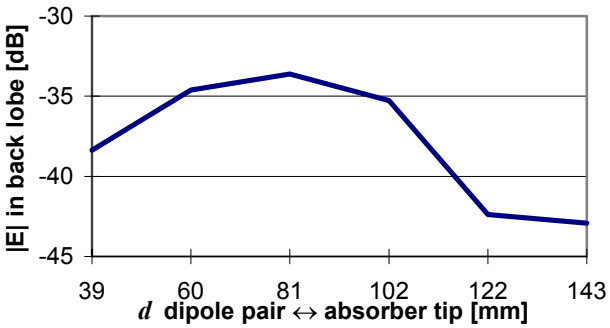

Figure 21: Simulated electric field in 10 m distance, in the back lobe of a pair of phased current dipoles ($\Delta\phi$ = 90º) at 6 distances from the tips of the absorbers, normalised to main lobe level.

Finally, the influence of a narrow transmission channel was investigated. A pair of pyramid RF absorbers (type: RANTEC EMC-24CL) was positioned between two antennas in such a manner that there was a gap between the tips as a propagation path from one to the other antenna (see Fig. 22). The gap width was varied. The transmission coefficient between the AUT and the measurement antenna was measured for two orthogonal polarisations.

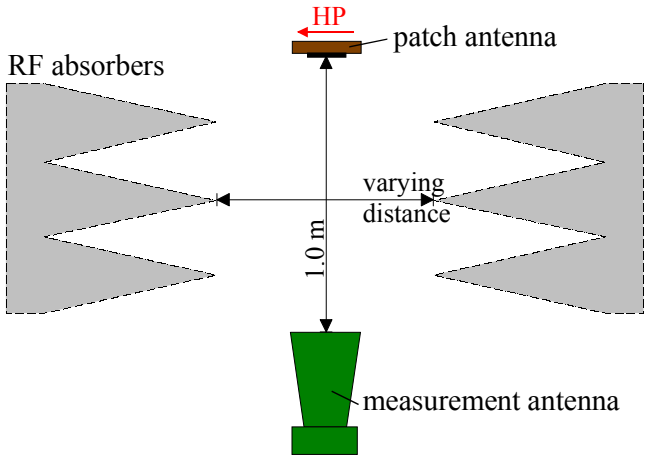

Figure 22: Top view of measurement set-up for transmission measurements through a transmission channel formed by the resistive absorbers on side walls. HP denotes horizontal polarisation.

In Fig. 23 the transmission coefficient is shown in the case where both antennas are vertically polarised (VP). Even when the absorbers are so close, that the opposite tips are in the same plane, the transmission between the antennas is practically not affected, i.e. the fluctuation stays within ±0.4 dB. When both of the antennas are horizontally polarised (HP) the transmission coefficient increases due to the absorbers (see Fig. 24), which can be explained by the lens effect of the dielectric material. But even in this case, a gap of 50 mm results in a deviation of only about 0.2 dB in the transmission coefficient when compared to the case with no absorbers present.

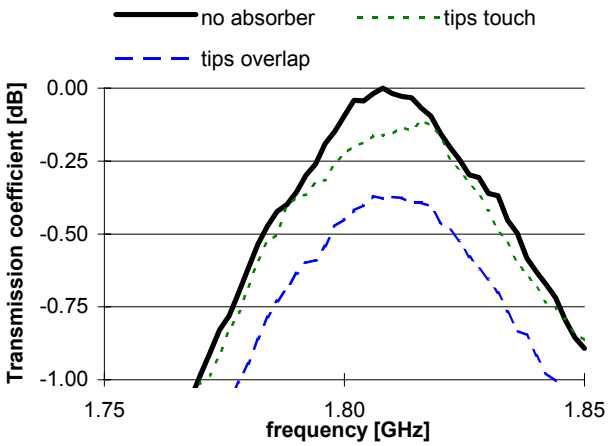

Figure 23: Influence of RF absorbers when they form a transmission channel parallel to the polarisation of the two antennas (VP), measured at 1.8 MHz.

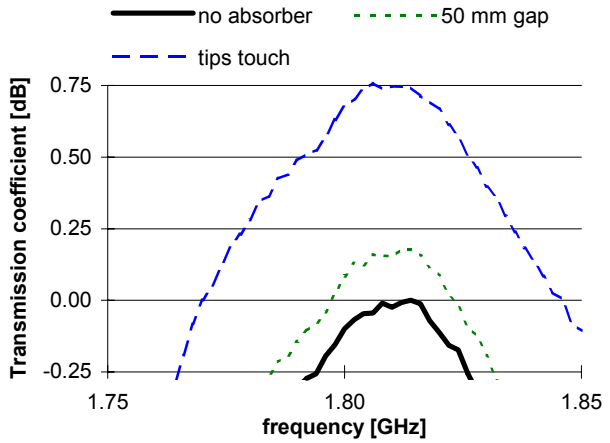

Figure 24: Influence of RF absorbers forming a transmission channel perpendicular to the polarisation of the two antennas (HP), measured at 1.8 MHz.

It can be said as a rule of thumb that absorbers with a thickness of 610 mm do not have a substantial effect on the radiation characteristics of a small antenna at around 1.8 GHz, as long as they are kept more than 100 mm away from the AUT. Furthermore the transmission channel formed by the absorbers between the antennas must be wider than 100 mm in order to have an undisturbed transmission between the AUT and the measurement antenna. This justifies measurements of the radiation pattern and other characteristics of small antennas in much smaller (possibly down to table-top size), anechoic chambers than the usual large chambers, with the AUT situated much closer to the absorbers than normally.

Additionally, the results show that computer simulations are a useful tool when investigating the feasibility to measure the radiation pattern of small antennas in a small anechoic chamber, and the results also show that computer simulations can help optimising a chamber in terms of the minimum chamber size.

4.3. Design, construction, and performance of a small shielded anechoic chamber

This section describes the construction and evaluation of a small anechoic chamber, in which the measurement distance between the AUT and the measurement antenna was decreased to about 1 m. The distance between the AUT and the absorbers on the side- and backwalls was reduced to 200 mm.

The size of the absorbers is determined by the requirements for the reflectivity level of the anechoic room. This again is dependent on the gain of the antennas involved, i.e. the measurement antenna and the AUT. Usually a horn antenna is used as a measurement antenna. In the following an average value of 8 dB for the gain of a horn antenna, and 2 dB for the general case of an AUT are used. The size of the AUT determines the size of the test volume in which the reflectivity level has to be met. For a 20 mm long antenna on a 100 mm long chassis, which has to be rotated around the feed point of the antenna, a quiet zone (or test volume) with a diameter of 250 mm is sufficient and will be used in the following.

The chamber was built with an area of about 2.5 m by 2.5 m and a height of 2.40 m (see Fig. 25a). Relatively large absorbers were used in this chamber (see Fig. 26). These large absorbers were needed because the chamber is also meant for EMC radiated emissions near-field measurements down to 100 MHz. The specifications for a test volume with a diameter of 250 mm were given as follows: ± 3 dB variation on the field strength amplitude (or a reflectivity level of – 10 dB) at 100 MHz for omnidirectional radiating devices, and better than ±0.1 dB variation above 900 MHz for moderately directive antennas under test, i.e. a reflectivity level of – 45 dB. In order to fulfil these requirements the end walls of the room had to be covered by 450 mm long absorbers, and the side walls, floor and ceiling of the room by 910 mm long absorbers.

Initially the positioner had been made of PVC material, which proved to be unsuitable for this purpose, due to its high dielectric losses (see Section 4.3.1). Therefore, the positioner was replaced by one made of very lightweight honeycomb material with four layers of thin sheets, which ensure a high stability and at the same time a minimal absorption of electromagnetic energy. The positioning system has two rotators on two perpendicular axes, which allow automated, computer-controlled measurements of three-dimensional radiation patterns (see Figure 25b). This system allows the radiation pattern measurement of a mobile handset together with the head model of a human user.

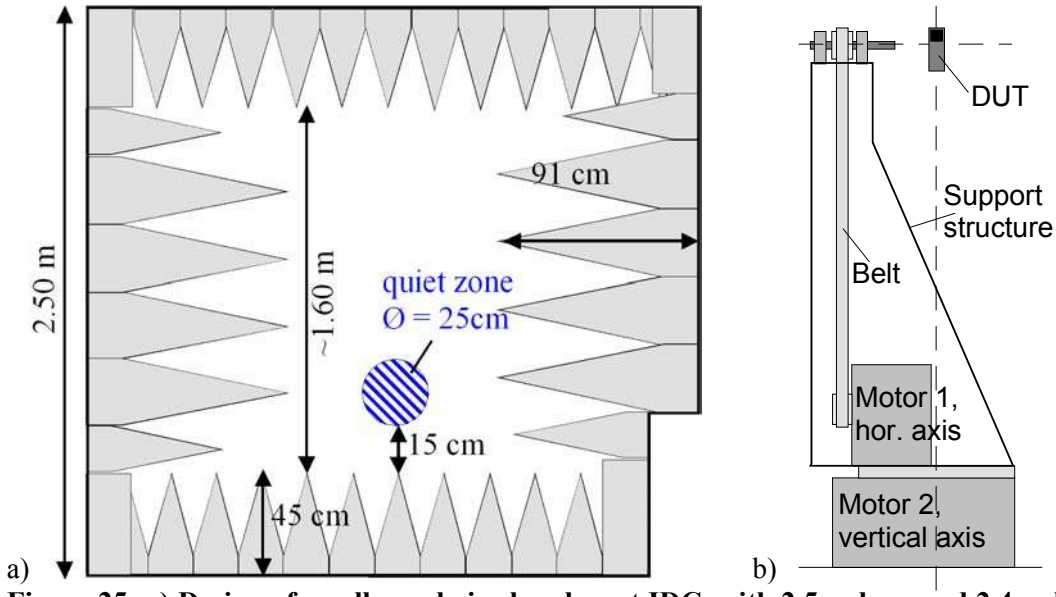

Figure 25: a) Design of small anechoic chamber at IDC, with 2.5 m long and 2.4 m high sidewalls. b) Automated positioning system with a vertical and a horizontal axis (dashed lines), the latter driven via a belt, DUT in the centre of rotation = centre of 'quiet zone'.

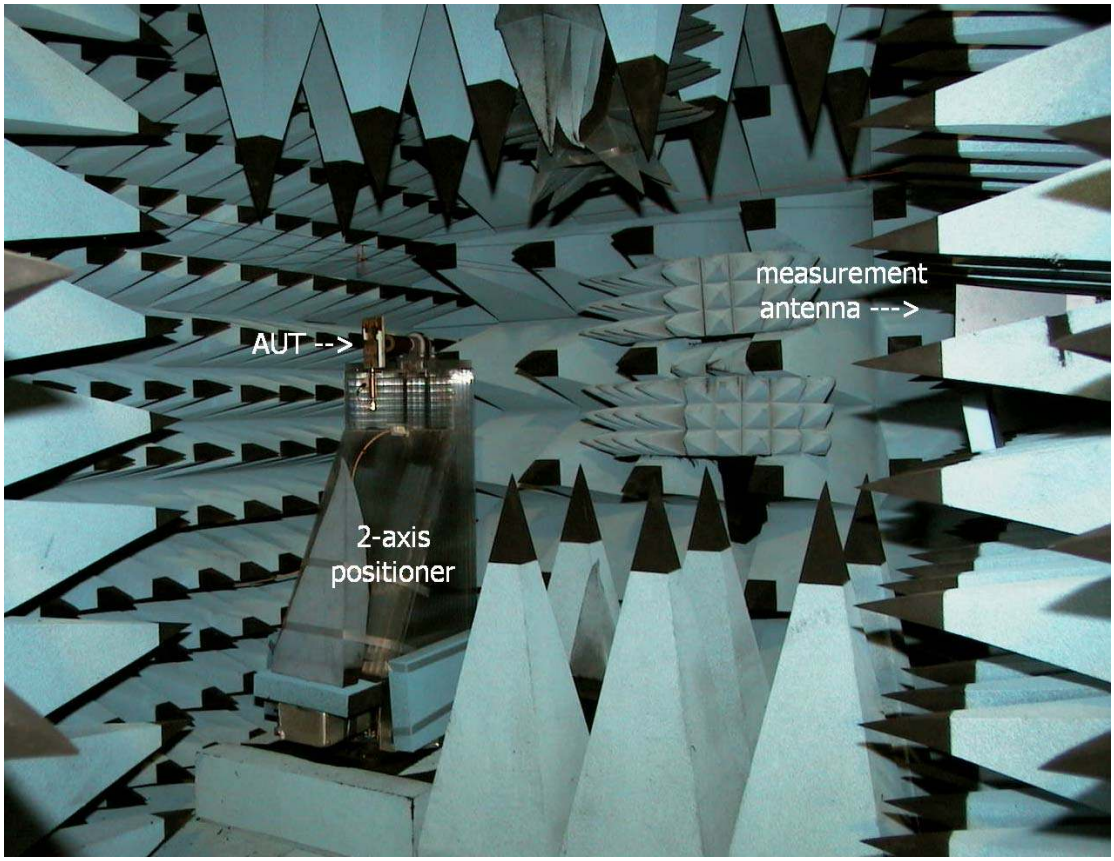

Figure 26: Small anechoic chamber at IDC, one side panel is open; we are looking at the opposite sidewall with 900 mm thick absorbers. Also ceiling and floor are lined with 900 mm long absorbers, other walls with 450 mm long RF absorbers. One antenna (wideband horn antenna, on the right) is fixed, acts as measurement or probe antenna, the AUT (left) is rotated about two axes, and its movements are computer controlled.

4.3.1. Field homogeneity inside the small anechoic chamber

The actual performance of the chamber was first evaluated by measurements of the field homogeneity in the quiet zone. A capacitively loaded conical wideband dipole was rotated inside the test volume on eight circles with equally spaced diameters. An HP 8722C network analyser recorded the transmission coefficient between the dipole antenna and the wideband horn antenna that illuminated the anechoic chamber from the opposite chamber wall (see Fig. 27). Fig. 28 through Fig. 31 illustrate the field homogeneity at 0.8 GHz, 1 GHz, 1.8 GHz, and at 2 GHz. Quite clearly the effect of the PVC material in the initial positioner construction can be seen at positive *y* values, i.e. when the positioner tower is partly located between the two antennas. The effect is much more severe at 2 GHz, where an attenuation of more than 7 dB is caused by the positioner, while at 1 GHz the attenuation by the dielectric and lossy material is only about 3 dB. These values were not acceptable in the use of the chamber for antenna so the original PVC-positioner structure was replaced with one made from low-ε honeycomb material.

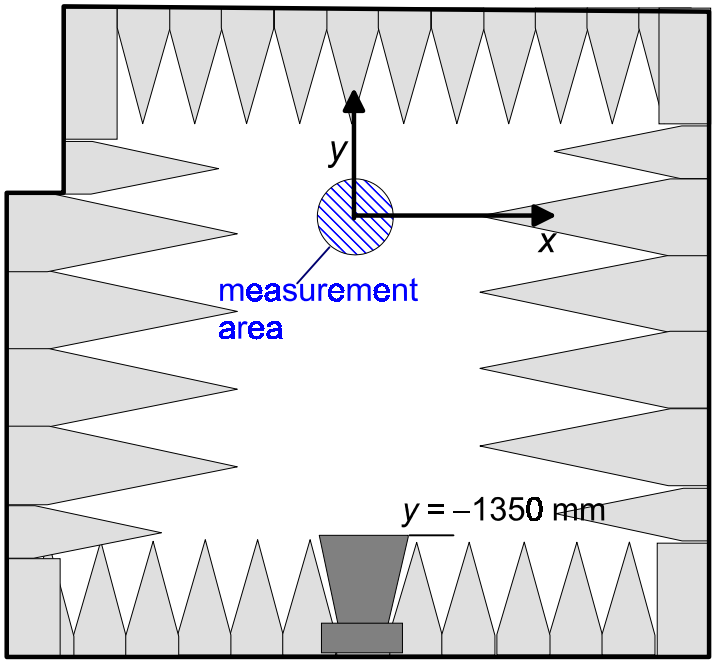

Figure 27: Measurement set-up for field homogeneity measurements in the quiet zone (i.e. the test volume) of the small anechoic chamber. Coordinate system as used in Figs. 28 – 31.

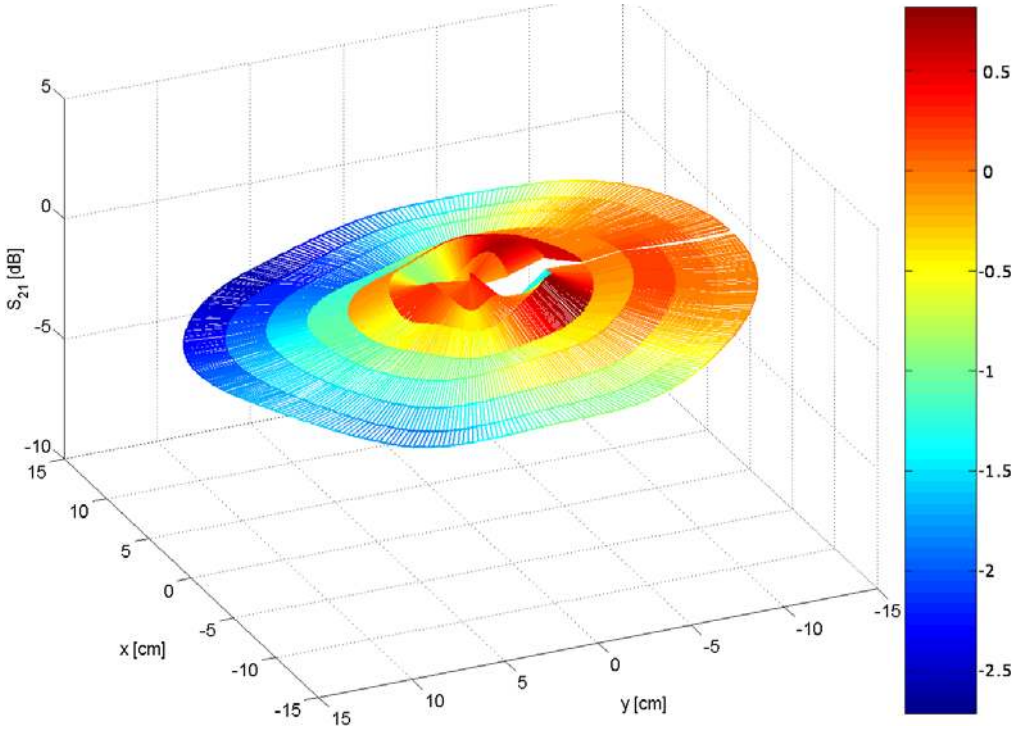

Figure 28: Measured $|S_{21}|$ at 0.8 GHz. The detected level was corrected for the varying distances between the measurement points and the measurement antenna.

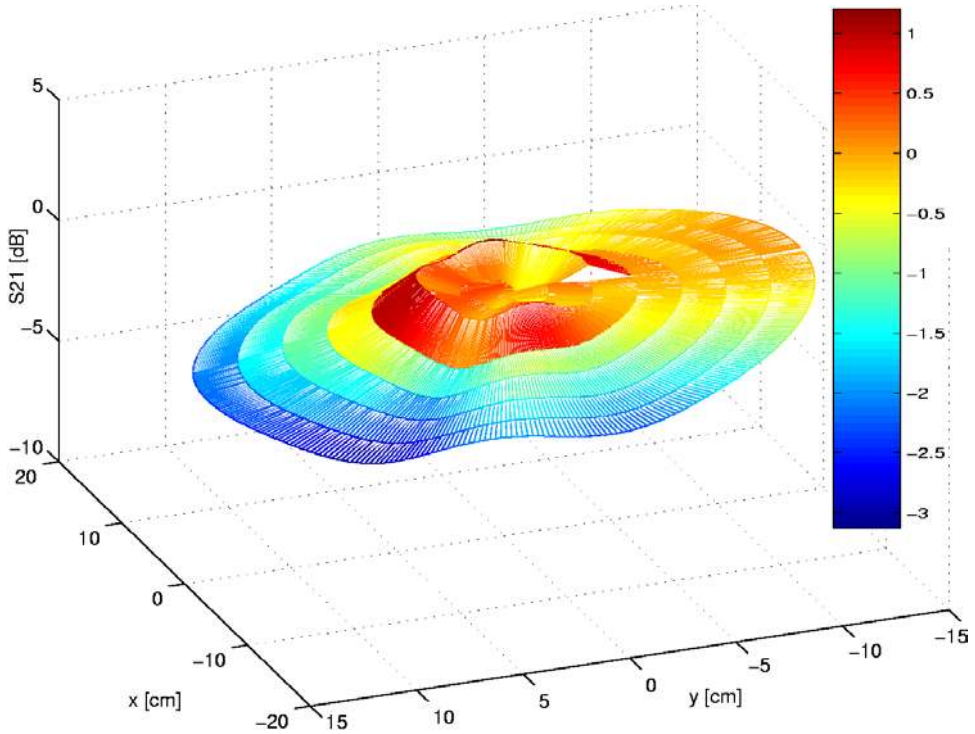

Figure 29: Measured $|S_{21}|$ at 1 GHz. The detected level was corrected for the varying distances between the measurement points and the measurement antenna.

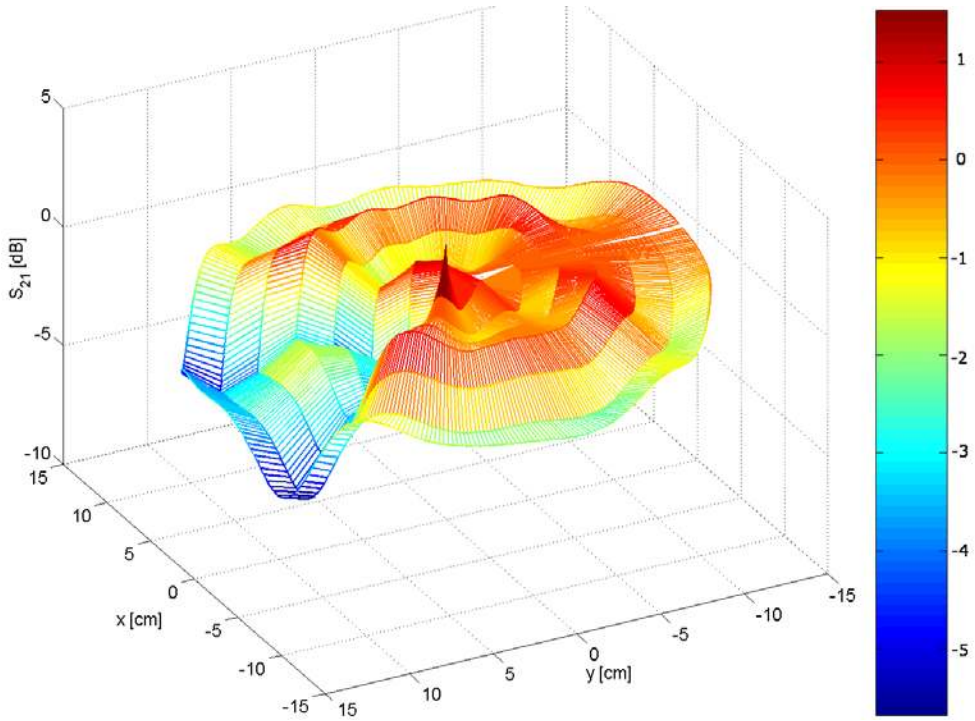

Figure 30: Measured $|S_{21}|$ at 1.8 GHz. The detected level was corrected for the varying distances between the measurement points and the measurement antenna.

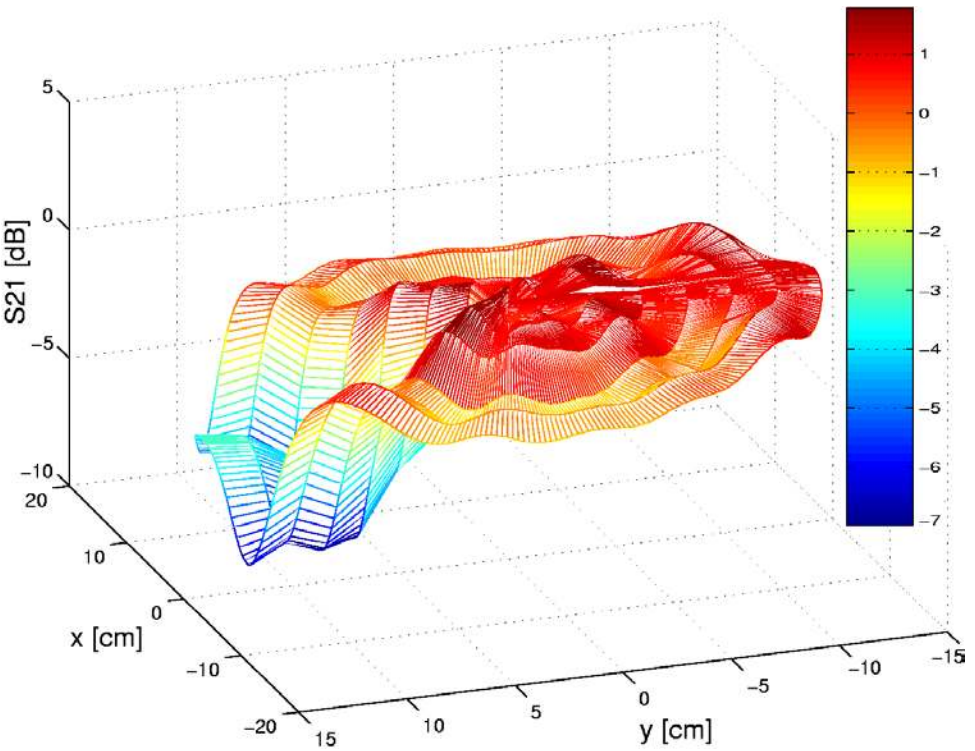

Figure 31: Measured $|S_{21}|$ at 2 GHz. The detected level was corrected for the varying distances between the measurement points and the measurement antenna.

From the measurements with the positioner it is rather difficult to estimate the homogeneity of the empty chamber (i.e. without the positioner). The inherent

reflections from the RF absorbers had to be investigated without the positioner tower, which makes the automatic movement of the probe antenna difficult. Measurements were done with a wideband dipole and a wideband double-ridged horn at 0.800 - 2 GHz, both vertically polarised. The dipole antenna was rotated around the centre of the test volume that was 1.35 m from the aperture of the horn antenna. The field was measured only along one circle with a diameter Ø = 245 mm, i.e. along the boundary of the denoted test volume. The probe antenna was mounted on a thin wooden pole with a length of 0.9 m, moved along the circle by the vertical positioner motor. Two measurements were performed, the second with the probe antenna rotated by 180° in its mounting, and the average taken to reduce the effect of non-ideal omnidirectionality in the probe antenna which was of the order of 0.1 dB. The results from this measurement can be seen in Fig. 32.

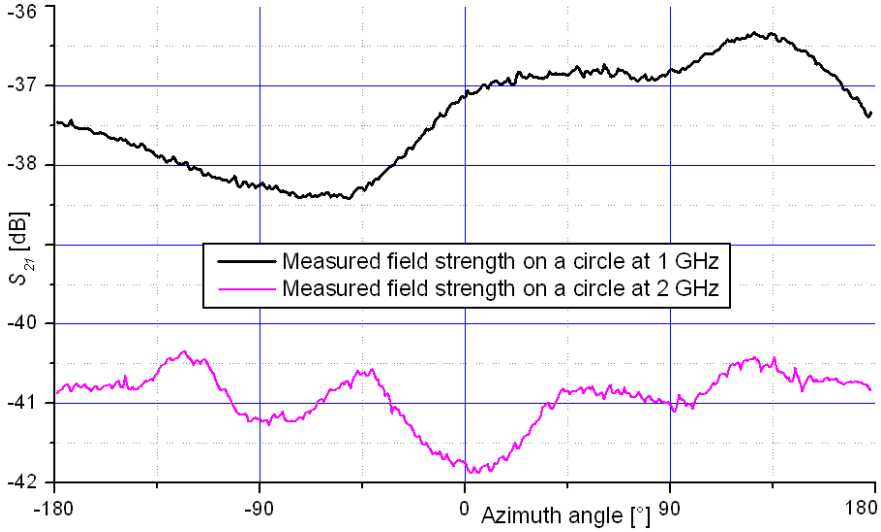

Figure 32: $|S_{21}|$ at 1 GHz and 2 GHz. The detected level was corrected for the varying distance of each measurement point from the measurement antenna. The absolute level was not normalised. Measurement-circle diameter = 245 mm, i.e. the boundary of the denoted quiet zone.

At 1 GHz the variations in the field strength were ±1 dB, at 2 GHz only about ±0.75 dB. The overall field variations are about ± 1 dB (peak to peak), at 0.8 - 2 GHz, i.e. at the frequency range of current mobile phones. The values are not as good as predicted by the estimations during the design, but much better than with the previous measurements that included the PVC-based positioner tower. The remaining inhomogeneities are probably due to imperfections in the absorber lining, which had to be modified to place the positioner mount and its large motors into the chamber. Also, due to the limited space in the chamber the relatively large absorbers do not form a homogeneous lining for the obliquely incident fields on the narrow walls, floor and ceiling, so the absorbers do not reach their peak performance that is typically given for an incoming plane wave. Another error source are the RF cables, which were not yet optimised for low field interference. Based on these nevertheless clear indications a replacement for the tower was designed using a honeycomb material (see Figs. 26, 33 and 34), which has a considerably lower absorbing effect on the radiated electromagnetic power than the initial design. To evaluate the effect of the new positioner, antenna measurements have been performed as described in the following Section 4.3.2.

4.3.2. Antenna measurements in the small anechoic chamber

The small anechoic chamber with the modified positioner tower was evaluated by measuring the radiation pattern of a dual-band patch-antenna prototype measuring 30 mm by 40 mm mounted on a ground plane measuring 110 mm by 40 mm [59]. Three principal planes were measured with help of the computer controlled measurement system. To reduce cable-related effects a balun and ferrite beads were introduced on the RF cable, as described in Chapter 5. The measurement set-ups for two of the three principal plane cuts can be seen in Figs. 33 and 34, respectively. The top part of the positioner tower, and a Styrofoam support for the prototype are visible. A short RF cable stub containing the balun was inserted between the prototype and the RF cable, and the RF cable was covered with several ferrite beads. For the horizontal axis the rotation of the positioner was restricted to an angular range of about 290º.

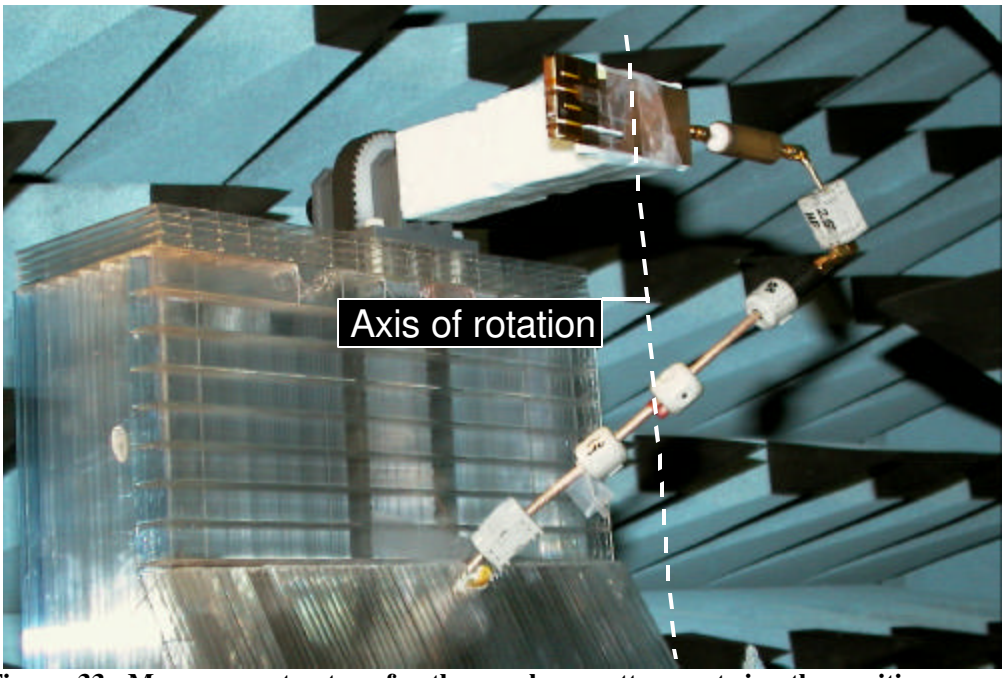

Figure 33: Measurement set-up for the *yz*-plane pattern cut, i.e. the positioner was rotated around the vertical axis (dashed line), which translates to an elevation rotation for the AUT. The dual-band balun and five ferrites were placed along the RF cable.

For comparison computer simulations and measurements performed in two large anechoic chambers are included in the gain patterns in Figs. 35 – 45. The patterns are shown for the three principal planes. Like in the small anechoic chamber, also in large anechoic chamber 1 [22] (Fig. 61, measurement distance 2 m), the dual-band balun described in Section 5 was used to suppress the RF cable related problems. No balun was used in large chamber 2, where the measurement distance was 4 m and the positioner allows azimuth movement only. Gain patterns in chamber 2 were provided by Jani Ollikainen, HUT/Radio Laboratory. Chamber 2 has a length of 8 m, a width of 4 m and a height of 5 m, and reflectivity levels of -28 dB at 800 MHz and -42 dB at 2 GHz were given for two wideband horn antennas. So, in both large chambers a sufficiently high accuracy is ensured in antenna measurements at 0.9 – 1.8 GHz.

At around 900 MHz good agreement between the measured patterns in all three environments can be noticed. In the *xy*-plane (in the coordinate system of the AUT, not of the chamber) the attenuation effect of the low-ε positioner tower in the small anechoic chamber can still be noticed when it is situated between the antennas, i.e. at around $\phi = -90^{\circ}$. Here, the positioner causes an attenuation of 1 dB (while it had been about 3 dB with the initial PVC-based positioner construction). At 1.8 GHz the overall fluctuations are larger than at 900 MHz. In the small anechoic chamber we can find all the lobes that computer simulations predict, with only small shifts in their direction and in the amplitudes of the pattern lobes ±0.5 dB error at 900 MHz and about ±1.5 dB error at 1.8 GHz. One significant exception in large anechoic chamber 2 is the sidelobe at $\phi = -45^{\circ}$ elevation that was replaced by a deep null (see Figs. 38, 41 and 44). Only cable-related interference effects can cause this null. At 1.8 GHz we can again see the attenuation effects from the dielectric material in the positioner tower in the small chamber (Figs. 40 and 43). The measurements in large anechoic chamber 1 shows smaller, fast ripples on all patterns. These ripples can only be caused by interferences from the vertically hanging RF feed cable acting as a secondary and distributed radiator. The overall agreement of all measurement cases proves that the small anechoic chamber can achieve a measurement uncertainty comparable to those of good large anechoic chambers, even though the small chamber may suffer from different error sources than a large chamber.

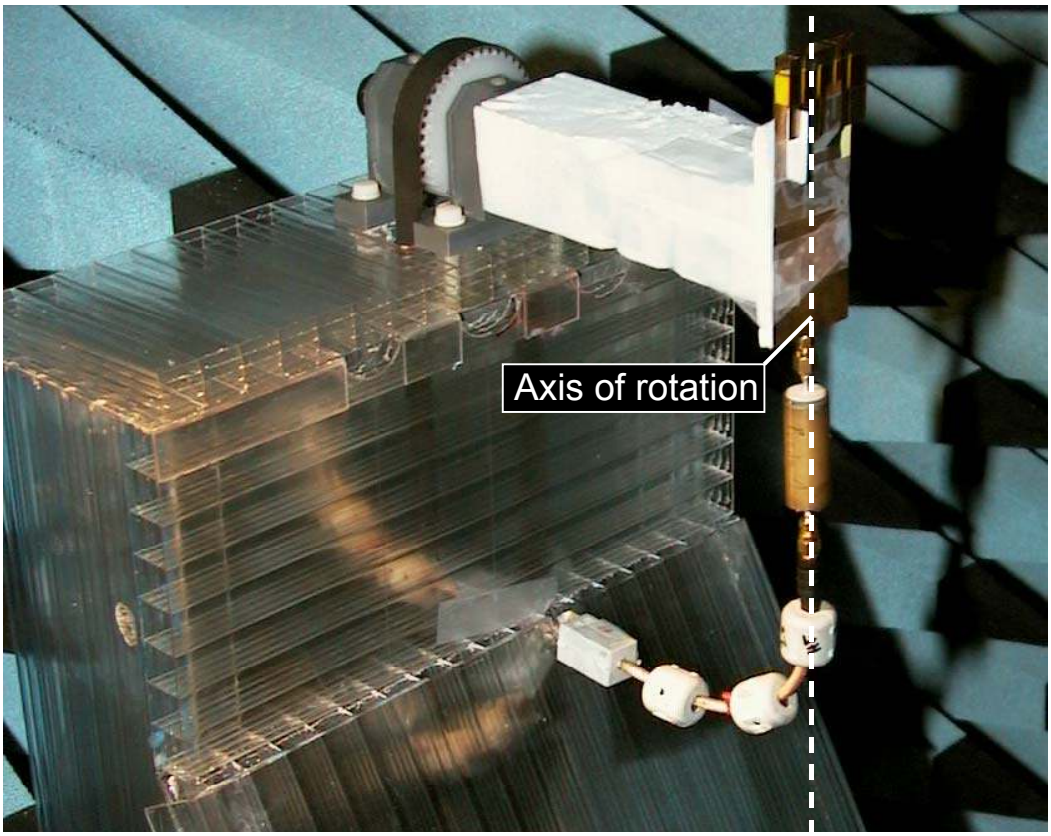

Figure 34: Measurement set-up for the *xy*-plane pattern cut, i.e. the positioner was rotated around the vertical axis (dashed line), which translates into an azimuth rotation for the AUT. The quarter-wave dual-band balun between antenna and RF cable reduces the parasitic currents on the cable shield.

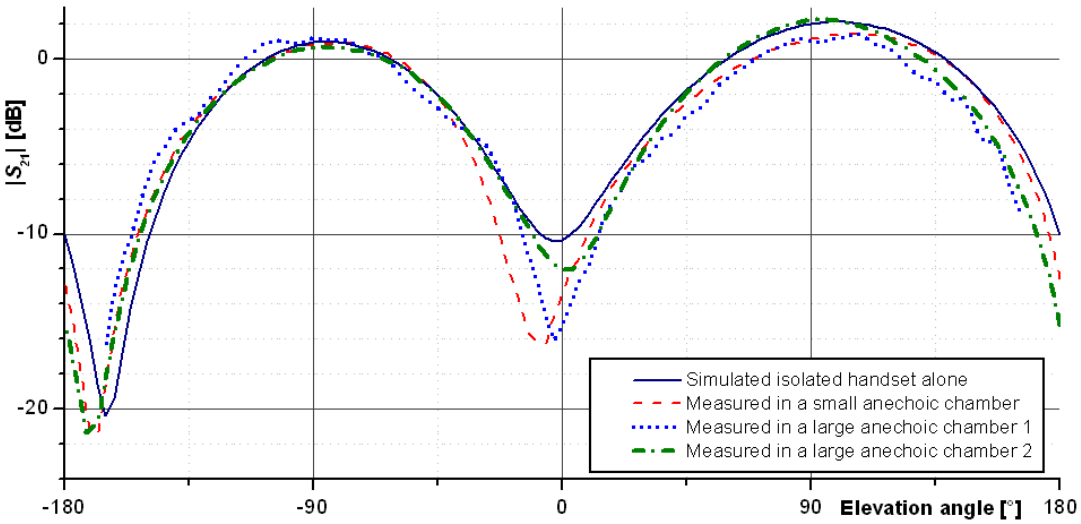

Figure 35: Far-field pattern comparison, *yz*-plane cut, E_θ polarisation, $f = 920$ MHz

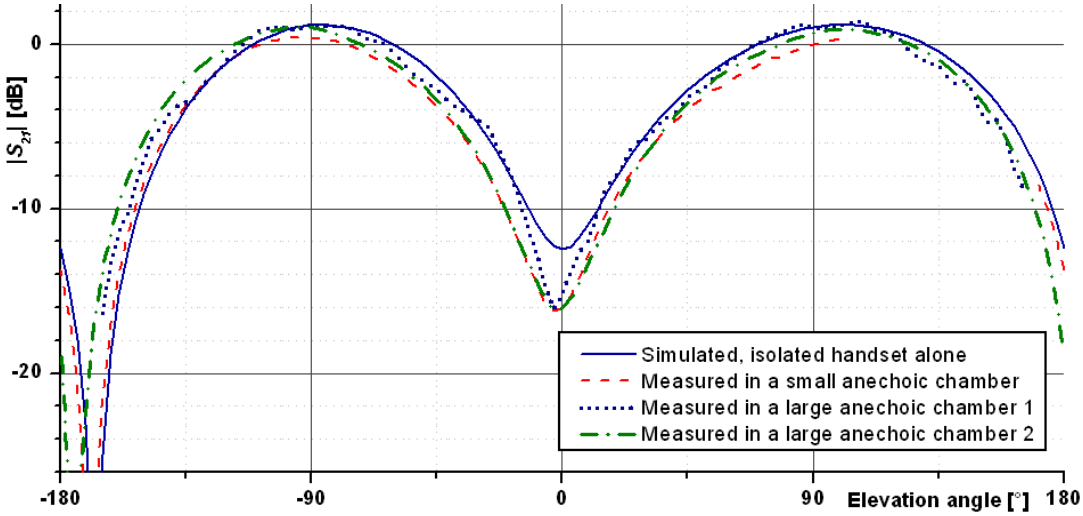

Figure 36: Far-field pattern comparison, *xz*-plane cut, E_θ polarisation, $f = 920$ MHz.

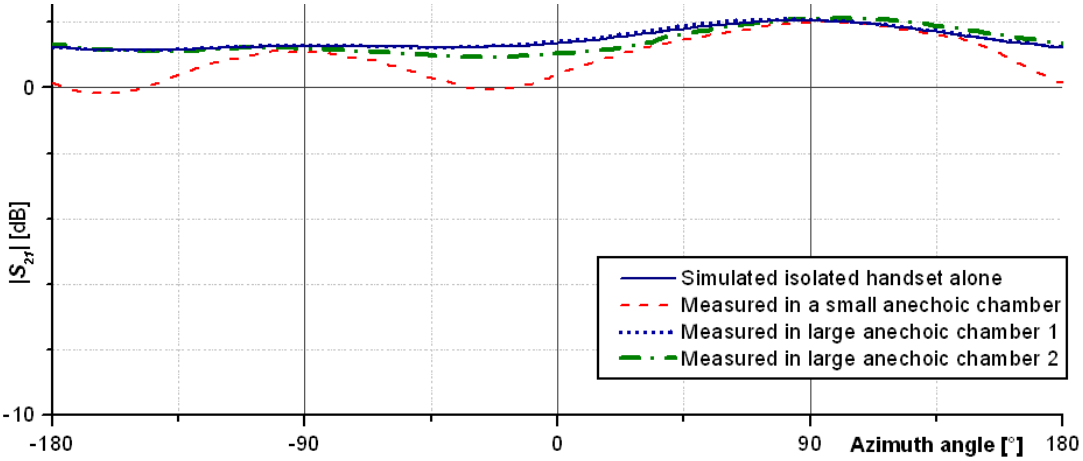

Figure 37: Far-field pattern comparison, *xy*-plane cut, E_θ polarisation, $f = 920$ MHz.

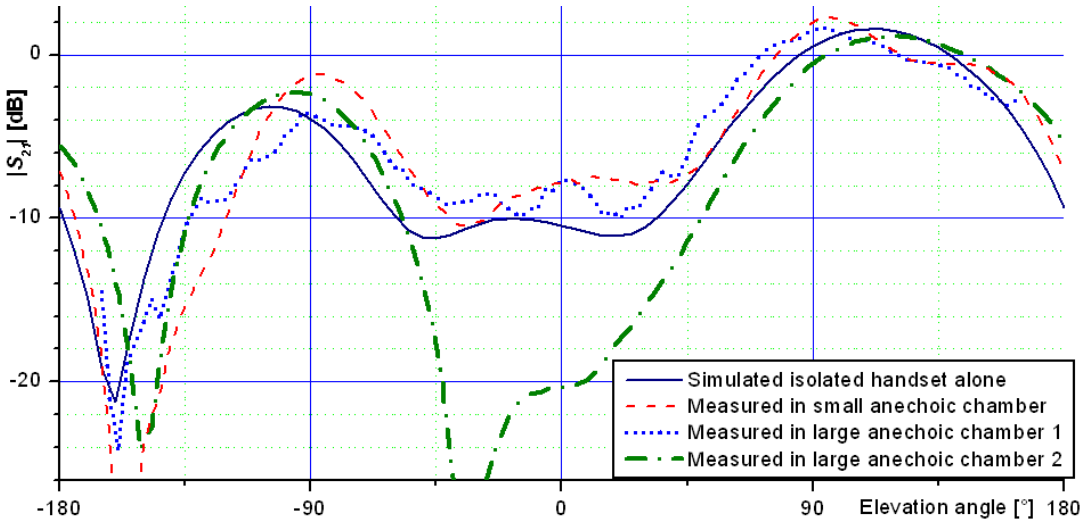

Figure 38: Far-field pattern comparison, *yz*-plane cut, E_θ polarisation, f = 1715MHz

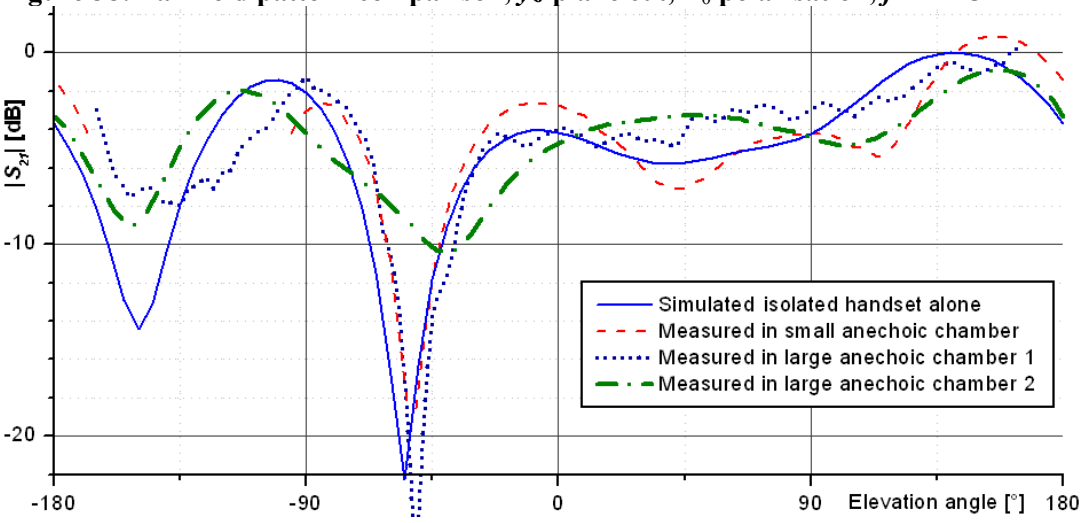

Figure 39: Far-field pattern comparison, *xz*-plane cut, E_θ polarisation, f = 1715MHz

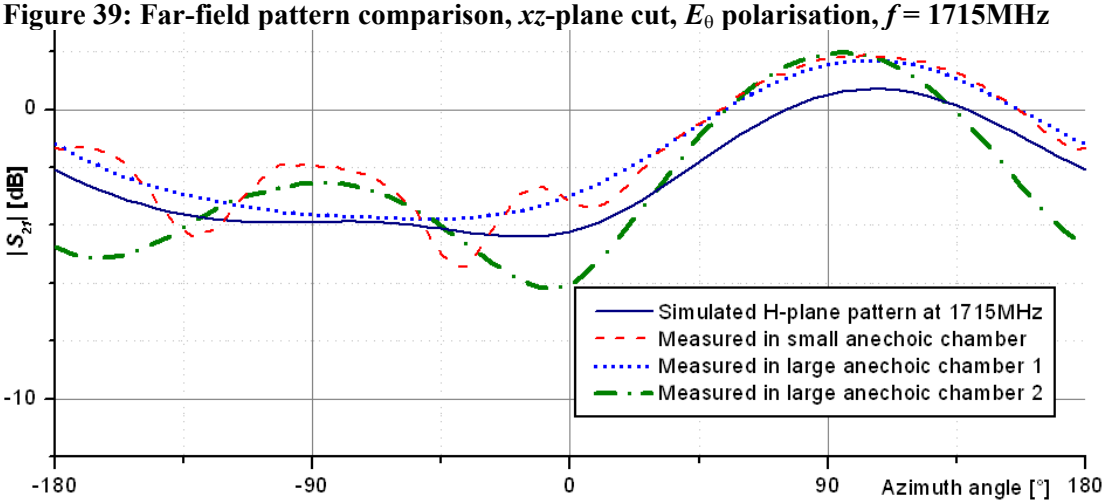

Figure 40: Far-field pattern comparison, *xy*-plane cut, E_θ polarisation, f = 1715MHz

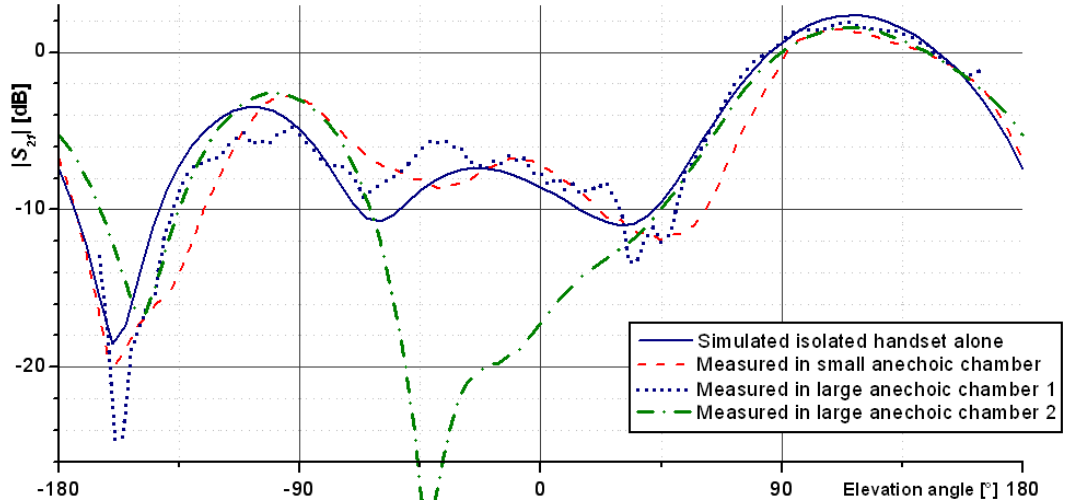

Figure 41: Far-field pattern comparison, *yz*-plane cut, E_θ polarisation, f = 1795 MHz.

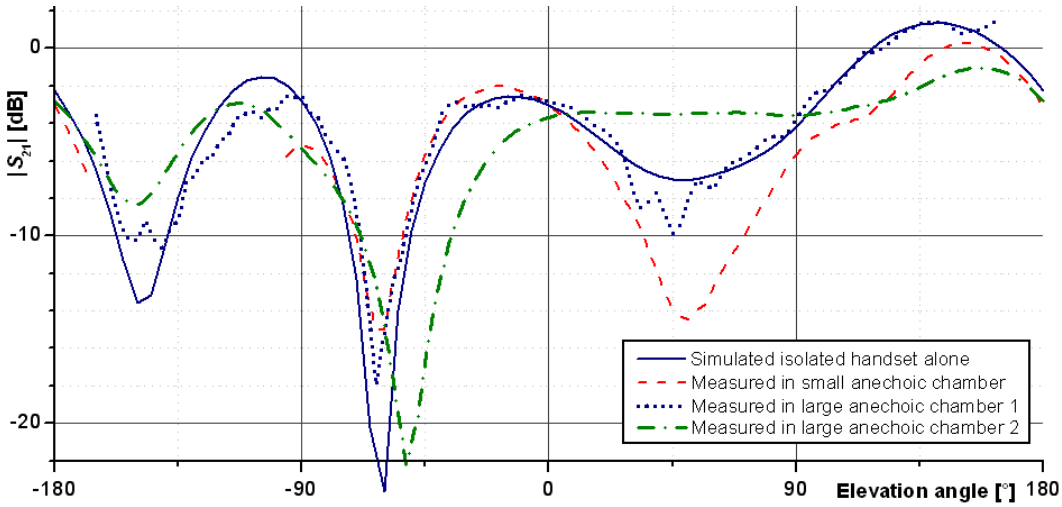

Figure 42: Far-field pattern comparison, *xz*-plane cut, E_θ polarisation, f = 1795 MHz

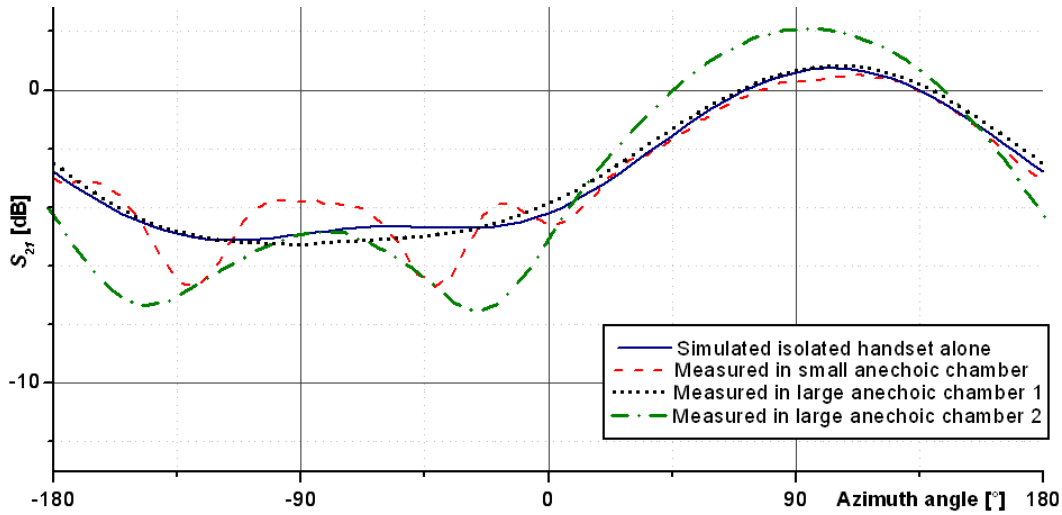

Figure 43: Far-field pattern comparison, *xy*-plane cut, E_θ polarisation, f = 1795 MHz

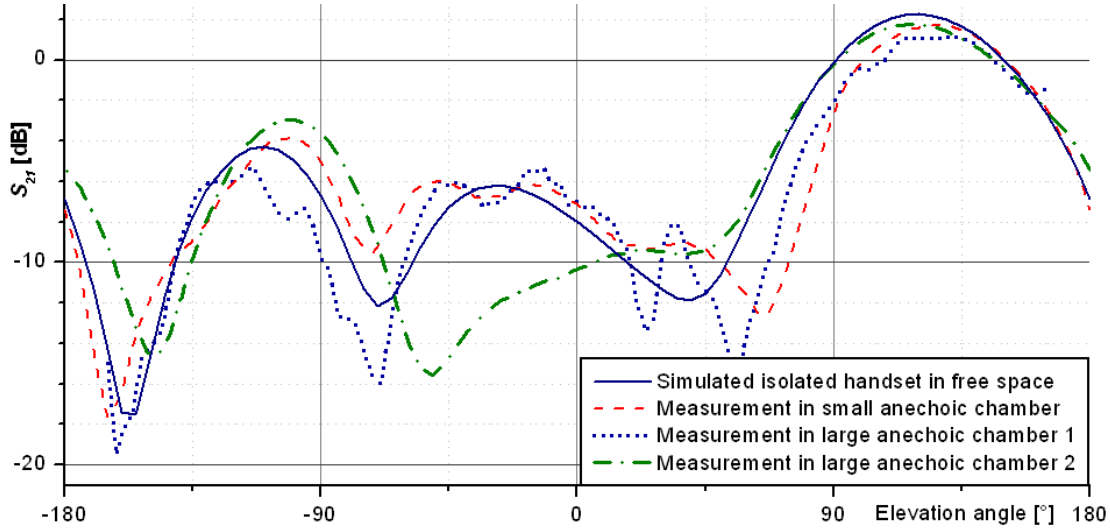

Figure 44: Far-field pattern comparison, *yz*-plane, E_θ, f = 1885 MHz.

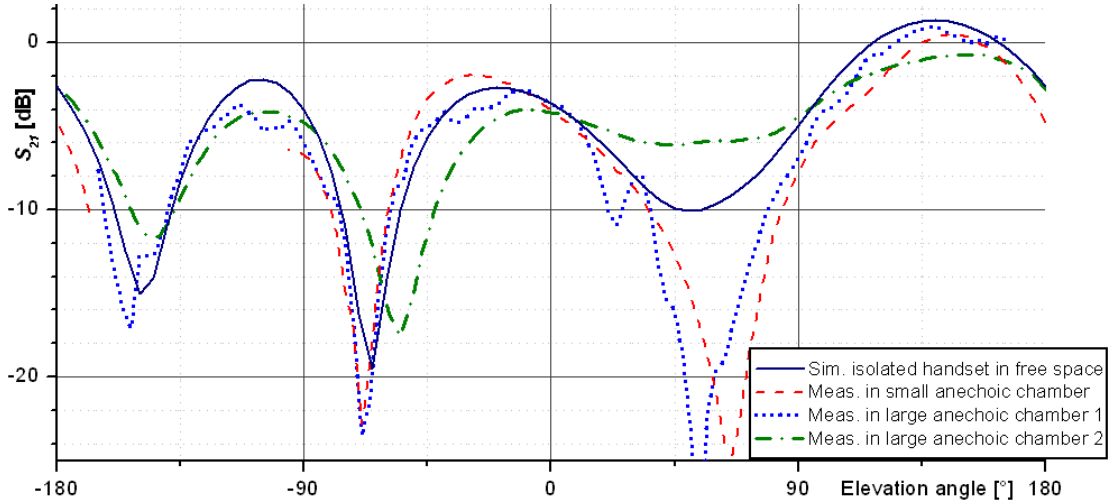

Figure 45: Far-field pattern comparison, *xz*-plane, E_θ, f = 1885 MHz

As mentioned above the small anechoic chamber was designed to allow EMC measurements down to 100 MHz, so the size of the RF absorbers lining the walls is larger than would be necessary to provide a high enough field homogeneity for measurements only above about 800 MHz. Above 800 MHz the return loss of RF absorbers with a height of 500 mm is better than 40 dB and the performance does not improve considerably with height anymore. Therefore, by replacing the largest absorbers (910 mm height) with shorter ones (500 – 600 mm height) a smaller footprint of the chamber of for instance 2.50 m × 1.80 m and a height of 1.80 m should be possible without a considerable increase in uncertainty above 800 MHz. Hereby basically a portable, table-top sized chamber would be possible to design for use with small-antenna measurements, e.g. during an experimental design process as described above.

5. Quarter-wave cap: a means for decreasing the influence of RF cables

In this chapter solutions to the problem of measurement cables attached to small antennas or mobile handsets are presented. RF cables are used to connect both the measurement antenna and the AUT to a network analyser in order to obtain the complex transmission coefficient between the antennas, and also the reflection coefficient at the antenna input port(s). The RF feed cables can cause considerable changes in the input impedance and in the radiation characteristics of the AUT when contrasted with the case of the antenna ideally floating in free-space as was discussed in Chapter 2. Although baluns are band-limited they are a valuable means to minimize the effect that the leakage currents along the RF cable have on the antenna radiation. Current and future mobile handsets operate at two or more frequency bands. Measuring the radiation characteristics of the multiple-band antenna by conveniently performing one wide frequency sweep requires multi-frequency baluns as were introduced in [41].

This chapter begins with a description of the mechanisms and design of the single-band balun. Then the design of a dual-band balun is presented that was the basis for a prototype of a dual-band balun. Computer simulations and measurements were performed with the prototype and the results of a comprehensive study of the effects on the current distribution of the handset and of the RF cable, as well as on the far-field radiation patterns are presented in this chapter. The performance and applicability of the dual-band balun in two different measurement set-ups is shown, namely in measurements of the far-field pattern and in near-field/SAR measurements. The balun is also compared with the commonly used ferrite beads, and it is shown that the balun provides a new improved means to significantly decrease uncertainty in small-antenna measurements.

5.1. Single-band balun

The need to provide a balanced-unbalanced transformation in measurements of dipole-like (balanced) antennas that are connected to a coaxial (unbalanced) RF cable has been mentioned e.g. in [4, pp. 43-25 – 43-27], [5, pp. 217 – 220] and [6, pp. 38-40] where under the designation ‘balun’ a quarter-wave sleeve is proposed for stopping undesired currents on the shield of the coaxial RF cable. The big advantage of using several sleeve-like chokes along the feed cable in order to decrease its scattering area was first mentioned in [37], where also the typical bandwidth of 10 % was stated for this narrow-band device. The ability of a quarter-wave sleeve placed on the antenna feed cable close to a mobile radio unit or handset to stop the surface currents from accessing the feed-cable surface at the connection to the handset was mentioned in [60] and also utilized in [38] in input-impedance measurements over a very narrow band (1%). In either case the mechanisms and effects in the balun device, or its design parameters or exact dimensions were not investigated further. It

was not until in [39] and [40] that the balun was thoroughly investigated for the effects of its dimensions and its placement on the RF cable and that it was optimised for its usability in radiation measurements of mobile handsets.

The basic idea of the balun is to introduce an "open end" at the edge of the DUT by placing a short circuit on the shield of the coaxial RF cable at a distance $d = \lambda/4$ from the edge of the DUT. The balun acts as such a short-circuit on the single-wire transmission line that the RF cable shield represents, i.e. for a specific frequency this transforms into an open termination at the edge of the DUT. With the balun the current distribution on the DUT and its radiation characteristics stay unperturbed compared to the case of the DUT floating in free space [39]. The same effect can be observed at *odd* multiples of the base frequency. The balun does not introduce losses to the radiating platform as opposed to ferrite chokes that are a well-known means to reduce unwanted radiation from cables in the field of electromagnetic compatibility (EMC), but are also widely used in antenna measurements.

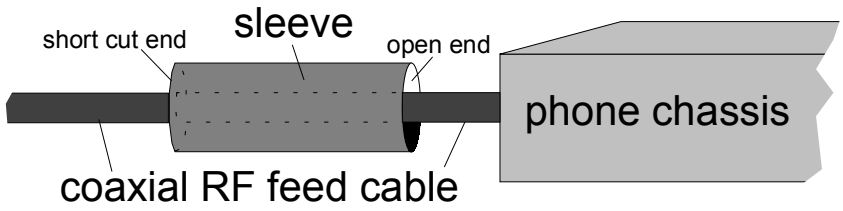

Figure 46: Set-up of the sleeve-like balun on the RF cable attached to the DUT.

A quarter-wave balun utilises this principle of impedance transformation. A coaxial sleeve is placed on the feed cable close to the connector. The end of the sleeve towards the DUT is open and the far end is short-circuited to the cable surface (see Fig. 46). A simpler short cut, namely a conducting circular plate on the cable, does not appear to be so useful, because currents can overcome the obstacle unless its diameter is more than about 5 - 6 cm, i.e. so large that it shadows a large sector of the 3-D radiation pattern. By folding this plate towards the DUT this problem is overcome, even though the blocking bandwidth decreases. The balun acts as a short-circuit located at $\lambda/4$ from the connector, i.e. for a specific frequency we get an open termination at the edge of the DUT, so the current distribution on the DUT resembles much better the current distribution in the case of the DUT floating in free space [39].

Especially at frequencies above 1 GHz a balun is much easier to implement than to find suitable ferrite material for chokes. The simulations in Section 5.1.1 show that the influence of the cable is reduced considerably by using such a balun. The shield of the RF cable beyond the balun can be covered by absorbing material to decrease also the spurious reflections by it. However, the main effect of the balun is to act like an open termination, so the energy propagating towards the feed cable is not only absorbed but reflected back towards the handset as if no cable were present. Therefore, the power radiated by the handset-antenna combination is not decreased like when lossy material is involved.

5.1.1. Computer simulations

To evaluate the performance of the balun compared to traditional ferrite beads, 3-D field simulations were carried out for a typical antenna-measurement set-up [39]. A commercial Finite Element Method (FEM) based software (Agilent HFSS) was used. The model of a handset-antenna combination consisted of the chassis with dimensions $h \times w \times t = 100$ mm $\times$ 40 mm $\times$ 10 mm, plus a l_a = 20 mm long, dielectrically loaded monopole antenna (see Fig. 47), resonant at 1 GHz and placed at a typical position on the handset. This monopole was used instead of the common helical antenna to simplify the geometry in the computer model. The radiation of the handset alone was simulated as reference. Then a 2.4 mm-thick metal stub of 160 mm length was added at the bottom to model the shield of the coaxial RF feed cable.

Next, a ferrite bead (l = 80 mm, d = 20 mm) was consecutively placed at four positions. The ferrite material had a relative permittivity ε_r' = 50 and relative permeability μ_r' = 50, and electric and magnetic loss tangents of 0.1. Finally, in several simulations 60 – 70 mm long caps with a diameter of 16 mm were placed on the cable. The gap between the handset bottom and the open-end of the cap was 10-20 mm. Thus, the effective distance between handset and the closed end of the cap was in all cases about quarter of the wavelength at 1 GHz (i.e. 75 mm).

For the evaluation two figures of merit were used, the total radiated power and the average of absolute differences between the far-field pattern and the case of the handset alone in free space. The pattern in the E-plane through x- and z-axes was chosen, as it is one of the patterns most likely to be affected by a change in the current distribution on the handset.

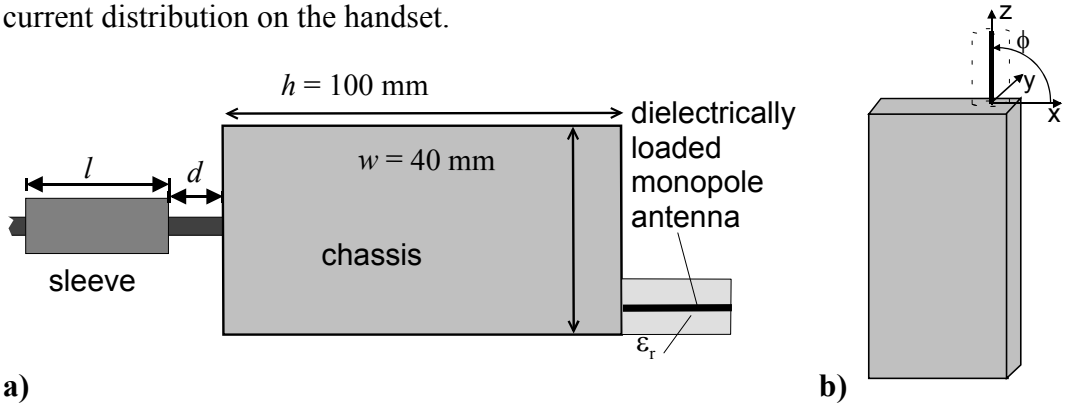

Figure 47: a) Dimensions of simulated set-ups. The resonance frequency of the antenna is $f_{res.}$ = 1 GHz. The cable stub is attached to the bottom plane of the chassis. b) The coordinate system used in Figs. 48 and 49.

The results show that the influence of the cable stub, in this comparison with the ferrite beads, is best eliminated by the cap. In Table 3 one can see that with the 160 mm cable attached to the handset the matching and thus total radiated power is close to that without a cable, but the error in the pattern is very large due to the currents induced on the cable. In case ferrites are used to eliminate these currents of the cable shield, the error in the pattern is slightly lower, but the ferrites absorb much of the power. When we now look at the cap with the use of the cap both radiated power and

the pattern are comparatively close to the reference case. The small changes in the radiated power are within the numerical accuracies. The cases cap 2, 3 and 4 in Table 3 show best agreement with the reference case. It should be noted that in those cases the shorted end of the cap is at $d = \lambda/4 = 75$ mm (or $d = 80$ mm in case cap 3) away from the handset, which seems to be the best selection. The total radiated power is generally in the range of the reference case. This could be expected as the lossy material is situated only on the cable shielding beyond the cap were only a small part of the power propagates. In Figs. 48 and 49 the E-plane pattern for a few cases is shown to visualise the effect of the different measures. It can be seen that the cap results in the radiation pattern closest to the reference. The sensitivity to variations in length, position or diameter of the cap is relatively small. Still the dimensions can be optimised and tested with different handset models to show their general applicability. To investigate the bandwidth of the cap cases cap 2 and cap 4 were simulated with a dipole resonant at a 5% higher frequency. It was found that compared to the reference case with a handset alone the errors in the E-plane radiation patterns are in the same range for the two given cases (see Table 4), and the error in the total radiated power increases only slightly to around 0.5 dB.

Table 3: Two figures of merit - the total radiated power and the average of differences in the far-field pattern in the E-plane, compared to the reference case. f = 1 GHz.

Simulated case (l [mm], d [mm])	$P_{rad,tot}$ [dBm]	avg|ΔE_{far}[dB]| [dB]
handset alone (reference)	28.7	0
with 160 mm feed cable stub	28.6	3.29
with ferrite 1 (80, 30)	26.9	2.80
with ferrite 2 (80, 75)	26.6	3.22
with cap 1 (60, 10)	28.9	1.64
with cap 2 (60, 15)	28.7	1.41
with cap 3 (60, 20)	28.9	1.04
with cap 4 (65, 10)	28.6	1.63
with cap 5 (65, 15)	28.9	1.90
with cap 6 (70, 10)	28.4	2.14
with cap 7 (60, 15, ∅=20)	28.8	1.87

Table 4: Two figures of merit for two cases at $f_{+5\%}$ = 1.05 GHz.

Cases (l [mm], d [mm])	|$\Delta(P_{rad,\,tot}$[dBm])| [dB]	avg|$\Delta(E_{far}$[dB])| [dB]
cap 2 (60, 15)	0.25	1.07
cap 4 (65, 10)	0.54	2.38

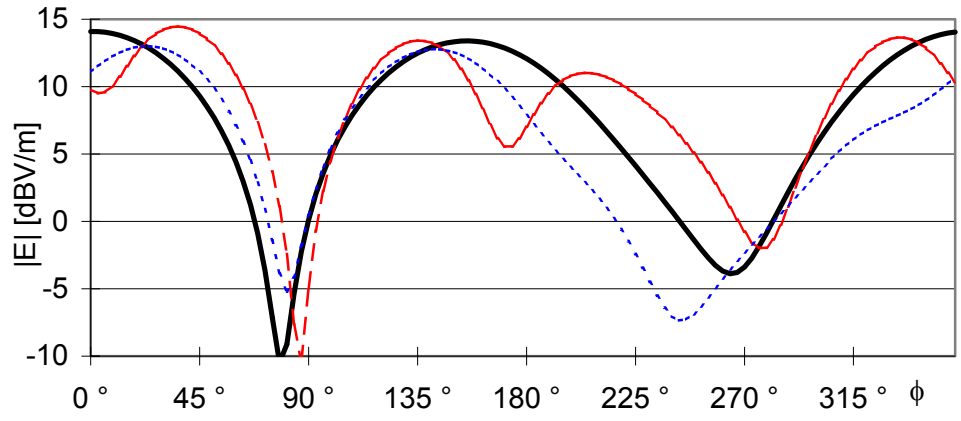

Figure 48: Simulated *zy*-plane radiation patterns at 1 GHz: |*E*| at 1 m distance, handset alone (solid), handset with 2.4 mm thick, 160 mm long cable (dashed), and a ferrite bead (*l* = 80 mm, ∅ = 20 mm, ε_r = 50-*j*5, μ_r = 50-*j*5) attached to cable at *d* = 30 mm (dotted).

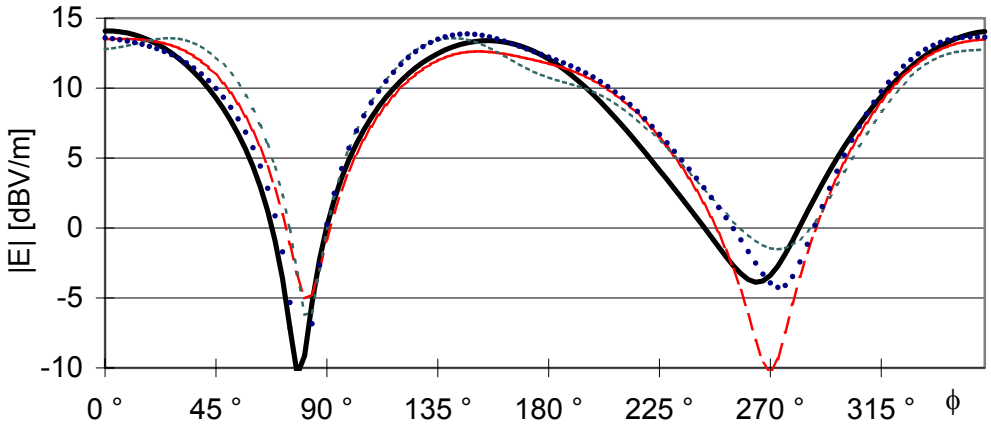

Figure 49: Simulated *zy*-plane radiation patterns at 1 GHz: |*E*| at 1 m distance, handset alone (solid), handset with 2.4 mm thick, 160 mm long cable plus cap 2 (*l* = 60 mm, *d* = 15 mm, dash-dot), cap 3 (*l* = 60 mm, *d* = 20 mm, dots), and cap 4 (*l* = 65 mm, *d* = 10 mm, dotted).

5.1.2. Optimisation

After having simulated only a limited amount of possible designs for the balun, the aim is now to more thoroughly optimise the size and the position of the sleeve, in order to obtain a good design for the prototype. The finite element method code that was used in Section 5.1.1 is too time-consuming when it comes to frequently changing the model of the measurement set-up. Also, the calculation time increased considerably when the set-up was modelled with a longer RF cable than in Section 5.1.1, and a longer cable stub would result in a better description of the real case with an arbitrarily long measurement cable.

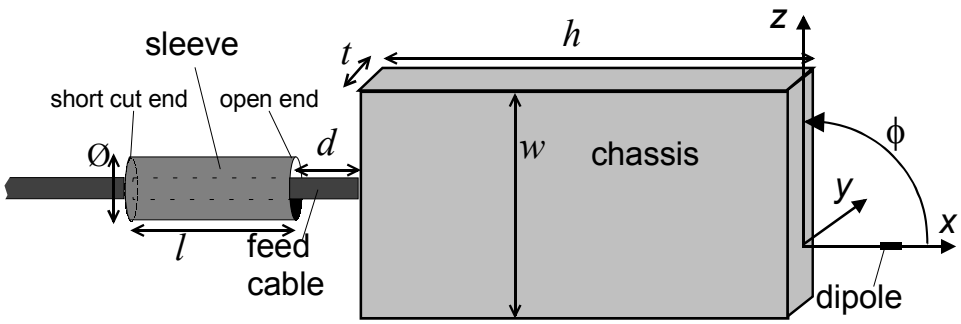

Figure 50: Mobile handset with feed cable, sleeve, and current dipole at location of antenna. Coordinate system used in Fig. 52

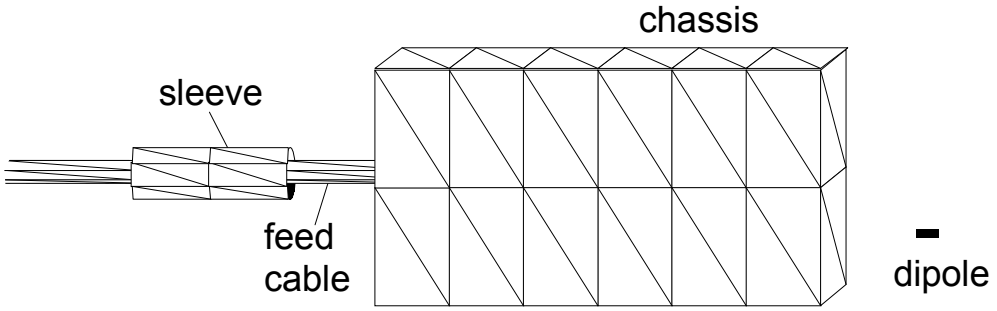

Figure 51: Principle representation of the triangular mesh for the handset model simulated at 1 GHz. The actual mesh consists of 360 triangles. The cable continues to the left to a length of m_0 = 600 mm.

For the E-field calculations a method of moments (MOM) code was developed using the electric field integral equation (EFIE). The code was based on the theory described in [61], [62], and [63]. The basic Matlab code was made available by the authors of [63]. The surface model for the handset, including cable and sleeve (Fig. 50) was then implemented with 360 planar triangular surface patches (see Fig. 51). A set of basis functions is used, where each basis function is defined on a pair of adjacent triangular patches. The excitation of the model is done by a current dipole point source, located where the tip of a typical helix antenna is located on a real handset, i.e. 15 mm from the upper end of the chassis (see Fig. 51). The initial boundary conditions for the MOM code are given by the currents on the surface of the object, which are directly induced by the current dipole.

The handset model is characterised by conducting surfaces. The model includes the rectangular box of the handset chassis with the same dimension as used in Section 5.1.1 and in [39]: h = 100 mm, w = 40 mm and t = 10 mm. The RF feeding cable is 600 mm long, and the coaxial sleeve on the cable has variable size and position. The sleeve is defined as an infinitely thin conducting sheet.

The MOM code is used to calculate the current distribution on the triangular patches. From the current distribution the radiated far-field pattern at any point in space can be obtained by superposition of the radiated fields from all current sources on the model surface.

However, one drawback of the MOM code is obvious if we look at the finite length of the feed cable. A typical feed cable during a measurement is several meters long

and after some 1 – 2 m from the device under test it is situated in an arbitrary orientation, possibly lying on or behind absorbing material, and finally it reaches a feed-through leading out from the shielded room. In the MOM calculation a straight cable with a certain length has to be chosen. Only a length of less then 1 m can be simulated with a reasonable use of resources and time for a PC, despite the fact that Dr. M. Popov contributed some final modifications to the E-field simulation Matlab code, thanks to which the code ran about 10 times faster than the un-optimised code. According to [53, pp. 489 – 496] the losses along a travelling wave antenna are small and a long wire with a badly matched termination will cause reflections from the termination and create a standing wave radiation pattern. In the simulations for any length of the cable the termination of the cable stub is inherently an open end, as the implementation of lossy material is not possible in this EFIE code. Therefore, the reflection coefficient at the cable end is $|\rho| = 1$ causing resonances and standing waves on the cable. Such a resonance can result in an especially high radiation. Thus, a good position of the sleeve might be rejected because that specific length of the cable behind the sleeve happens to support a resonance in the surface current on the cable. A solution to this problem is to vary the length of the cable and take an average of the radiation as described in the following.

The aim is to formulate a design problem for the position, the length and the diameter of the sleeve, which provide the best match between the perturbed radiation pattern calculated with an attached cable and the reference field calculated without any cable attached to the handset. The optimisation of the sleeve should also consider its desired independence of the RF cable length and location, the desired effective bandwidth, or the used kind of handset antenna, which leaves us with a large number of variables. Therefore, it seems reasonable to use a global optimisation method like a genetic algorithm (see e.g. [64], [65]).

Genetic algorithms are based on Charles Darwin's theory of the natural selection. The basic building blocks in a genetic algorithm are genes. A gene is one bit in a binary chromosome encoding the parameters. In our case each chromosome encodes the position, length and diameter of the sleeve. Each chromosome is associated and ranked with a value from the objective functional. In each iteration a new set of chromosomes is created that basically consist of parts of the highest ranked chromosomes and with a few occasionally mutated genes. After ranking, selection, crossover, and mutation of the chromosomes in each iteration, the global minimum is obtained after a number of iterations ([64], [65], and [66]).

As the first step in the optimisation algorithm, a suitable objective functional is introduced to be able to rank the chromosomes. The MOM code is used to calculate the radiation pattern in one significant *E*-plane cut. The cut through the *xz*-plane is sufficient as it includes the whole dynamic range of the handset radiation. The objective functional is the mean square error between the calculated perturbed pattern and the unperturbed reference pattern. The pattern is calculated in the *xz*-plane for $0° \leq \phi \leq 360°$ in 3° steps. When evaluating the far-field radiation pattern of the modelled handset, the parameter sets are ranked according to their objective

functional values. The genetic algorithm finds the parameter set with the minimal objective functional value.

The genetic algorithm requires a discretisation of the search space, i.e. of the position and dimensions of the sleeve. Therefore, an exact absolute minimum is generally not obtained, unless a very fine discretisation is chosen. The present optimisation case does not require a very fine discretisation, as the changes in the radiation pattern are rather smooth. A distance of 2 mm was chosen for the discretisation step for the length and location of the sleeve, and 1 mm for that of the diameter. If a more accurate design for the parameters is required, a gradient method can be employed to make a finer search.

The above mentioned effect of cable length related resonances and standing waves has been reduced by the following method: Each evaluation of the objective functional includes the solution of the MOM code for five cases instead of one, i.e. the radiation patterns for five different cable lengths are calculated: The original cable length of m_0 = 600 mm, and four varied cable lengths $m_n = m_0 + n \times \lambda/10$, where n = ±1, ±2. The corresponding five complex radiation patterns are added up in the objective functional before averaging the differences from the reference case. Hereby, possible cable length-dependent narrowband resonances do not affect the results as much.

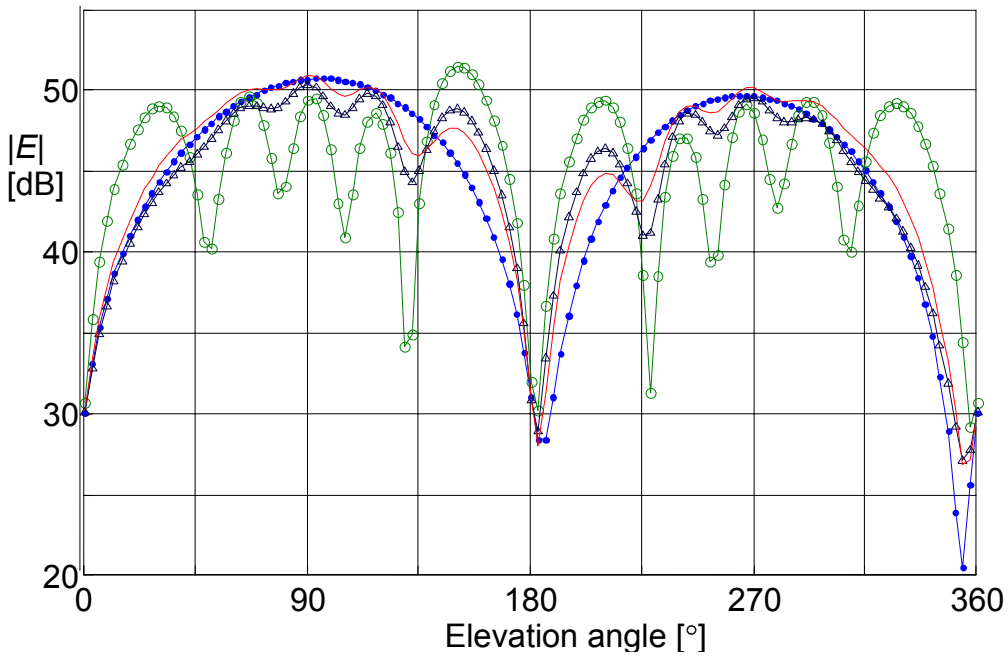

Figure 52: Simulated electric field strength at 10 m distance from source. The solid line indicates the complex sum of the radiation patterns with five slightly different cable lengths, the reference case without any cable attached is denoted by dots, and the far-field pattern with a 600 mm long cable attached and no sleeve is marked with circles. Additionally, the radiation pattern based on the balun dimensions proposed in Section 5.1.1 and in [39] is shown with triangles.

After the optimisation of the sleeve design, the optimal diameter of the sleeve is Ø = 13.8 mm, the optimal length of the sleeve l = 63.7 mm. The optimal distance of the open side of the sleeve to the bottom of the chassis is d = 28.1 mm. This means the distance between the short cut end of the sleeve and the chassis of the handset is $l + d$ = 91.8 mm, i.e. significantly more than λ/4 (= 75 mm), which was the first guess used in Section 5.1.1 and in [39], where the proposed optimum dimensions were l_0 = 60 mm, $Ø_0$ = 16 mm, d_0 = 15. That previous case results in a worse agreement with the reference case (see Fig. 52) because no optimisation had been used.

5.1.3. Design and application

The use of a quarter-wave single-band balun was discussed and optimised in [39] and [40]. The effective bandwidth at the centre frequency of the balun was about 10%. General instructions for the design, optimisation and construction of baluns for small-antenna measurements were given. Based on computer simulations it is relatively easy to design a balun optimised for one specific frequency range. Fig. 53 shows the dimensions of a prototype of a balun designed for 2 GHz.

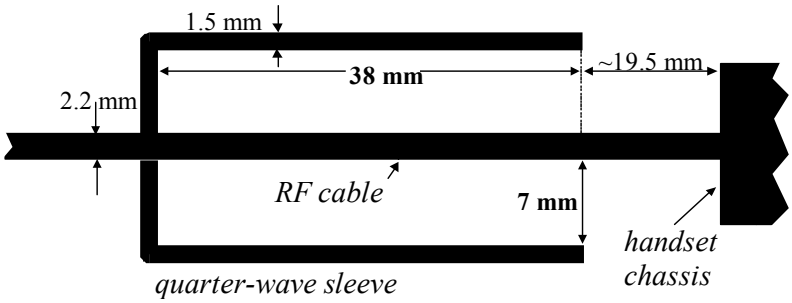

Fig. 53: Cross-section of a mobile handset with RF feed cable and a 2 GHz single-band balun.

Generally, the effect of electromagnetic fields scattered or reflected by the RF cable can still cause a considerable error in the measured radiation pattern, even when one balun is used. By placing lossy or absorbing material around the RF cable behind the balun, also this scattering effect can be reduced to an acceptable level. Again, merely using lossy material to cover the RF cable without the use of the balun would result in a drain of energy from the surface of the handset and thus in a reduced total radiated power as was also shown in [39]. The use of 2 or even 3 quarter-wave baluns in a row can reduce this near-field effect, as well as the scattering of fields (see Fig. 54). The best effect can be reached when baluns are placed so close to each other that they virtually cut the RF cable into small pieces, too short to act as resonating dipoles. The scattering area as a function of the length of a cable segment has been investigated in [37], and it was found that the worst case is when the length of the segment is about λ/2 or larger than 1.3λ, while a cable segment shorter than about 0.4λ is no significant scatterer anymore. Therefore, when placing the second (and third etc.) balun the wavelengths of both resonance frequencies in question have to be carefully considered, in order to obtain the best possible segmentation of the cable.

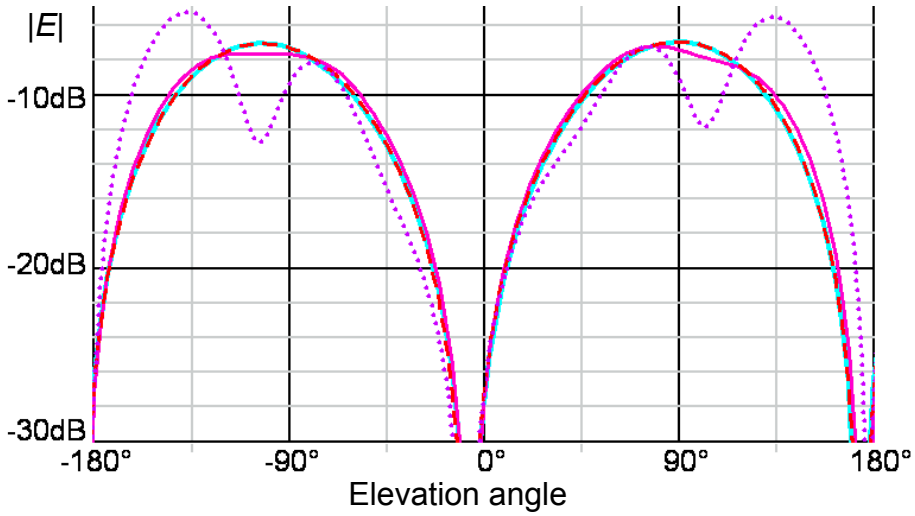

Figure 54: Simulated *yz*-plane pattern at 920 MHz, short current dipole mounted on the corner of an 80 mm long handset, isolated handset —, handset with cable · · ·, with 1 balun —, 2 baluns in a row - - -.

Despite all the mentioned measures, on a conical sector of several degrees in the direction of the cable no reliable radiation pattern can be obtained due to the shadowing effect of the balun and the RF cable. This is the reason why the diameter of the sleeve has to be kept small, although the blocking effect of the sleeve improves with an increasing diameter. It is recommendable to place the RF cable (with the balun) in the expected direction of the lowest lobe or pattern null to loose only less significant pattern information. This direction may in terms of vertically polarised mounted antennas seem like the worst possible place to attach the RF cable to the handset as the cable must be placed in the same polarisation as the AUT and is thus most prone to cause interferences in the measured patterns. However, the bottom feed is the most convenient feed configuration e.g. for the 3-D spherical scanning systems that include a phantom head or torso, because these systems can use a rotary joint and thus the axis-aligned cables can be kept 'stationary'. When using a side feed in these systems there are moving cables that can cause mechanical problems. Nevertheless, the way the sleeve balun works makes the measurement set-up independent of traditional rules of thumb, like trying to place the RF cable perpendicular to the polarisation of the AUT (to reduce the direct coupling) or placing the connector for the RF cable at a location on the AUT/handset where a low current density can be expected (to reduce leakage of currents) as was proposed in [37]. Due to the fact that the direction in which the RF cable points is inevitably the one that is excluded from the scanning surface, with these avoiding strategies one typically loses information in a major side lobe if not the main lobe. In those cases the shadowing effect of the balun is more significant, too. Nevertheless, in simulations the balun proved to work also for those measurement set-ups.

5.2. Dual-band balun

5.2.1. Dual-band balun, design 1

With some modifications in the geometry of the single-band design, the balun can be used as a dual-frequency balun (Balun 1). The application of the following design for use in small dual-band antenna measurements was first presented in [41]. Extending the idea of impedance transformation we now consider a half-wavelength long tapered coaxial cylinder around the RF feed cable. The cylinder is open on both ends, but very small in diameter at the end pointing away from the handset (see Fig. 55). This way an abrupt change from low to high wave impedance is imposed at the narrow end of the coaxial cylinder. When placing this impedance step half a wavelength away, it is transformed into a high impedance at the connection of the RF cable to the handset. As in the case of the quarter-wave balun the RF cable surface becomes practically inaccessible for the surface currents from the handset. The advantage over the quarter-wave cap is, that the effect can be observed also at *even* multiples of the lowest frequency. For measurements of mobile handset antennas that operate at 900 MHz and 1800 MHz this is a useful feature.

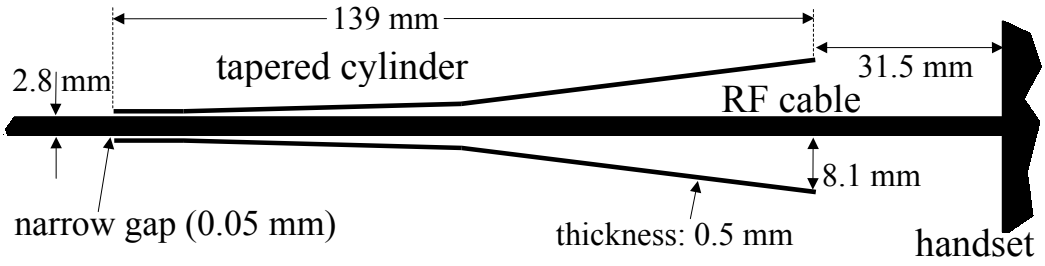

Fig. 55: Cross-section of dual-band balun 1, indicating its location on the RF cable.

The inner diameter of the narrow end of the cylinder is 2.9 mm. The diameter of the cable is 2.8 mm. The step in the wave impedance at the end of the coaxial cylinder is therefore from 2Ω to a considerably higher impedance of the single wire line that the shield represents. Initially, the tapering of the cylinder was chosen linear, plus a 5 mm piece of cylinder with constant diameter at the narrow end. The parameters length, wide-end diameter of the tapered coaxial cylinder, and the distance from handset have been optimised with help of a genetic algorithm [39] at 1 GHz and 2 GHz. Subsequently, the small bandwidth of the balun has been improved with a FEM software package, i.e. by changing the tapering to an exponential one and adjusting the length.

The results in Fig. 57 and Fig. 58 show that the perturbation of the far-field radiation pattern is reduced significantly at 1 GHz and at 2 GHz. The bandwidth of the balun is about 10% at 1 GHz, and about 5% at 2 GHz. The two frequency bands can be changed by designing the tapering and the dimensions of the balun appropriately, e.g.

with help of computer simulations. For practical reasons this rather difficult-to-construct design was not further investigated nor prototyped.

5.2.2. Dual-band balun, design 2

Alternatively, by folding the coaxial sleeve into two coaxial layers a more compact design is achieved (Balun2). This design is not only much easier to construct than design 1, but also more useful when building a short cable extension containing the balun, to be inserted between the RF measurement cable and the AUT. Secondly, at the connection of the inner and outer cavity a narrow radial gap is introduced. The capacitance of the gap acts as a series low-pass filter that cuts off the outer cavity for high frequencies and makes it accessible only for lower frequencies.

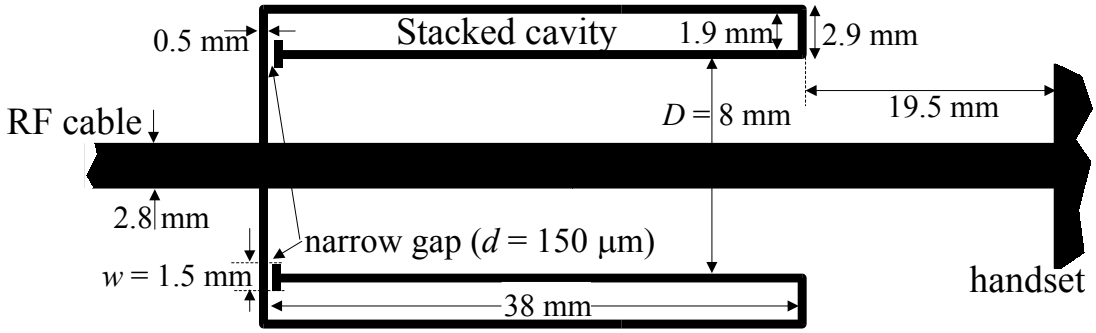

Fig. 56: Cross-section of dual-band balun 2, indicating its location on the RF cable.

Figure 56 illustrates the geometry and the dimensions. The capacitance of the gap basically acts as a low-pass filter, so for high frequencies the outer cavity is blocked away, and the inner cavity is the active quarter-wave balun. At low frequencies the outer cavity is added to the inner one, so the effective quarter-wave cap is twice as long. In this design capacitance of the circular-gap is approximately that of a plate capacitor with a width w = 1.5 mm, length $l = \pi D = \pi \cdot 8$ mm ≈ 26 mm, and d = 150 μm is the gap width, so that $C = \varepsilon_0 w \pi D/d \approx 2.3$ pF.

In computer simulations the bandwidth of the balun is about 10% both at 1 GHz and at 2 GHz. The two frequency bands can be adjusted for the antenna under test by changing the inner and outer diameters and the length of the stacked balun, and by changing the gap width appropriately.

Figs. 57 and 58 show the H-plane radiation patterns at the centre frequencies of the baluns, i.e. at 1 GHz and 2 GHz, respectively. The absolute signal levels seen in the plots are arbitrary, as produced by the FEM software package. However, the relative levels of the different simulated cases are normalised to the same total radiated power.

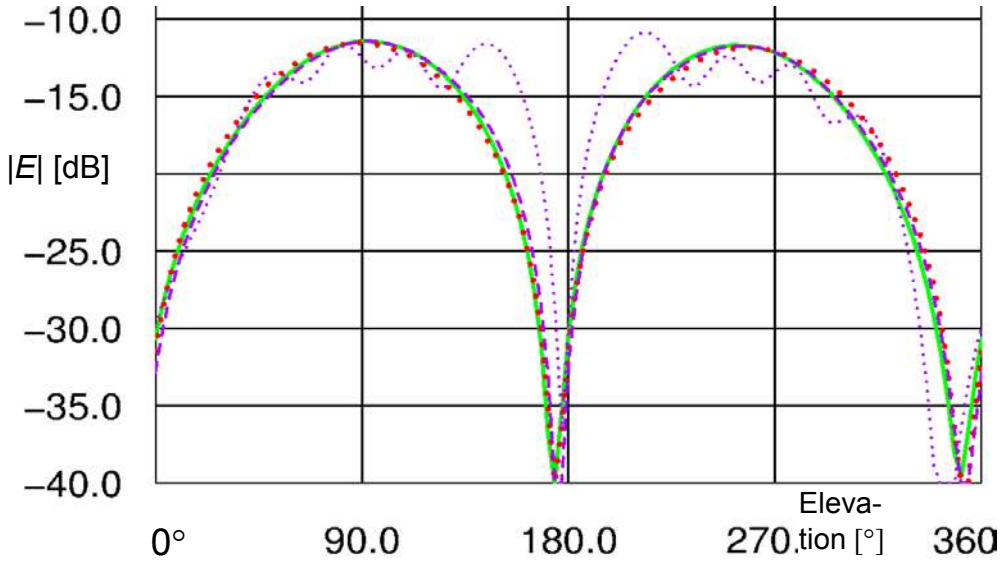

Figure 57: The H-plane radiation pattern at 1 GHz. Balun 1 is indicated by large dots, Balun 2 by a dashed line, the reference case without any cable attached is denoted by a solid line, and the far-field pattern with a 500 mm long cable attached and no balun is marked with smaller dots.

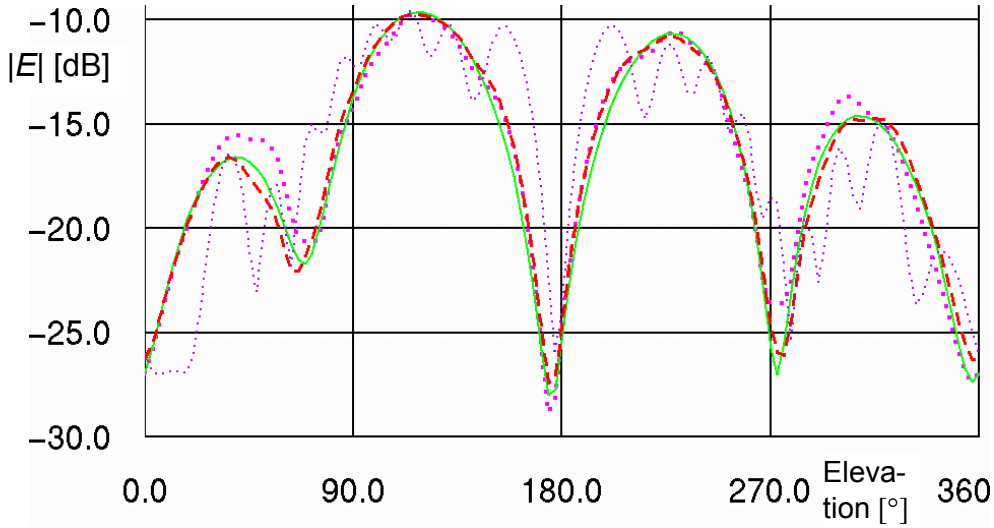

Figure 58: The H-plane radiation pattern at 2 GHz. Balun 1 is indicated by large dots, Balun 2 by a dashed line, the reference case without any cable attached is denoted by a solid line, and the far-field pattern with a 500 mm long cable attached and no balun is marked with smaller dots.

The RF cable attached to the handset perturbs the radiation pattern. At 1 GHz with either one of the balun designs the field perturbations are decreased by more than an order of magnitude, i.e. from more than 10 dB down to less than 1 dB. At 2 GHz Balun 2 is as effective as at 1 GHz, but Balun 1 is not quite as effective, i.e. perturbations up to ±2.5 dB occur in the two minor lobes.

The bandwidth of Balun 1 is 10% at 1 GHz, and 5% at 2 GHz. For Balun 2 the bandwidth is 10 % both at 1 GHz and at 2 GHz. The criterion for the bandwidth is

that the perturbation of the two dominant lobes caused by the RF cable, stays within ±2 dB, when compared to the radiation pattern without any cable attached to the handset.

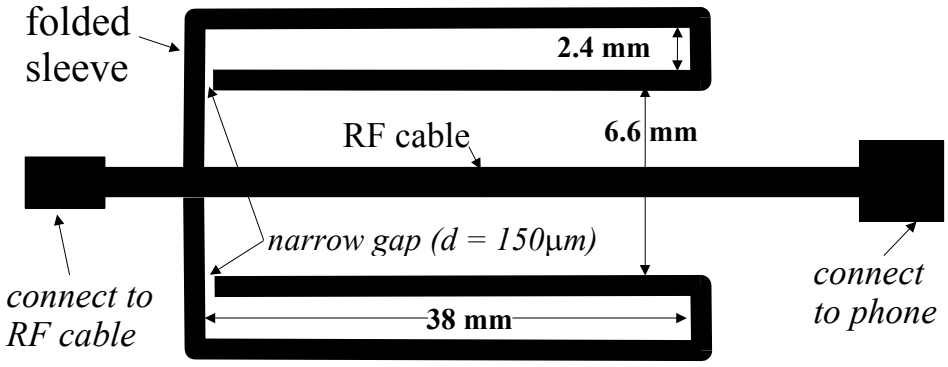

Fig. 59: Cross-section of the dual-band balun prototype, designed for the frequency bands around 920 MHz and 1795 MHz, wall thickness is 1.5 mm, RF cable thickness is 2.2 mm.

Fig. 59 illustrates the geometry and the dimensions of a prototype dual-band balun optimised in simulations for the centre frequencies 920 MHz and 1795 MHz, i.e. the GSM 900 and GSM 1800 bands. As opposed to the case of the single-band balun it is not anymore merely the length of the coaxial sleeves that determines the centre frequencies of the quarter-wave balun, but the widths of the two coaxial cavities and especially the capacitance of the gap. As a change of e.g. 10 % in width results in a shift of both centre frequencies by 1-2 %, the exact gap width is essential. Due to the apparent difficulty of constructing the 150-μm gap with sufficient accuracy, 6 tuning screws were inserted in order to fine-tune the gap capacitance after construction. The screws can be used to adjust the average width of the gap and therefore its capacitance. Four narrow Teflon rings were used to keep the parts of the balun in place during construction, i.e. the balun was actually composed of two brass tubes that were mounted on the RF cable stub and soldered together after having been carefully placed and adjusted.

This type of balun was originally designed for two frequency bands with a centre-frequency ratio of about 2, i.e. the two GSM bands at 900 and 1800 MHz. However, larger (e.g. 3 with a single-band balun) or smaller ratios (down to 1.4 has been successfully reached in simulations) can be designed while keeping a useful bandwidth, by changing the inner and outer diameters and the length of the stacked balun, and by changing the gap width appropriately. Also the bandwidth is dependent on the dimensions of the balun and the gap width. As the gap capacitance is basically a first-order filter the effective bandwidths at both frequency bands can be expected to decrease when the centre-frequency ratio decreases.

5.3. Computer simulations

Computer simulations were performed with a commercial Finite Element Method (FEM) code software package (Agilent HFSS). A model of the dual-band patch-antenna prototype according to [59] was placed in the coordinate system as shown in Fig. 60. Due to the limitations inherent in the time- and memory-demanding calculations, the RF-cable model had to be limited to a length of 150 mm, while its end was terminated with a matched port. This way only the influence of the cable-surface currents on the current distribution on the ground plane could be investigated, but not the scattering effects of the whole cable. These scattering effects could only be evaluated in measurements.

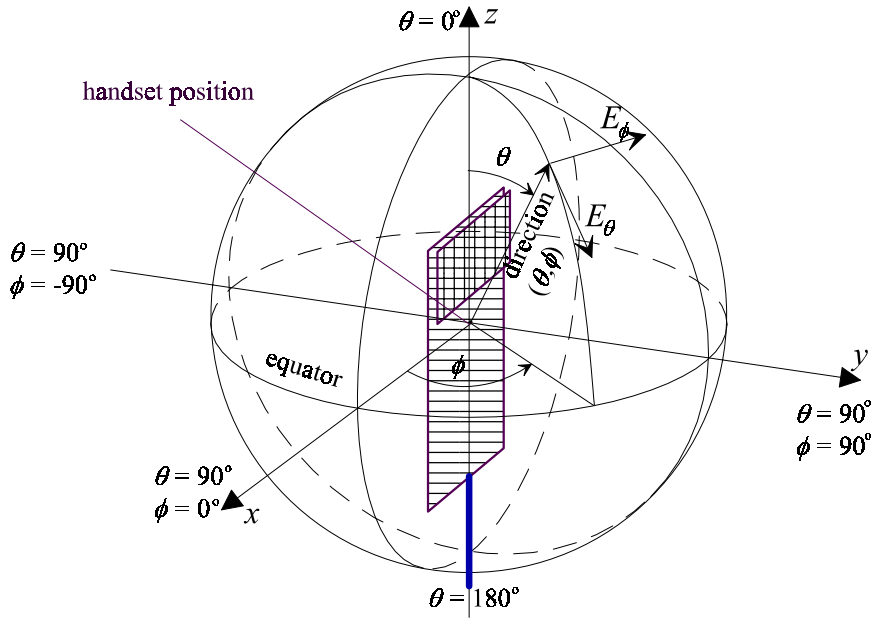

Figure 60: The dual-band patch antenna [59] in the standard spherical coordinate system [3, p. 16], as used in measurements/simulations. The patch points towards $\phi = \theta = 90°$, the cable towards $\theta = 180°$.

The following four cases were compared in the simulations:

S1) The reference case of a handset/patch floating in free space (isolated AUT),
S2) The handset with a short cable stub (150 mm long) attached to the bottom,
S3) A lossy ferrite bead placed on the cable stub 20 mm from the connector,
S4) The dual-band balun placed on the cable stub 20 mm from the connector.

From the calculated electromagnetic fields two parameters were extracted, 1) the far-field pattern in the two principal planes that lie in the *xz*- and *yz*-planes. These planes contain the most dynamics of the vertically polarised fields and therefore show perturbations of the radiated fields most clearly, and 2) the radiation efficiency to investigate the total losses in the system.

Figs. 83) and 84) shows the simulated *yz*-plane radiation pattern at the centre frequencies for which the balun (and the antenna) had been designed, i.e. 920 MHz and 1795 MHz. The ferrite bead used in the simulations was 51 mm long, had a diameter of 14 mm, and

was placed at the same position on the cable as the balun, i.e. at 18.5 mm from the edge of the chassis, a gap of 0.7 mm between the cable shield and the ferrite bead models an average air gap that usually occurs in the application of a ferrite cable snap due to the plastic cover of the RF shield and the fact that the ferrites are usually not available with inner diameters exactly suiting the RF cables. At 920 MHz the ferrite material had a relative permittivity $\varepsilon_r = 5 - j0.01$ and a relative permeability $\mu_r = 3.5 - j0.3$. At 1795 MHz the ferrite material had a relative permittivity $\varepsilon_r = 5 - j0.01$ and a relative permeability $\mu_r = 2.5 - j0.5$. Material properties of ferrite materials were investigated in [67], an average of two ferrite materials were used to model the ferrite material in the simulations. The absolute signal levels in the plots represent the antenna gain in dBi.

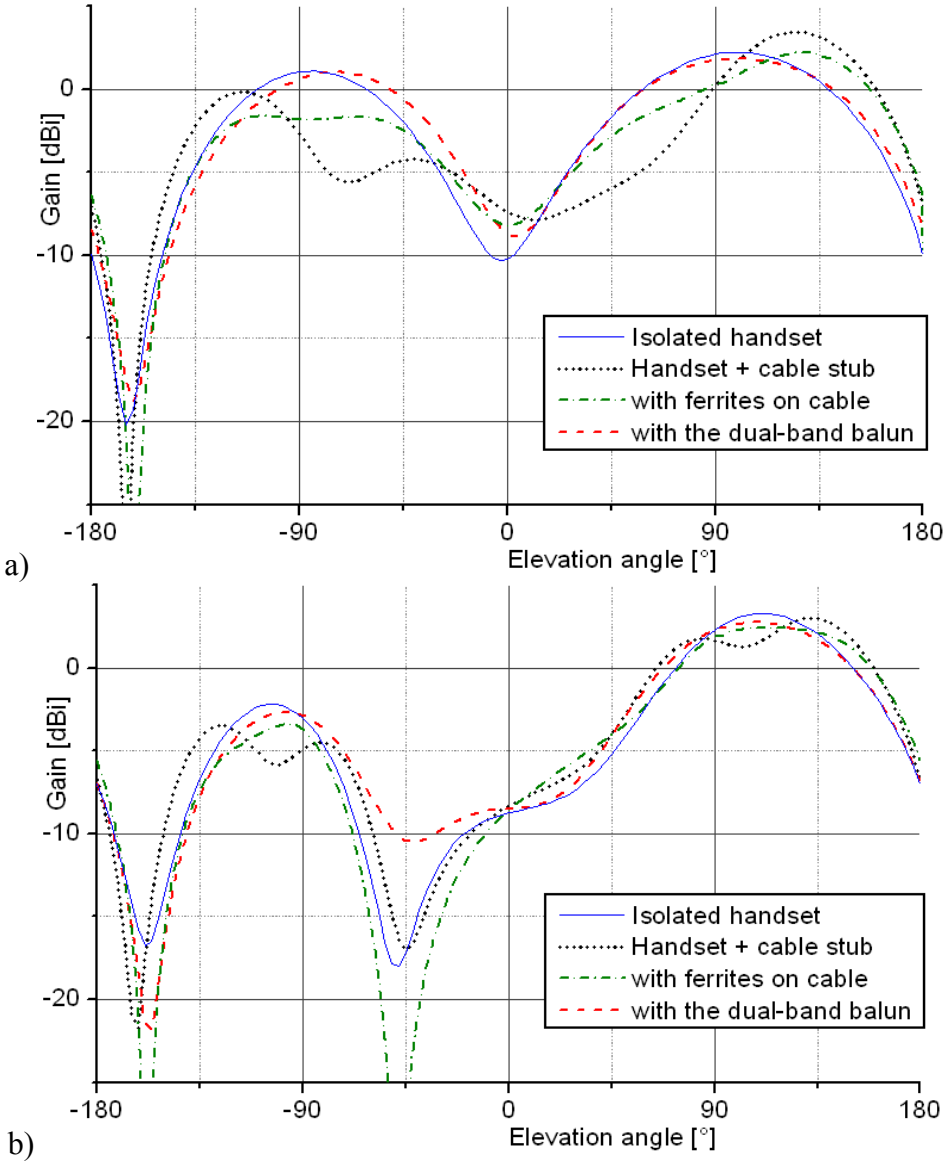

Figure 61: Simulated *yz*-plane gain pattern ($|E_\theta|$) at a) 920 MHz and b) 1795 MHz.

The results in Fig. 61 clearly demonstrate how much the RF cable perturbs the radiation pattern of the AUT when no measures are taken against leakage currents on the cable shield. The ferrite bead improves the situation noticeably at 920 MHz and

slightly at 1795 MHz. Both at 920 MHz and at 1795 MHz the balun prevents the field perturbations in the main lobes better than the ferrite bead.

Table 5: Antenna radiation efficiency for simulated cases S1 – S4 at 920 MHz and RMS of the absolute differences in the linear gain contrasted with the gain in case S1.

	S1:isolated handset	S2:handset with cable	S3: w. cable + ferrite	S4: w. cable + balun
Radiation efficiency	99.4%	91%	92%	99%
RMS of $\Delta E_{\theta,linear.}$ vs. S1	0	4.6%	2.9%	1.0%

Table 6: Antenna radiation efficiency for simulated cases S1–S4 at 1795 MHz and RMS of the absolute differences in the linear gain contrasted with the gain in case S1.

	S1:isolated handset	S2:handset with cable	S3: w. cable + ferrite	S4: w. cable + balun
Radiation efficiency	99.8%	99.8%	99.6%	99.8%
RMS of $\Delta E_{\theta,linear}$ vs. S1	0	2.2%	1.3%	0.9%

In Tables 5 and 6 the simulated antenna radiation efficiency (i.e. antenna efficiency corrected for the mismatch losses) of the AUT, as well as the relative error averaged over the *yz*-plane radiation pattern (from Fig. 61) in linear scale are given for 920 MHz and for 1795 MHz, respectively. According to [68] the relative error is best represented by the average root mean square (RMS) of the absolute differences in the linear gain contrasted with the gain in the isolated handset (Case S1). We can see especially at 920 MHz how much of the input power is dissipated along the cable or absorbed by the ferrite beads in case S3, while Case S4 with the balun is in best agreement with the reference case S1. At 1795 MHz the differences are much smaller but still Case S4 with the balun agrees best with the reference case.

Based on the simulations the relative bandwidth of the balun is around 10% both at 920 MHz and at 1795 MHz. The criterion for the bandwidth is that the perturbations in the main lobes are smaller than ±2 dB, when contrasted with the isolated handset (Case S1). These values were confirmed by the measurements presented in Section 5.5.1. It should be noted that the scattering effects of a long RF cable could not be included in the simulations, which explains the generally lower pattern errors in the simulations contrasted to those obtained in the measurements in Section 5.5.1.

5.4. Measurement set-ups

Measurements were performed with the tuned balun attached to a dual-band patch-antenna prototype measuring 30 mm × 40 mm × 7 mm mounted on a ground plane measuring 110 mm × 40 mm [59]. In the following this prototype is called DUT. The RF cable and the balun were attached at the bottom of the DUT, which is the end opposite of the patch antenna (see Figs. 60, 64 and 66). This can be considered to be the worst case in terms of field perturbations by the RF cable, i.e. by this choice the

best contrast for comparisons is obtained. The input impedance at the antenna input, far-field radiation patterns as well as the surface-current distribution on the ground plane and along the RF cable were measured.

5.4.1. Input impedance measurements

The set-up for the input impedance measurement was in a $1m^3$ absorber-lined cubical box ensuring a free-space like environment. With an RF cable, led through the absorbers, the handset antenna was connected to a network analyser and S_{11} at the antenna port was recorded. As a reference, input impedance and far-field pattern of the handset antenna were calculated with a 3-D-field-simulator software package. Compared to the simulated 6-dB bandwidth of 5.2 % for the isolated handset at 920 MHz, the measured 6-dB bandwidth was decreased by the RF cable to 4.4 % whereas when the balun was attached to the cable the bandwidth was 5.3 %, which is close to the simulated 6-dB bandwidth. However, additional resonance effects were encountered in the input impedance that suggest a more direct influence of the balun resonance on the antenna resonance. As a thorough discussion of these effects on the resonance characteristics of the patch antenna shall not be the subject of this paper, it is mentioned here for completeness, but should be noted when performing impedance measurements.

5.4.2. 3-D pattern measurements

The measurements of the 3-D far-field radiation pattern of the dual-band patch-antenna prototype (DUT) with different feed-cable set-ups were performed with a spherical scanning system in an anechoic chamber with length of 10 m, width of 7 m, and height of 7 m [22] at Nokia Research Center (NRC), Helsinki, Finland. The measurement and analysis of the 3-D patterns and of the H-field scans were performed in cooperation with J. Krogerus from NRC. The spherical scanning system used is based on a rotating elevation arm, which provides the movement of a probe horn antenna along a semicircular trajectory. The DUT has to be rotated only in the azimuth direction on a turntable. A rotary joint was used so the RF feed cable was geometrically stationary. The samples of the fields radiated by the DUT were taken in steps of $\Delta\phi = 10°$ in azimuth and in steps of $\Delta\theta = 3°$ in elevation. The radius of the scanning sphere, i.e., the distance between the DUT and the probe horn is 2 m. For the DUT in question this distance resembles far-field conditions with sufficiently low uncertainty. The positioner and its support structures are installed on the sidewalls of the chamber (Fig. 62). An HP 8753D network analyser was used to measure the complex transmission coefficient S_{21} between the DUT and the probe. The spherical surface around the DUT was scanned with the probe horn in θ-polarization and then in ϕ-polarization. The DUT was fixed in vertical polarization on an antenna mast installed on the azimuth turntable. The antenna mast is made of two concentric expanded-polystyrene (EPS) columns. To allow mounting of different antenna fixtures and human body models on the antenna mast a 10-mm thick plexiglass plate is glued on top of the larger EPS column 880 mm below the rotation centre of DUT.

The diameter of the larger EPS column and the plate is 600 mm, and the diameter of the narrower EPS column is 200 mm. Along the centre axis of the EPS columns a hole with diameter of 100 mm and 30 mm, respectively, allows convenient placement of the feed cable. The set-up is shown in Figs. 62, 63 and 64. During measurements the centre of the ground plane of the DUT coincided with the centre of the scanning sphere.

In the analysis of the 3-D pattern measurement data, maximum gain, cross-polarization discrimination (*XPD*), directivity, the total radiated power and thus the efficiency of the antenna were determined (see (5) – (7)). Due to mechanical restrictions of the antenna positioning system a conical sector of 30° pointing towards the negative z-axis ("the south pole") of the spherical coordinate system could not be scanned by the probe antenna. The missing data points were filled with the average field strength of all other measured data points. To calibrate the absolute gain levels, the 3-D pattern of a Broad-Band-Horn-Antenna (BBHA) by "Schwarzbeck Mess–Elektronik", Schönau, Germany was also measured. This type of antenna was also used as the measurement antenna (probe horn in Fig. 62).

The maximum gain is defined as

$$G_{\max} = \max\left\{G_\theta + G_\phi\right\}, \tag{5}$$

The total radiation efficiency, which includes also mismatch loss, is defined as

$$\eta_{\text{tot}} = \frac{1}{4\pi}\int_0^{2\pi}\int_0^{\pi}\left[G_\theta(\theta,\phi) + G_\phi(\theta,\phi)\right]\sin\theta d\theta d\phi \,. \tag{6}$$

It should be noted that the gain components G_θ and G_ϕ are not compensated for the mismatch. The cross-polarization discrimination of the AUT is here defined as the ratio of the total radiated power at θ-polarisation and the total radiated power at ϕ-polarization:

$$XPD = \frac{\int_0^{2\pi}\int_0^{\pi} G_\theta(\theta,\phi)\sin\theta d\theta d\phi}{\int_0^{2\pi}\int_0^{\pi} G_\phi(\theta,\phi)\sin\theta d\theta d\phi}\,. \tag{7}$$

The radiation pattern measurements were performed between 880 MHz – 960 MHz and between 1715 MHz – 1875 MHz, i.e. in the two frequency bands of the European GSM standard.

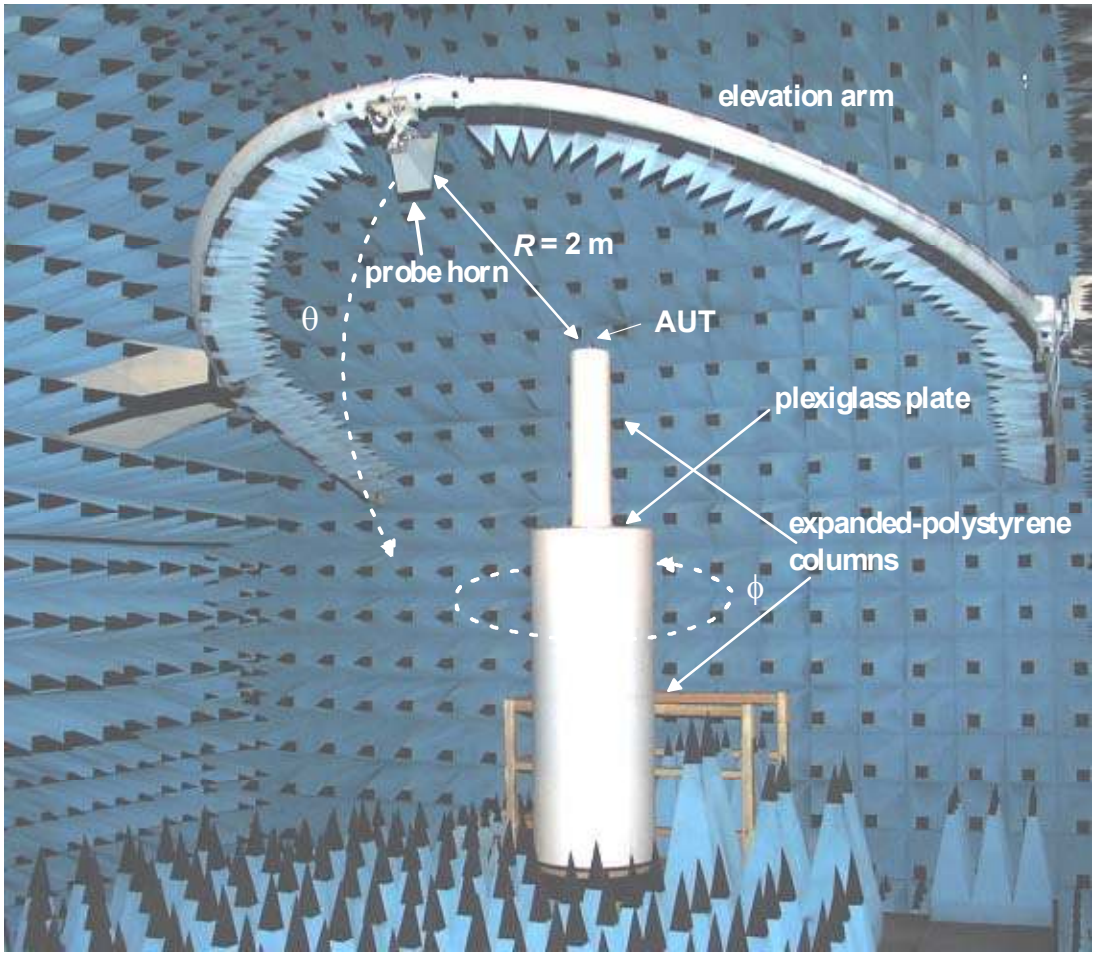

Fig. 62. The 3-D spherical scanning system used in the radiation pattern measurements.

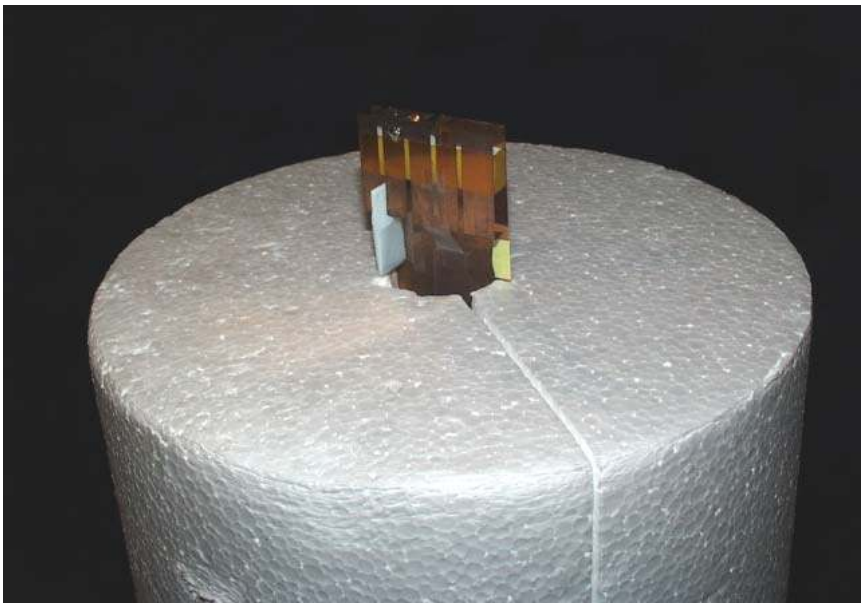

Fig. 63. The AUT was fixated in vertical polarisation on the expanded styrofoam pole during the radiation pattern measurements.

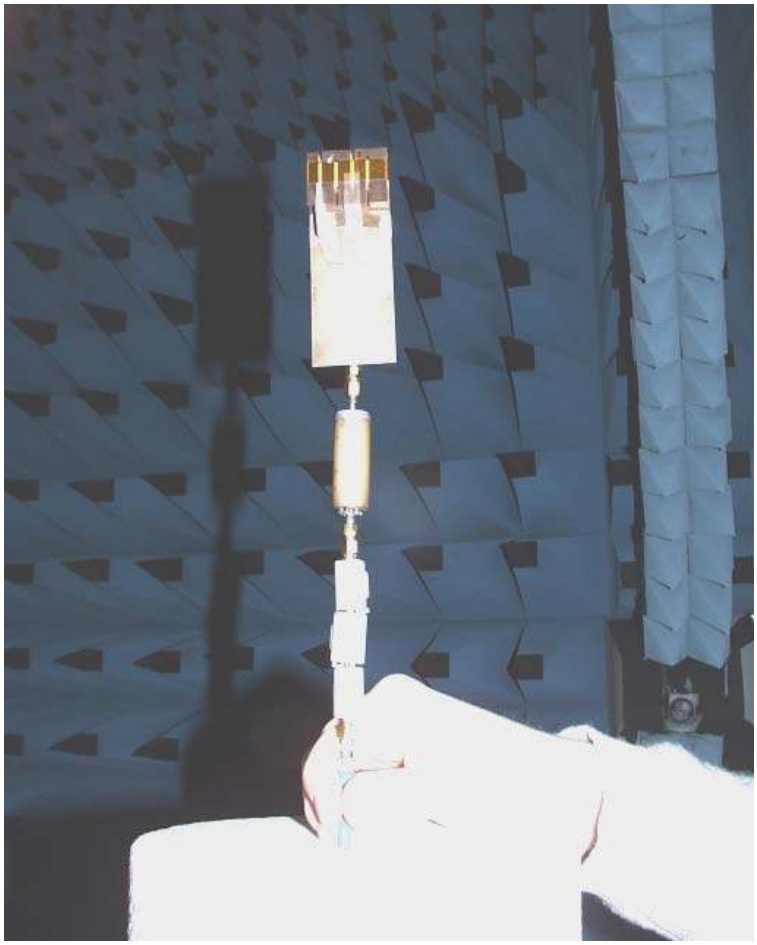

Fig. 64. The AUT (top) with the dual-band balun and three ferrite beads (bottom).

5.4.3. H-field scanning

Estimations of the surface current distributions on the AUT and the different feed-RF-cable configurations were performed at NRC with a computer-controlled magnetic field probe mounted on a scanner with a robot arm. The DASY3 system (Dosimetric Assessment System) by Schmid and Partner AG was used for this purpose. This SAR measurement system can also be used for surface-current distribution measurements for antenna design purposes. In these measurements a free-space magnetic-field probe is used, which measured three orthogonal magnetic-field components simultaneously with three concentric loop antennas. The probe scanned a plane at 15 mm over the ground plane. This means that the distances to the balun and the patch were 9 mm and 8 mm, respectively. The sample step width both in the x- and y-directions was 10 mm. The H-field scan in a plane very near to the DUT gives an estimate of the current distribution on the surface of the DUT, since current density is proportional to the magnetic field. The measurement frequencies were 920 MHz and 1795 MHz. A 450-mm high pyramidal RF absorber was placed around the feed RF cable near the signal source to reduce possible standing waves on the outer surface of the cable. The measurements took place in a semi-anechoic chamber (see set-up in Figs. 65 and 66).

5.4.4. Investigated configurations

The four different configurations in the 3-D pattern measurements and in the magnetic-field scans were:

M1) AUT with the RF feed cable only
M2) AUT with cable and three ferrite beads inserted
M3) AUT with cable and dual-band balun inserted
M4) AUT, cable with dual-band balun and an additional set of ferrite beads. In the 3-D pattern measurement the set-up included two additional ferrite beads placed on the RF feed cable. The distances of the first and second extra ferrite from the lower end of the group of three ferrites (see Figure 66) was 13 cm and 26 cm, respectively.

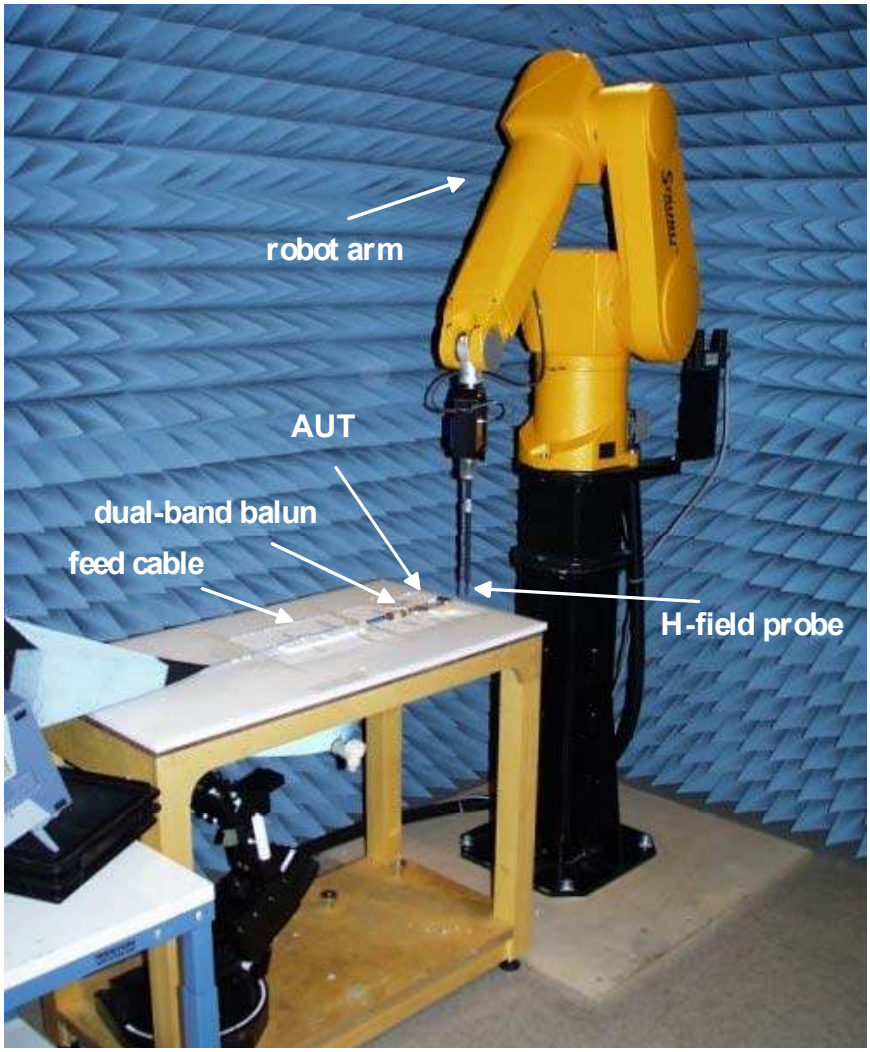

Fig. 65. The H-field scanning set-up (M3) used for evaluating the current distribution.

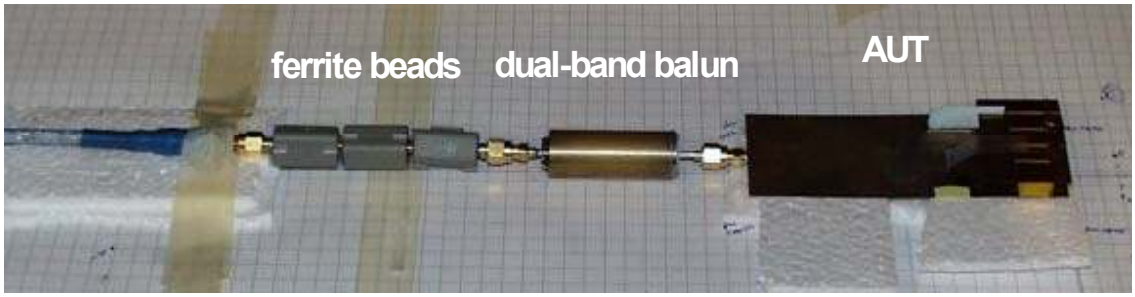

Fig. 66. Close-up of the H-field scanning set-up in the configuration in which the AUT was with the dual-band balun and three ferrite beads.

5.5. Measurements results

5.5.1. 3-D field pattern measurement results

Tables 7 and 8 show the antenna parameters calculated from the 3-D patterns at 920 MHz and at 1795 MHz. Tables 9 and 10 show the same parameters as averaged over the GSM900 and GSM1800 bands. Figs. 67 and 68 show the total radiation efficiency (6) and the maximum gain (5) as a function of frequency for the four set-ups. Figs. 69 – 75 show measured radiation patterns at 920 MHz and at 1795 MHz, respectively.

Table 7. Comparison of several antenna parameters calculated from 3-D patterns measured/simulated at 920 MHz with different set-ups

	Set-up	η_{tot}[dB]	η_{tot}[%]	G_{max}[dBi]	D_{max}[dBi]	XPD[dB]
Measured	M1: AUT with RF feed cable	-3.6	44%	6	9.5	6.3
	M2: AUT, cable and 3 ferrites	-2.5	56%	0.6	3.1	9.6
	M3: AUT, cable and balun	-0.3	93%	2.3	2.6	12.6
	M4: AUT, cable, balun+ferrites	-0.3	93%	2.4	2.7	12.5
Simulated	S1:Isolated AUT	-0.2	96%	2.2	2.4	–

Table 8. Comparison of several antenna parameters calculated from 3-D patterns measured/simulated at 1795 MHz with different set-ups

	Set-up	η_{tot}[dB]	η_{tot}[%]	G_{max}[dBi]	D_{max}[dBi]	XPD[dB]
Measured	M1: AUT with RF feed cable	-1.6	69%	4.2	5.8	1.4
	M2: AUT, cable and 3 ferrites	-1.6	69%	3.2	4.8	1.6
	M3, AUT, cable and balun	-1.3	75%	3.3	4.6	1.0
	M4: AUT, cable, balun+ferrites	-1.2	76%	3.3	4.4	1.0
Simulated	S1:Isolated AUT	-0.6	88%	3.7	4.2	–

Table 9. Comparison of antenna parameters calculated from 3-D pattern between different set-ups. Average values over GSM900 band.

	Set-up	η_{tot} [dB]	η_{tot} [%]	G_{max} [dBi]	D_{max} [dBi]	XPD [dB]
Measured	M1: AUT and RF feed cable	-3.9	41%	5.7	9.6	6.9
	M2: AUT, cable and 3 ferrites	-2.9	51%	0.1	3.0	9.6
	M3: AUT w. cable and balun	-0.8	83%	1.8	2.6	12.1
	M4:AUT, cable, balun+ferrites	-0.8	84%	1.9	2.7	12.1
Simulated	S1:Isolated AUT	-0.4	91%	1.7	2.1	–

Table 10. Comparison of antenna parameters calculated from 3-D pattern between different set-ups. Average values over GSM1800 band.

	Set-up	η_{tot} [dB]	η_{tot} [%]	G_{max} [dBi]	D_{max} [dBi]	XPD [dB]
Measured	M1: AUT and RF feed cable	-1.6	70%	4.2	5.8	1.4
	M2: AUT, cable and 3 ferrites	-1.5	70%	3.2	4.8	1.7
	M3: AUT w. cable and balun	-1.2	76%	3.4	4.6	1.2
	M4: AUT, cable, balun+ferrites	-1.2	77%	3.4	4.6	1.3
Simulated	S1:Isolated AUT	-0.7	85%	3.5	4.2	–

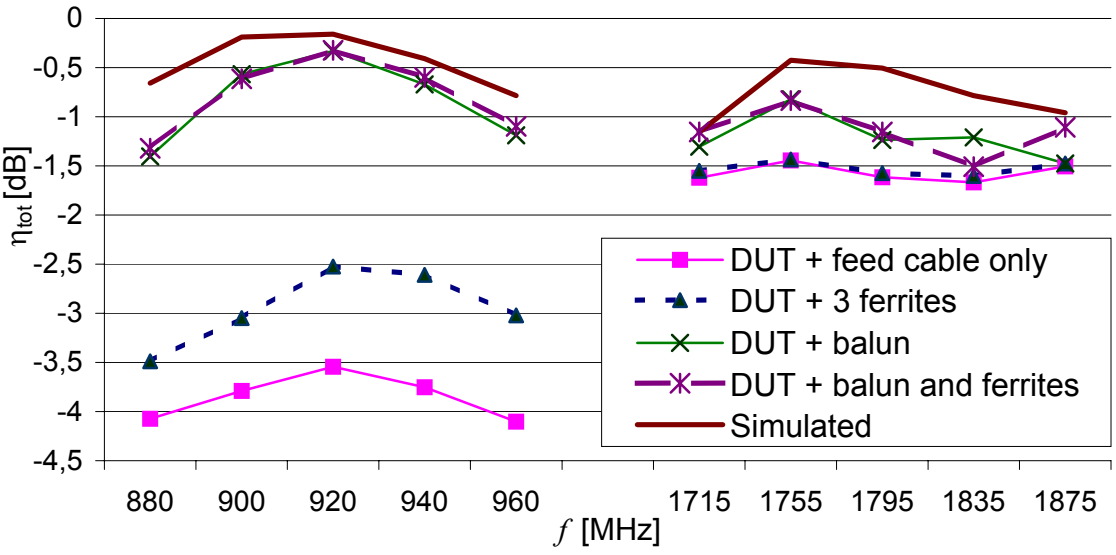

Figure 67. Measured total radiation efficiency with the four different set-ups, compared to the simulated radiation efficiency.

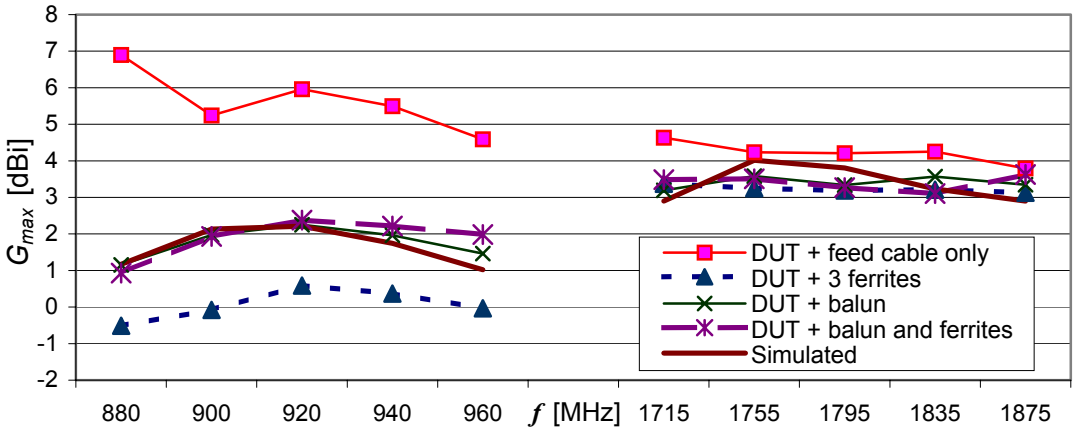

Figure 68. Measured maximum gain with the four different set-ups and simulation.

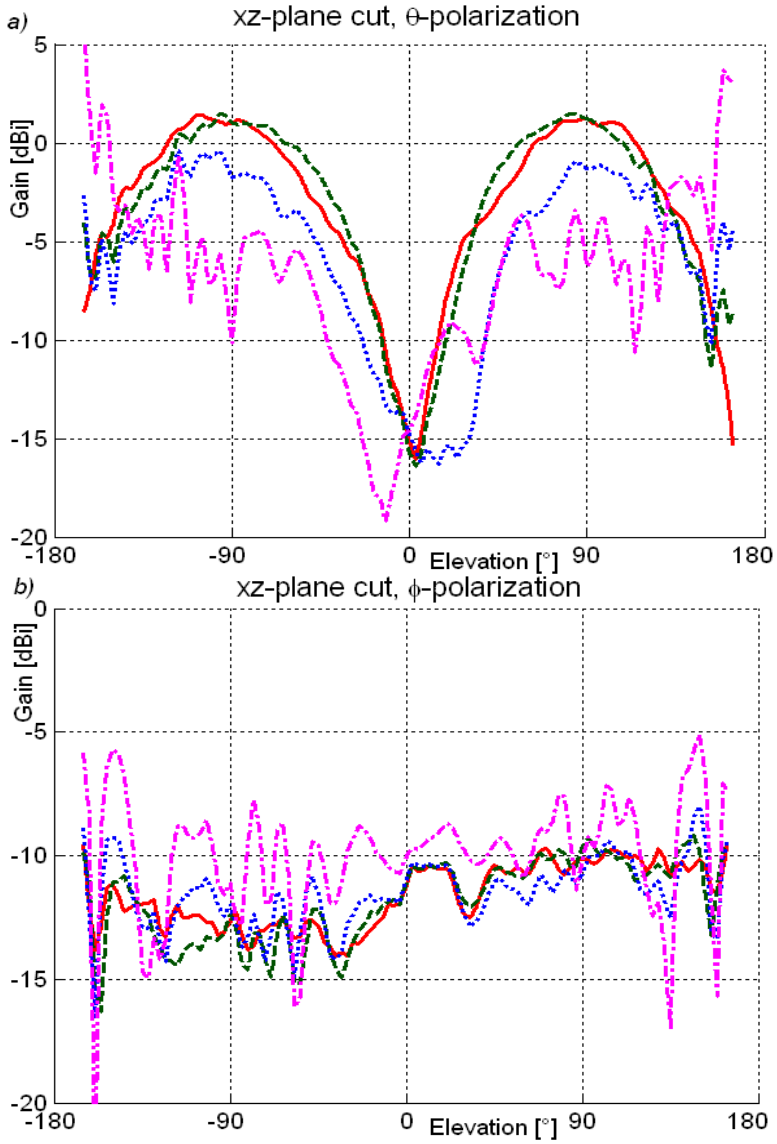

Figure 69. Comparison of *xz*-plane gain pattern cuts with four measured set-ups. f = 920 MHz. M1: AUT + feed cable · – · –, M2: AUT + 3 ferrites · · ·, M3: AUT + balun – –, M4: AUT + balun and ferrites —.

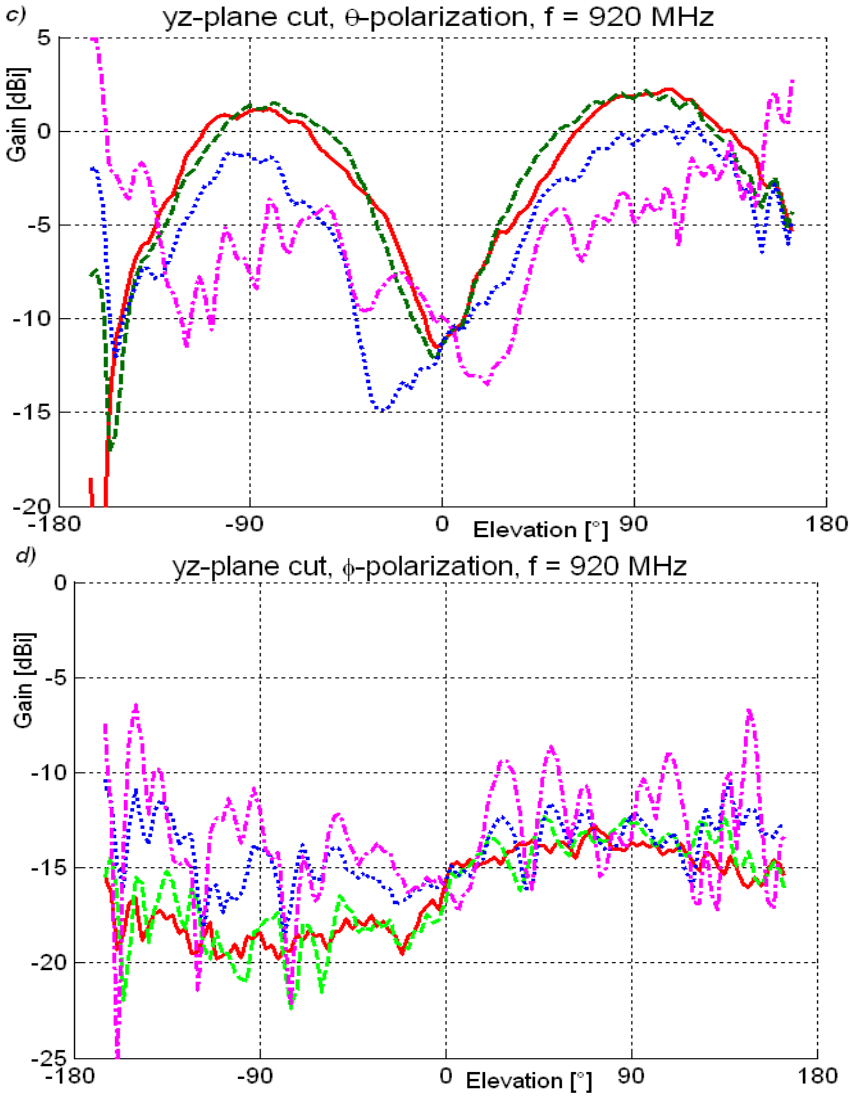

Figure 70. Comparison of yz-plane gain pattern cuts with four measured set-ups. *f* = 920 MHz. M1: · – · –, M2: · · ·, M3: – –, M4 —.

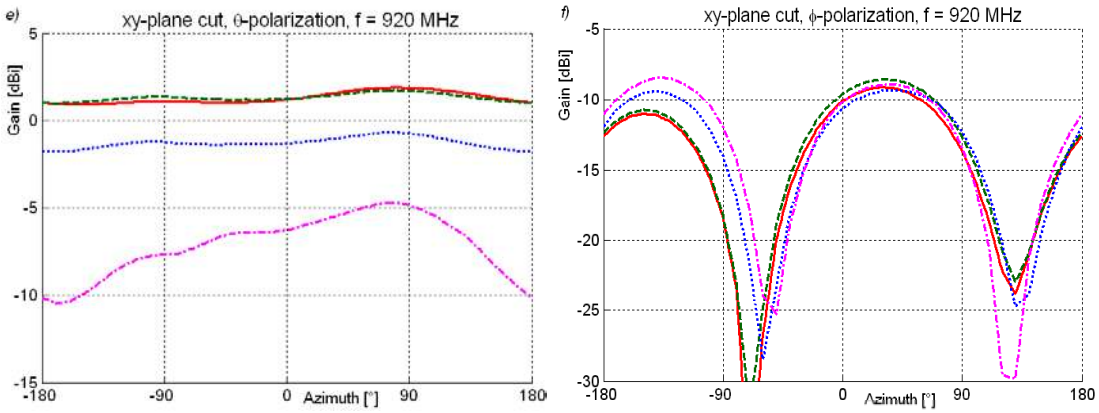

Figure 71. Comparison of *xy*-plane gain pattern cuts with four measured set-ups. *f* = 920 MHz. M1: · – · –, M2: · · ·, M3: – –, M4: —.

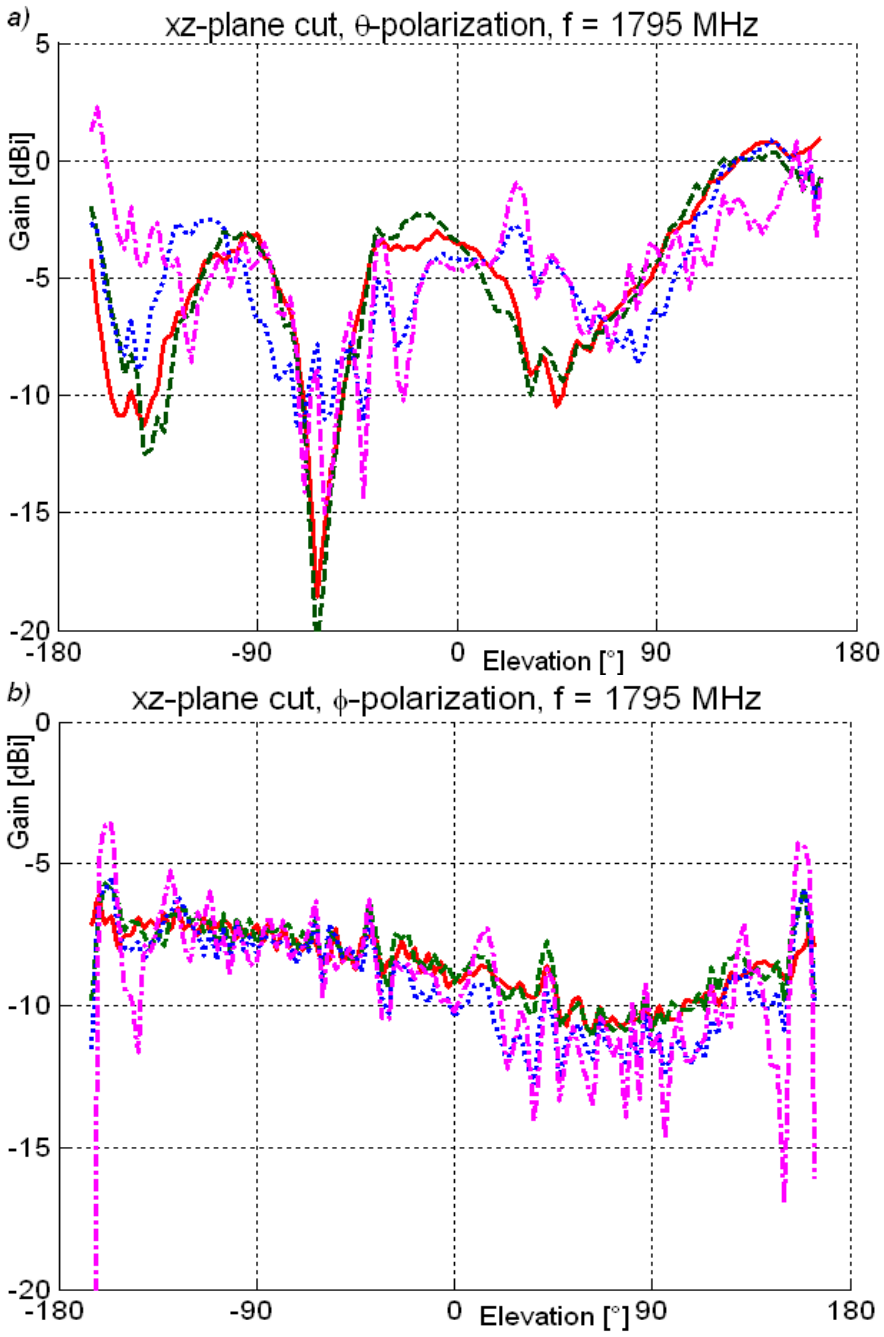

Figure 72. Comparison of *xz*-plane gain pattern cuts with four measured set-ups. *f* = 1795 MHz. M1: AUT + feed cable · – · – , M2: AUT + 3 ferrites · · ·, M3: AUT + balun – – , M4: AUT + balun and ferrites —.

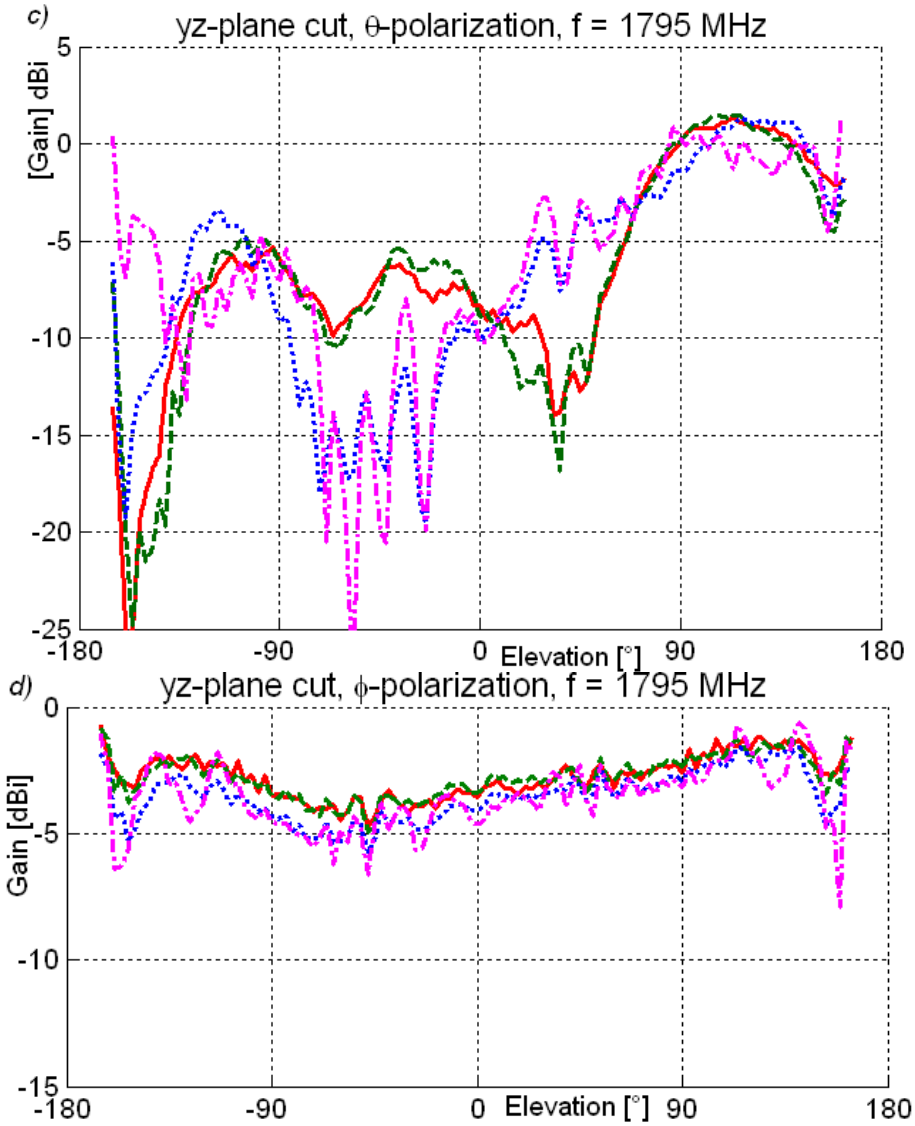

Figure 73. Comparison of *yz*-plane gain pattern cuts with four measured set-ups. *f* = 1795 MHz. M1: · – · –, M2: · · ·, M3: – –, M4: —.

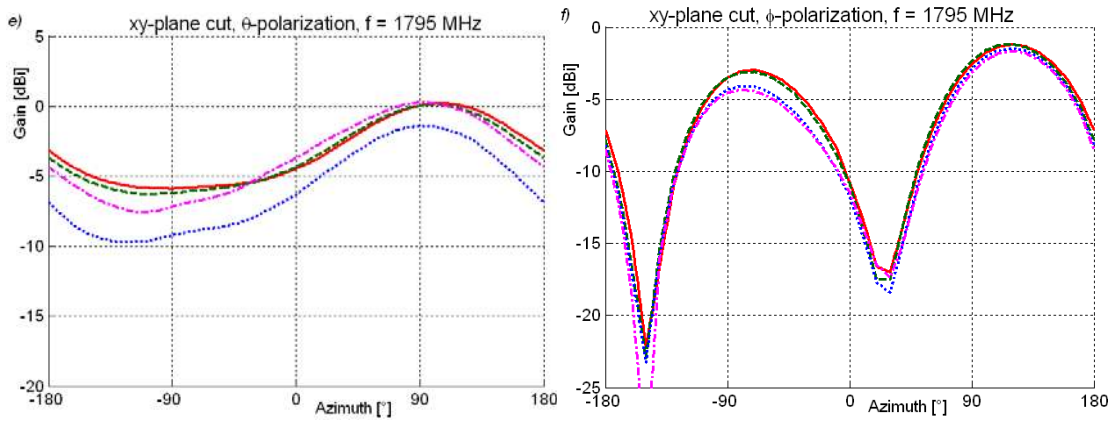

Figure 74. Comparison of *xy*-plane gain pattern cuts with four measured set-ups. *f* = 1795 MHz. M1: · – · –, M2: · · ·, M3: – –, M4: —.

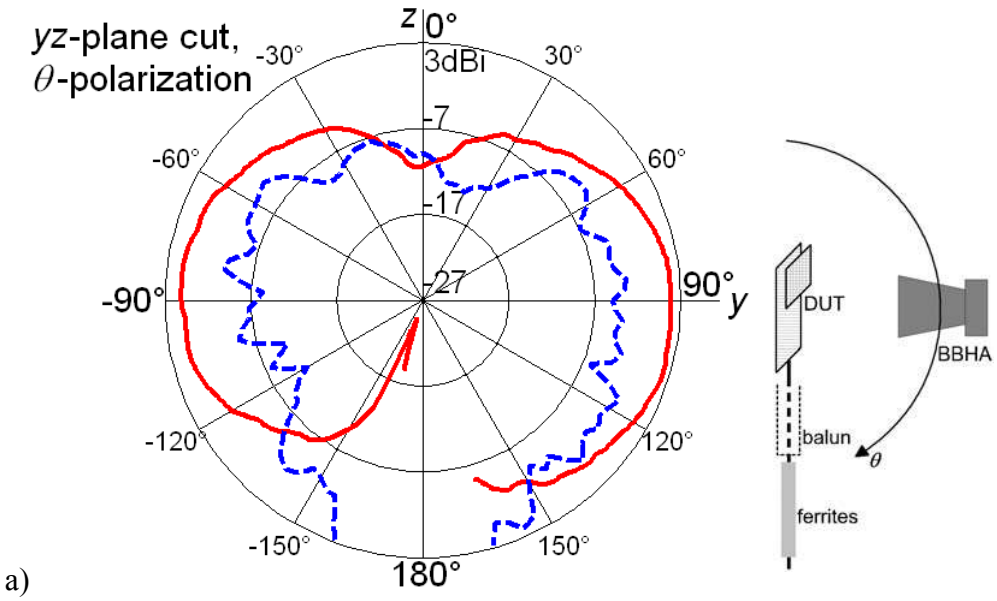

a)

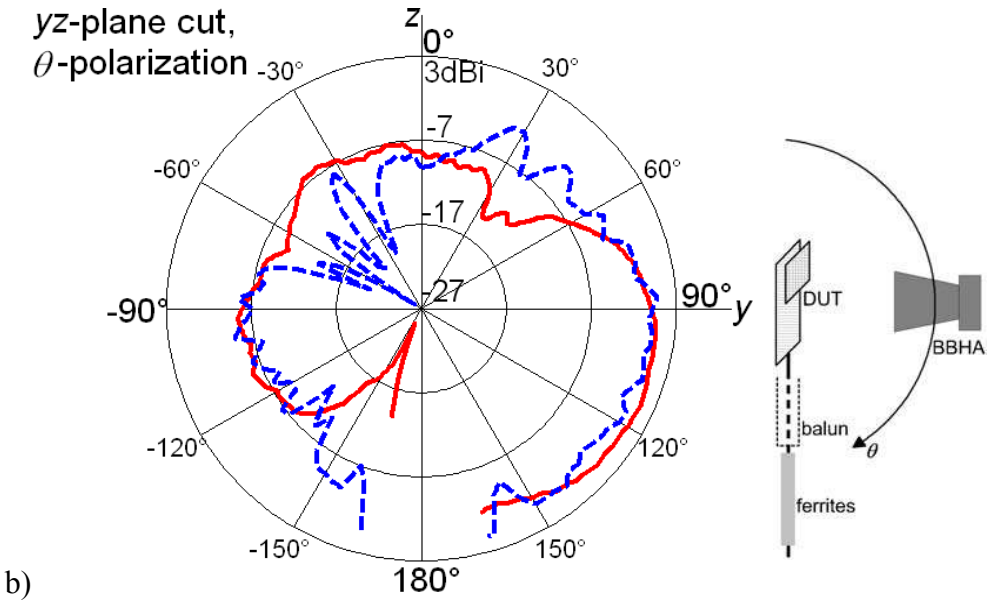

b)

Figure 75. Comparison of the *yz*-plane gain patterns for the worst set-up (M1, AUT + feed cable only) - - - - and the best set-up (M4, AUT + balun + ferrites) ——. The figure next to the plot visualizes how the AUT was oriented, a) f = 920 MHz, b) f = 1795 MHz.

From Table 7 and Figs. 69 – 71 we can see the large effect of the feed cable at 920 MHz, where the rather high gain in Case M1 cannot be obtained with such a small radiator as the DUT but can only be attributed to the cable acting as an additional (distributed) radiator which introduces an interference pattern with stronger main- and sidelobes. The large and fast ripples of up to ±3 dB in the radiation pattern cuts in Fig. 69 – 71 and Fig. 75 a) show the interference effects of the RF cable. Part of the total radiated power originates from the cable, and most of this power is not detected as the cable acts as a travelling wave antenna with a strongly downward directed

pattern [53, p. 494], i.e. mostly outside the scanning area of the probe, which explains the low efficiency of Case M1. This is also the reason why quite high radiation levels occur in the direction of the cable ($|\theta| > 160°$), where we would expect a pattern null for the isolated DUT, because at 920 MHz the dipole-like ground plane can be assumed to be main source of radiation from the DUT [23], [24]. At 920 MHz the significant decrease in cross-polarized radiated power when the balun is used (see Table 9 and Figs. 69 – 70) indicates that the feed-cable without any balun decreases the vertically polarised component of the effective dipole that the ground plane forms. This can also be seen in Fig. 76 where the dark-red high-current area increases in length when the balun is used.

Due to the ferrite chokes placed on the feed cable in Case M2 the radiation-pattern ripples are decreased, but the ferrite chokes also reduce the gain and the efficiency due to their losses (Figs. 67 – 68). With only the balun on the other hand, the gain, efficiency and total radiated power agree well with the simulated reference values, and also yield a smooth dipole-typical pattern. This is further improved by additional ferrites placed on the cable beyond the balun. The curvature of the efficiency and the gain as a function of frequency in the GSM900 band in Figs. 67 and 68 is caused by the decrease in matching towards the band edges of the handset antenna.

At 1795 MHz the effect of the attached RF cable on the radiation characteristics in Table 8 is less severe than at 920 MHz, although still notable from the pattern cuts in Figs. 72 – 74 and Fig. 75b). The improvement by the ferrites is smaller than at 920 MHz because above 1 GHz the permeability of ferrites typically decreases as a function of frequency while and dielectric loss tangent increases [67]. Again the balun decreases the main-lobe ripples on the pattern cuts considerably from ±5 to about ±1 dB, which is in good agreement with the simulated results that were presented in Section 5.3.

Some non-idealities can still be observed in the patterns measured in Case M4 (balun + ferrites) and the main reason for them is the remaining re-radiation of the feed cable. Using more ferrites and placing them more densely along the feed cable and can decrease the re-radiation effect even further. Additionally, the antenna mast may also have some effect. Although the influence of the EPS column to the pattern shapes can be expected to be very low, the plexiglass plate (measured $\varepsilon_r' \approx 2.8$ at the frequency bands used) probably has some scattering effect. With the dimensions of the plexiglass plate and EPS column the plate is situated in the line-of-sight (LOS) between the AUT and the probe when the elevation angle is $\theta > 160°$. Finally, despite of the use of large absorbers in this anechoic chamber [22] residual reflections in the chamber may also affect the pattern.

5.5.2. H-field measurement results

Figs. 76 and 77 illustrate the measured magnitude of the total *H*-field [dBmA/m] on a parallel plane 15 mm above the ground plane at 920 MHz and at 1795 MHz, respectively.

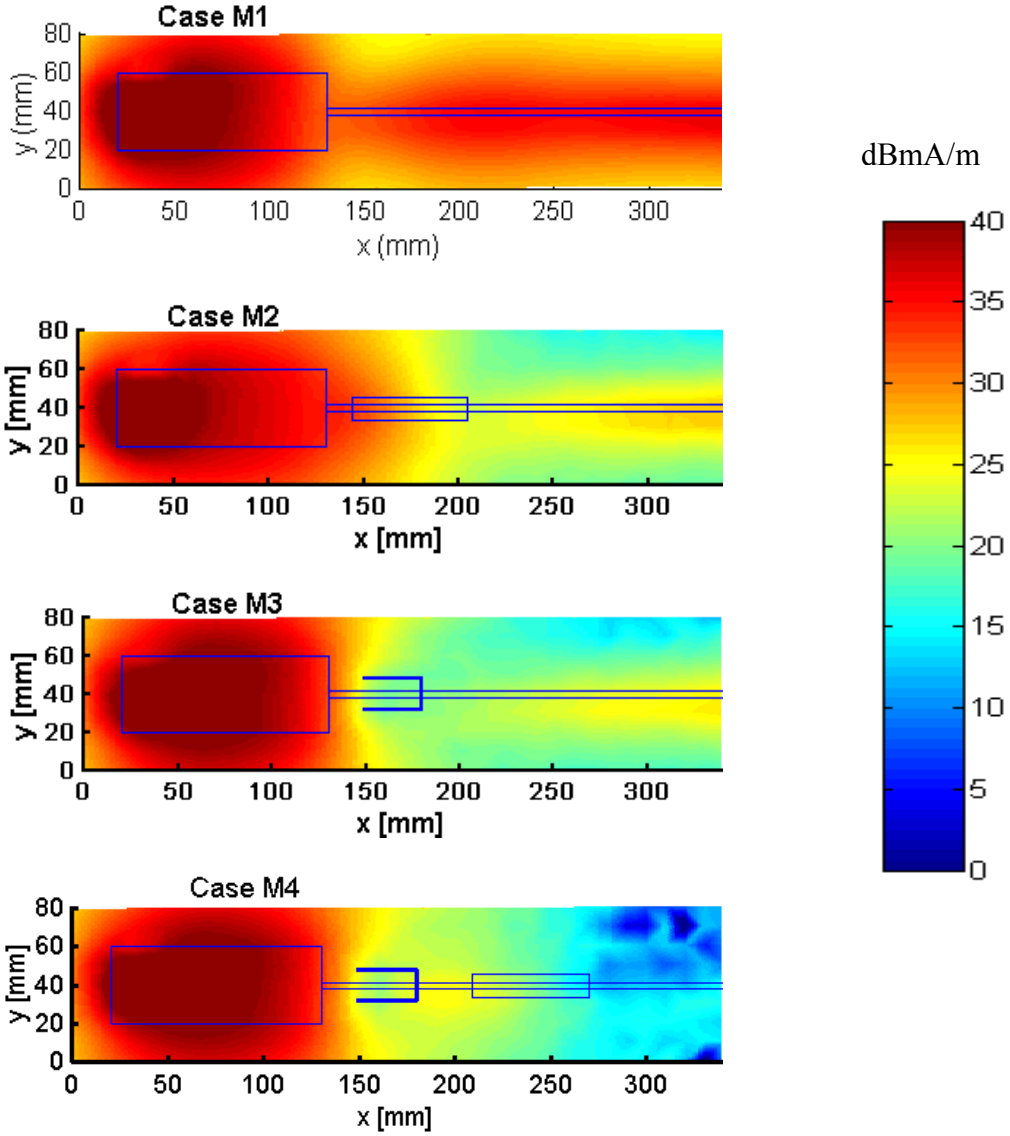

Figure 76: Measured magnitude of total H-field [dBmA/m] 15 mm above the ground plane at f = 920 MHz, The ground plane (40 mm × 110 mm), the RF cable, and the location of the 3 ferrites (total length = 70 mm, ∅ = 14 mm) are adumbrated by thin lines, the balun (length = 44 mm, ∅ = 16 mm) by a thick line.

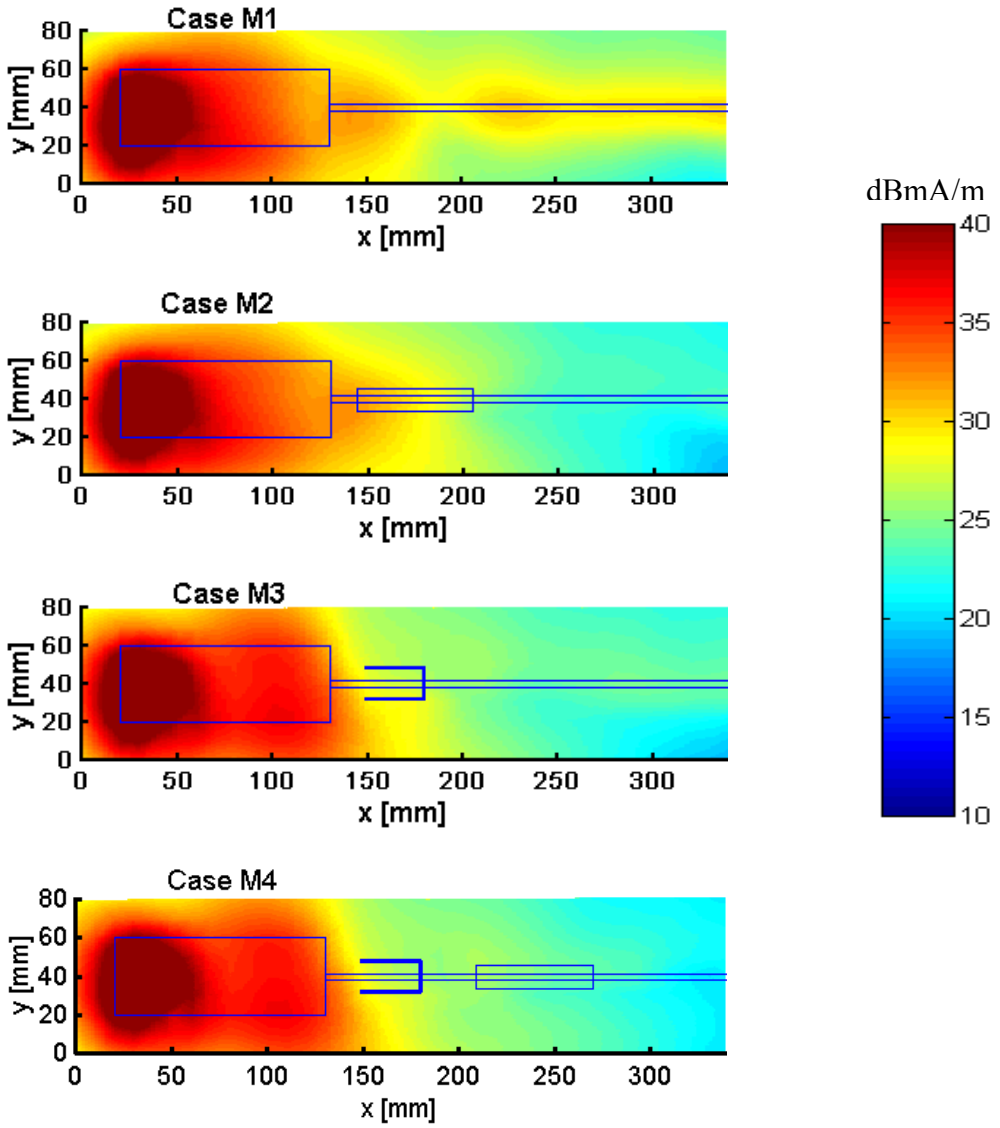

Figure 77: Measured magnitude of total H-field [dBmA/m] 15 mm above the ground plane at f = 1795 MHz, The ground plane (40 mm × 110 mm), the RF cable, and the location of the 3 ferrites (total length = 70 mm, ∅ = 14 mm) are adumbrated by thin lines, the balun (length = 44 mm, ∅ = 16 mm) by a thick line.

Fig. 76 and 77 illustrate the current density on the handset at 920 and at 1795 MHz. Fig. 78 shows the *H* field (and thus indicates the current density) along the attached RF feed cable at 920 MHz and 1795 MHz. The same four cases are compared as those in the far-field measurements, i.e. M1 - M4. It can be noticed that fringing H-fields at the edges extend beyond the edges of the ground plane.

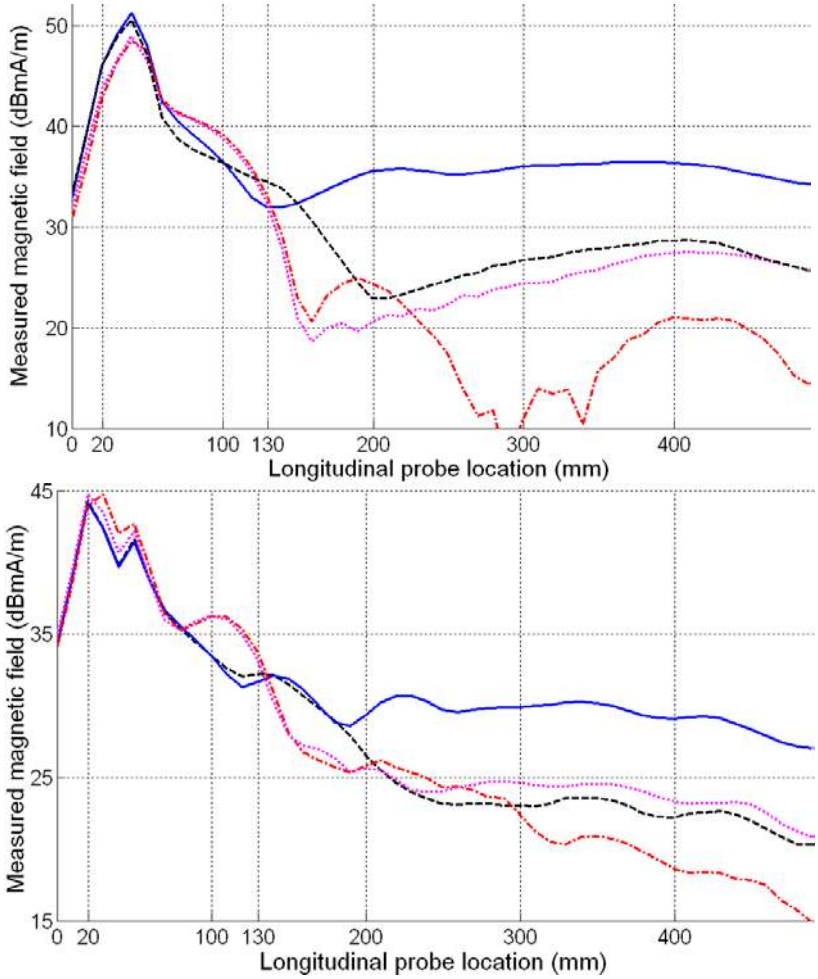

Figure 78: The measured magnitude of the total *H*-field strength along the RF cable, 15 mm above ground plane (extends from 20 mm to 130 mm) and RF cable, at 920 MHz (top) and 1795 MHz (bottom). Cable only — (a) , with ferrites - - - (b) , with balun — (c) , bal&ferr. - • - (d).

Very clearly, in M3 and M4 the surface currents are well restrained to the ground plane of the handset and do not propagate onto the RF cable like they do in M1 and even M2, while in M2 the currents show a maximum just in front of the ferrite bead, but also some activity behind the ferrite. The second current maximum in the lower part of the ground plane is lost when only the cable is attached, but can clearly be noted in case of the balun. The ability to block currents, or the isolation of the balun, can be seen (Fig, 78) to be much better than 10 dB at 920 MHz and about 6-7 dB at 1795 MHz. Placing several ferrites close to the handset along the RF cable will decrease the total radiated power as shown in Section 5.5.1. However, as was mentioned above, the use of ferrites along the RF cable but beyond the balun(s) is useful and recommendable in order to decrease the scattering effects of the cable exposed to the far fields originating from the AUT. This can be seen also in Fig. 78, where the case with a balun and ferrites yields the lowest H-fields at the far end of the RF cable, decreased by more than 15 dB compared to the case with only the RF cable attached to the handset.

5.5.3. Bandwidth of the balun

Measurements of the filter characteristics were performed to evaluate the performance of the dual-band balun prototype shown in Fig. 59. The effective bandwidth is difficult to determine, as it is mainly radiation effects that we are measuring. However, with help of computer simulations and with measurements inside a waveguide the effective bandwidth of the balun can be estimated. The filter characteristics of the balun on an RF cable were measured inside a rectangular waveguide below cut-off, i.e. with a cross-section of 52 mm × 72 mm (see Fig. 79). The balun prototype was placed between two standard flexible RF cables. Outside the waveguide the RF cables were covered with RF absorber cones to inhibit standing waves on the RF cable shield. When the RF cables are placed along the centre line of the waveguide the cables form the centre conductor of a rectangular coaxial waveguide. Two capacitive field probes were inserted in the walls of the waveguide to couple into the TEM mode. Their distance along the axis of the waveguide was 200 mm, and the 41 mm long balun was situated between the probes. The transmission coefficient between the probes with the balun contrasted with only an RF cable inside the waveguide gives a clear picture of the centre frequencies and an indication of the bandwidth of the balun.

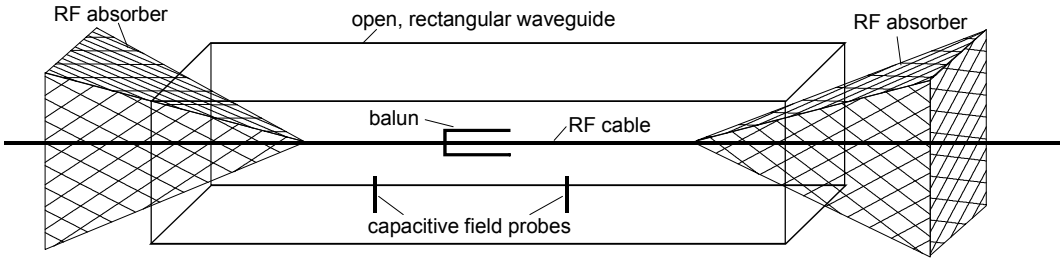

Fig. 79: Principle measurement set-up for determining the filter characteristics of the balun inside a waveguide below cut-off.

As seen from the measured S_{21} in Fig. 81, the lower centre frequency is about 920 MHz and the upper one about 1840 MHz. From Fig. 81 one can furthermore estimate the bandwidth of this filter. For an isolation of at least 10 dB the bandwidth is about 10 % at both frequency bands. Computer simulations (Fig. 80) in free space gave comparable results for the resonance frequencies and bandwidths. The slightly different resonant frequencies in the simulations and in the measurements are caused mainly by the fact that the measured prototype was tuned to an optimum with the tuning screws which were impossible to include in the simulations. Additionally, the resonance frequencies of the balun inside the rather narrow waveguide can differ from the free-space set-up. The simulations show an additional return loss of 3 dB already at the transition from the handset to the RF cable. Unfortunately, the impedance step has an effect on the resonance frequencies of the balun, when compared to the balun placed on an infinitely long cable. Simulations have shown that both effects, i.e. measuring the balun inside a waveguide and placing the balun near the handset-cable impedance step, cause an uncertainty in both upper and lower centre frequency of about 2 – 3%. To decrease the error simulations were used to predict this shift and tune the balun inside the waveguide accordingly.

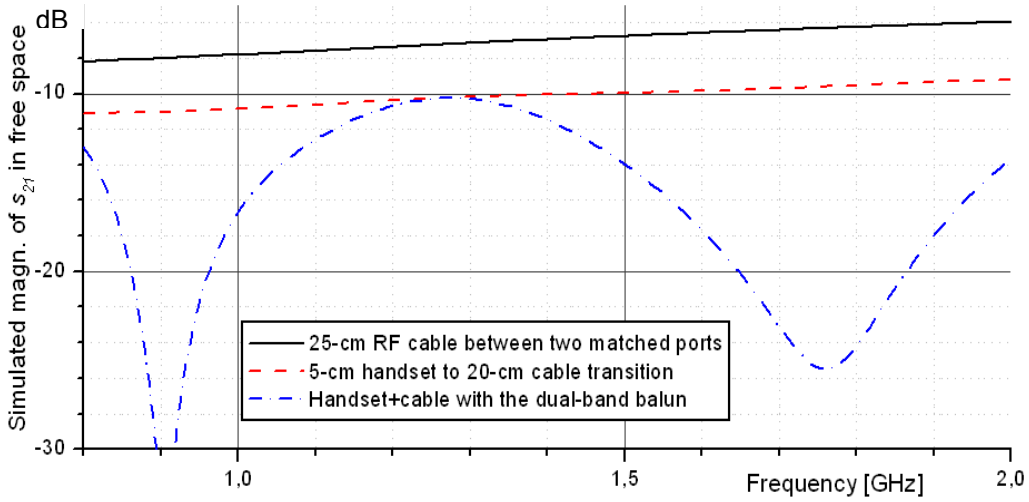

Fig. 80: Simulated $|S_{21}|$ between two matched simulation ports 25 cm apart in free space, with (dash-dot) and without (dashed) balun on RF cable.

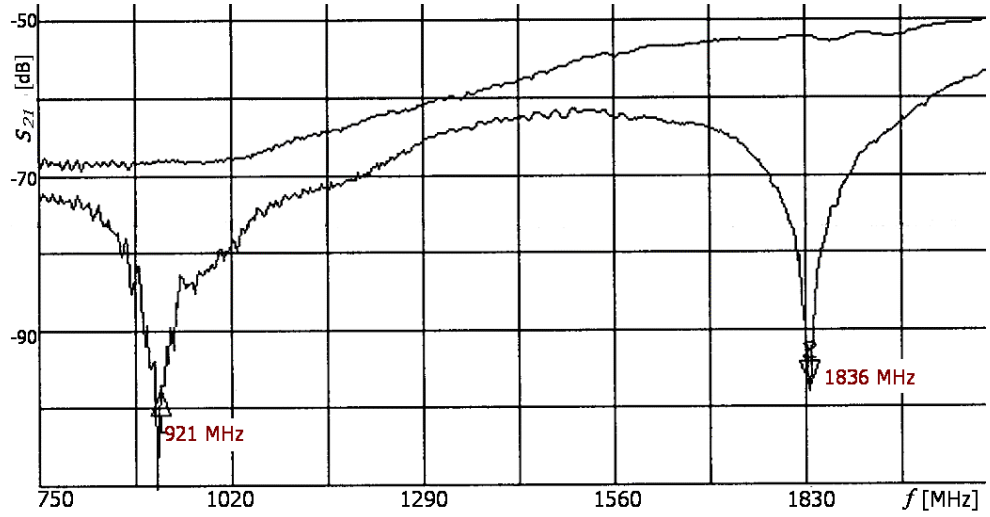

Fig. 81: Measured $|S_{21}|$ between two capacitive field probes on the wall of the waveguide, with balun (lower) and without (upper) balun on centred RF cable inside a 52 mm × 72 mm rectangular waveguide (Fig. 79). The two resonance frequencies are 921 MHz and 1836 MHz.

It should be noted, that the tuning screws always change both resonance frequencies and cannot correct inaccuracies in the construction affecting the ratio of the resonance frequencies. However, additional tuning screws that decrease the volume/length of the outer cavity in the balun could be considered.

Figs. 82 – 85 illustrate the performance of the combination of the balun and the ferrites (Case M4) as a function of frequency. Both *xz*-plane the *yz*-plane pattern cuts are shown, which appear to be the ones most affected by the interferences originating from the vertically hanging cable. For comparison also set-up M1 is shown in which the AUT was measured with only the feed cable. It can be seen that the balun can retain sufficiently well the general dipole-like pattern shape of the AUT over the approximately 10 % relative bandwidth investigated (920 MHz ± 4.3 %) at the GSM900 band (Fig. 82). In other words, the amount of cable-originating ripples does not increase at the band edges of the balun.

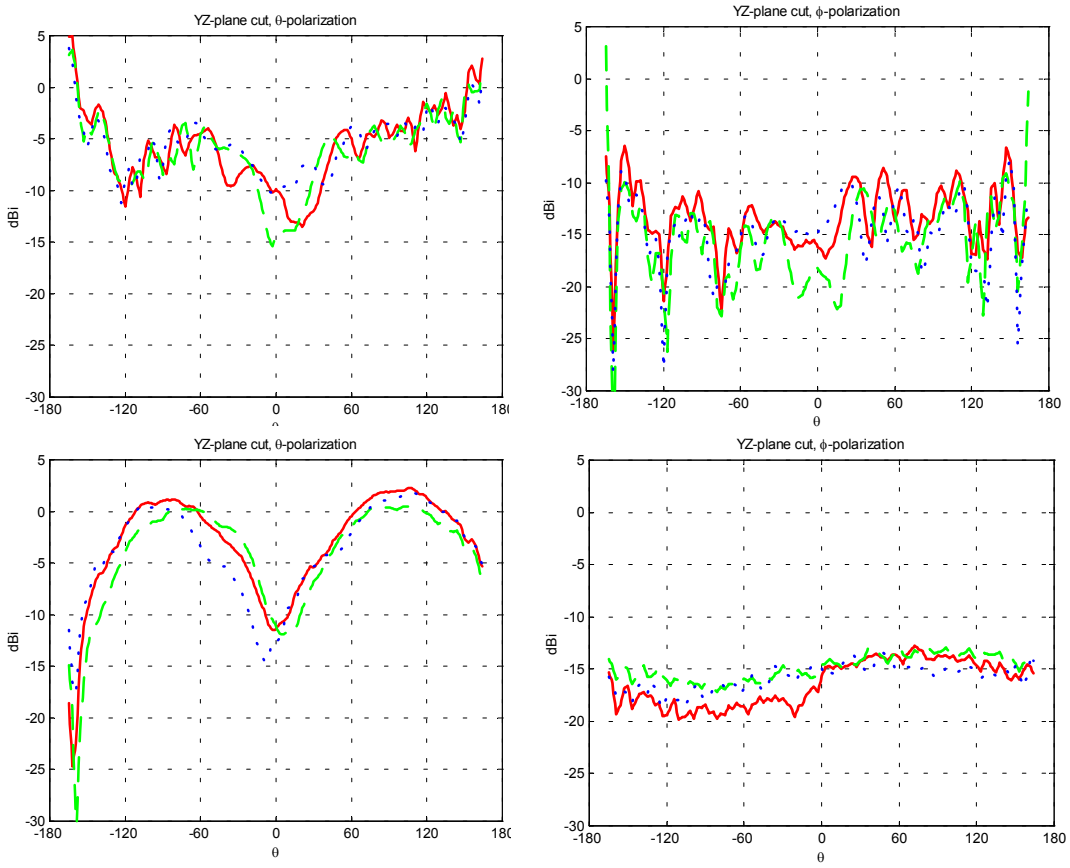

Figure 82. Illustrating the bandwidth of the balun at the GSM900 band. Gain pattern cuts at 880 MHz – – –, 920 MHz ——, 960 MHz - - - -. *Top row:* the worst set-up (M1: AUT + RF feed cable only). *Bottom row:* the best set-up (M4: AUT + balun + ferrites).

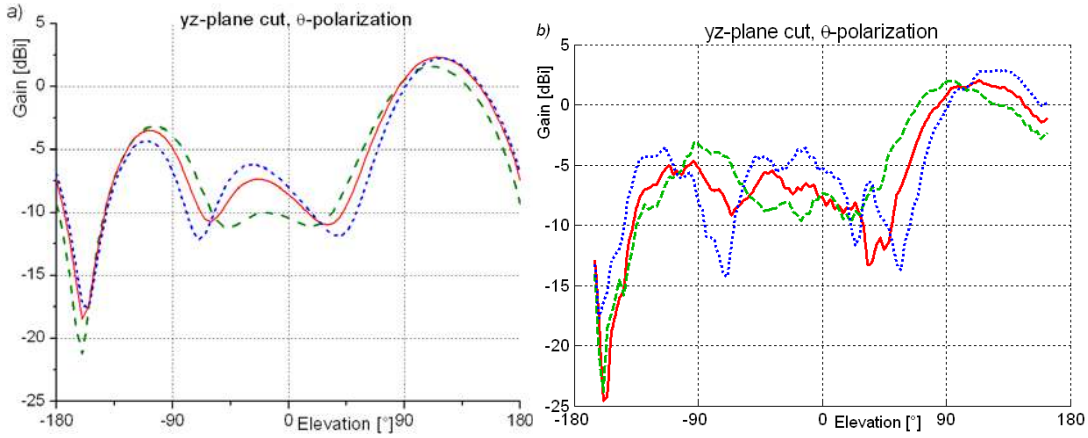

Figure 83. Illustrating the bandwidth of the balun at the GSM1800 band, *yz*-plane gain pattern cuts at 1715 MHz – – –, 1795 MHz ——, 1875 MHz - - - -. a) simulated pattern with DUT alone, b) set-up M4) (DUT + balun + ferrites).

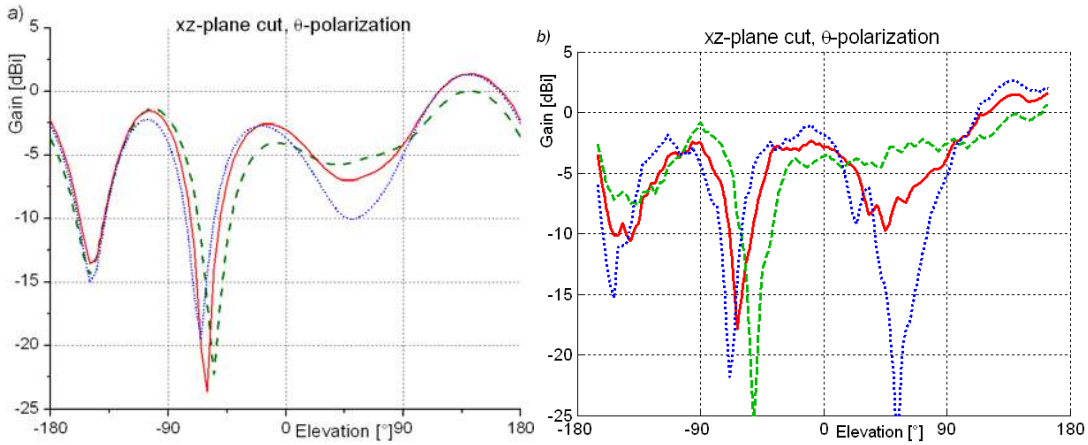

Figure 84. Illustrating the bandwidth of the balun at the GSM1800 band, *xz*-plane gain pattern cuts at 1715 MHz – – –, 1795 MHz ——, 1875 MHz - - - -. a) simulated pattern with DUT alone, b) set-up M4) (DUT + balun + ferrites).

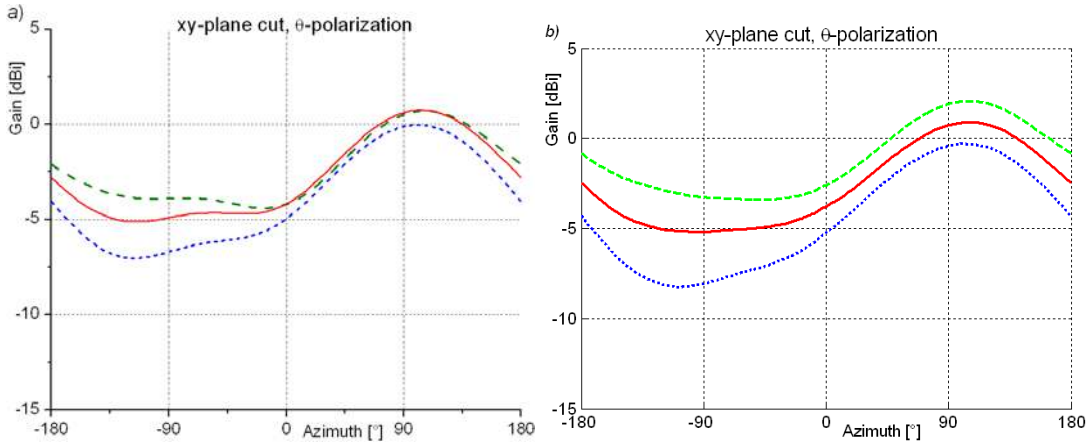

Figure 85. Illustrating the bandwidth of the balun at the GSM1800 band, *xy*-plane, gain pattern cuts at 1715 MHz – – –, 1795 MHz ——, 1875 MHz - - - -. a) simulated pattern with DUT alone, b) set-up M4) (DUT + balun + ferrites).

At GSM1800 band the investigation is more difficult due to more complex pattern shapes and due to the fact that at 1800 MHz the inherent changes in the pattern shapes of the AUT are more rapid as function of frequency than at 900 MHz band. This can be verified in Figs. 83 – 85, which contain the simulated patterns in the GSM1800 band, at 1715 MHz, 1795 MHz, and 1875 MHz (i.e. 1795 MHz ± 4.5 %). The shapes of the three lobes in the *xz*- and the *yz*-plane remain relatively smooth and distinguishable at all frequencies. At an elevation of around $\theta = 60°$ we can see differences in the *yz*-plane pattern, these can also be found in the simulated patterns, where also the shift in the null around $\theta = -60°$ is apparent. However, in the measured patterns both these details get slightly more emphasised. This indicates that the balun virtually increases (for higher frequencies) or decreases (for lower frequencies) the ground plane when the frequency offset from the centre frequency increases. Figs. 35 – 45 in Chapter 4 illustrate the bandwidth of the balun through measurements of three different principal plane cuts in a large anechoic chamber and also in a small anechoic chamber. In comparison to the simulated pattern, over a bandwidth of 10% the measured patterns with the balun (Small chamber and Large

chamber 1) resemble the simulated pattern similarly well as the balun-less measurement in a standard large chamber.

Also the efficiency and the gain measured with the balun are clearly closer to the simulated case as can be seen in Figs. 67 and 68. All the presented measurement results show that over a bandwidth of about 10% at each frequency band the dual-band balun provides an effective means to suppress the RF cable as an error source in measurements of the radiation characteristics of small antennas.

Some limitations in the use of the balun can be stated. There is first of all the relatively slow design process that requires computer simulations and an optimisation process for the dimensions. The result is a balun that works only for a designated (dual-)frequency range, so for instance a set of baluns is needed if several very different frequency ranges are measured frequently. Tuneable frequency ranges are technically possible through mechanically varying the dimensions of the balun with help of screws, for instance the length or diameter of the different cavities. This concept is currently used only to fine-tune the gap distance as described in Section 5.2.2. but could be expanded to a larger tuning range.

Depending on the position of the RF feed cable, also the need to insert a rigid piece of RF cable that contains the balun (with a length of about 100 mm) may be of disadvantage. However, as was discussed in Section 5.1.3 the positioning of the cable can be considered much less crucial when baluns are used. Therefore, mechanical conveniences like alignment of the RF cable with the rotational axis can be taken into account more freely when using baluns.

6. Conclusions

In this thesis two major technical innovations for measurement procedures of the RF properties of small antennas are presented and evaluated. Firstly, the use of very small measurement chambers for measurements of radiation characteristics is investigated. The GTEM cell - representing the group of guided-wave environments - , and small anechoic chambers - representing the group of 'zero-mode' or free-space environments -, open the way towards a table-top size measurement chamber for inexpensive and relatively quick measurements of small antennas and mobile-handset prototypes, with the possibility to include a phantom head in the measurement set-up. This way the high costs and inconveniences of using large anechoic chambers can be avoided. Especially during the design process of a new handset antenna, but also when a prototype of a mobile handset is available the radiation characteristics such as the radiation pattern, efficiency or bandwidth of the antenna-handset combination need to be determined to optimise its performance. What makes measurements of small antennas more important than those of their larger counterparts is the design process of small antennas. For large antennas typically well-known reference-book design approaches are used. For the complex platform of a small antenna mounted on a mobile handset no standard design approaches are available. In fact, small antennas are often not conceptionalised on the drawing board but instead by experimental methods, optimising the antenna performance in computer simulations or with help of measurements of several proto-types. By using unconventionally small anechoic chambers as described in this thesis it is possible to perform quick measurements of small antenna characteristics in decentralised, or even portable table-top sized measurement environments situated close to the developers of new antennas. Hereby, faster assessment of the behaviour of the mobile handset in operation is possible. The applicability of the GTEM cell to small-antenna measurements with certain restrictions is verified by several measurements of small antennas. The feasibility of decreasing the size of small anechoic chambers to table-top size is shown by a theoretical investigation of the effects of bringing measurement antenna and AUT, as well as sidewalls and AUT very close to one another. Furthermore, a small anechoic chamber W × L × H = 2.50 m × 2.50 m × 2.40 m was designed, constructed and evaluated by measurements of the field-homogeneity in the chamber, as well as performing small-antenna measurements and comparing the obtained radiation characteristics to those obtained in two large anechoic chambers. Several figures of merit show that small-antenna measurements in the small chamber do not result in a higher uncertainty than those obtained in standard commercial large anechoic chambers.

The second innovation presented in this thesis is a multi-frequency balun that provides an improved means to decrease the uncertainty caused by RF feed cables. The cabling can cause considerable errors in the measurements of the radiation characteristics of small antennas not only in large and small anechoic chambers, but also during near-field scans and SAR measurements. During radiation-pattern measurements performed during this work with a small antenna mounted on ground plane with the size of a typical mobile handset, large perturbations in the far-field

pattern of the handset were observed. The perturbations are caused by the RF feed cable attached to the handset through *a)* stray currents on the surface of the cable, and *b)* scattered fields from the cable. Also in near-field measurements such as surface-current scans the effect of the attached feed cable was noticed. In near-field scans along the surface of the above-mentioned handset prototype it could be clearly seen how the cable shield acts as a current drain for the surface currents on the AUT. A common method to suppress those surface currents is the use of several ferrite chokes along the cable. An improved solution to this problem is presented, based on a sleeve-like balun placed on the RF feed cable of a mobile handset. The balun blocks the parasitic currents and thus reduces the perturbations at a frequency range of about 10%. A novel dual-frequency balun design is presented for the centre frequencies 920 MHz and 1795 MHz. The dimensions of the balun were optimised with help of computer simulations. The results obtained from computer simulations and from measurements with the dual-band handset prototype show that despite of its limited bandwidth such a balun is very useful to suppress parasitic currents on the RF feed cable during measurements of the radiation characteristics. Because of the dual-band capability of the presented balun, also frequency-swept measurements of dual-frequency antennas are possible. It was shown that with a balun the errors in the measured gain and efficiency, and the uncertainty of far-field and near-field measurements decreases significantly over a bandwidth of about 10% at both centre frequencies. Also, within those frequency bands the balun decreases the measurement uncertainty significantly better than the ferrite chokes. Nevertheless, ferrite chokes can be a useful measure supplementing the balun. Both measurements and computer simulations show that the usage of two baluns of the same kind in a row, or of several additional ferrites along the RF cable beyond the balun clearly reduces further the effect of scattering by the RF cable when it is exposed to the radiated fields of the AUT.

References

[1] K. Kalliola, H. Laitinen, L.I. Vaskelainen, P. Vainikainen, “Real-time 3-D spatial-temporal dual-polarized measurement of wideband radio channel at mobile station”, *IEEE Transactions on Instrumentation and Measurement*, Vol. 49, No. 2, 04/00, pp. 439 –448.

[2] T. Taga, “Analysis for mean effective gain of mobile antennas in land mobile radio environments”, *IEEE Transactions on Vehicular Technology*, vol. 39, No. 2, 05/90, pp. 117–131.

[3] “IEEE Standard Test Procedures for Antennas,” *ANSI/IEEE Std. 149-1979*, IEEE Press, New York, NY, 1980, 143 pages.

[4] R.C. Johnson, H. Jasik, *Antenna Engineering Handbook*, 2nd Ed., McGraw-Hill, New York, 1961.

[5] W.L. Stutzman, G.A.Thiele, *Antenna Theory and Design*, J. Wiley and Sons, New York, 1981.

[6] H. Arai, *Measurement of Mobile Antenna Systems*, Boston, Artech House, 2001, 214 p.

[7] H.-O. Ruoss and F. M. Landstorfer, “Measurement techniques for the investigation of hand-held mobile telephones considering the user's influence”, *Proc. of the MIOP'97*, Mikrowellen und Optronik, 9. Kongreßmesse für Hochfrequenztechnik, Funkkommunikation und elektromagnetische Verträglichkeit, Sindelfingen, 04/97, pp. 285-289.

[8] J.E. Hansen et al., “Spherical Near-Field Antenna Measurements”, *IEE Electromagnetic Waves Series 26*, London, UK, 1988, 387 p.

[9] A. D. Yaghjian, "An Overview of Near-Field Antenna Measurements", *IEEE Transactions on Antenna and Propagation*, Vol. AP-34, No. 1, Jan. 1986, pp. 30-45.

[10] A. Drossos, V. Santomaa, N. Kuster, “The dependence of electromagnetic energy absorption upon human head tissue composition in the frequency range of 300-3000 MHz”, *IEEE Transactions on Microwave Theory and Techniques*, Vol. 48, No. 11, Part 2, 11/00, pp.1988 - 1995

[11] A. Schiavoni, P. Bertotto, G. Richiardi, P. Bielli, “SAR generated by commercial cellular phones-phone modeling, head modeling, and measurements”, *IEEE Transactions on Microwave Theory and Techniques*, Vol. 48, No. 11 Part: 2 , Nov. 2000 pp. 2064 –2071.

[12] International Commission on Non-Ionizing Radiation Protection, “Health issues related to the use of hand-held radiotelephones and base transmitters,” *Health Physics*, Vol. 70(4), 4/96, pp. 587–593.

[13] IEEE Standard for Safety Levels with Respect to Human Exposure to Radio Frequency Electromagnetic Fields, 3 kHz to 300 GHz, *ANSI/IEEE Standard C95.1 1999 Edition*, 4/99.

[14] H. A. Wheeler, "The radiansphere around a small antenna," *Proceedings of the IRE*, Vol. 47, Aug. 1959, pp. 1325-1331.

[15] R. H. Johnston, J. G. McRory, “An improved Small Antenna Radiation-Efficiency Measurement Method,” *Antennas and Propagation Magazine*, Vol. 40, No. 5, 10/98, pp. 40 - 48.

[16] K. Rosengren, P-S Kildal, J. Carlsson, O. Lunden, "Measurement of terminal antennas performance in multimode reverberation chambers", *Proceedings of Nordic Antenna Symposium Antenn'00*, Lund, Sweden, 9/00, pp. 159 – 164.

[17] J. Krogerus, “Evaluation of Three Methods for Measuring Total Radiated Power of Handset Antennas”, *Proceedings of the Instrumentation and measurement technology conference, IMTC’01*, Budapest, Hungary, 05/01, p. 1005 – 1010.

[18] K. Rosengren, P.S. Kildal, C. Carlsson and J. Carlsson, ”Characterization of antennas for mobile and wireless terminals by using reverberation chambers: Improved accuracy by platform stirring”, *IEEE AP-S International Symposium Digest*, Boston, 7/01, pp. 350 – 354.

[19] P. Hallbjorner, K. Madsen, ‘Terminal antenna diversity characterisation using mode stirred chamber’, *Electronics Letters*, Vol. 37, No. 5, 03/01, pp. 273 – 274.

[20] G.F. Pedersen, J.O. Nielsen, K. Olesen, I.Z. Kovacs, “Measured variation in performance of handheld antennas for a large number of test persons”, *Digest of the 48th IEEE Vehicular Technology Conference*, VTC’98, Vol. 1, 05/98, pp. 505 – 509.

[21] G. E. Evans, *Antenna Measurement Techniques*, Artech House, 1990, 229 p.

[22] J. Krogerus, K. Kiesi, V. Santomaa, “Anechoic chamber with easily removable 3D radiation pattern measurement system for wireless communications antennas”, *Proceedings of AMTA 2000*, Philadelphia, 10/00, pp. 31 – 36.

[23] P. Vainikainen, J. Ollikainen, O. Kivekäs, I. Kelander, ”Performance analysis of small antennas mounted on mobile handset”, *COST 259 Workshop*, Bergen, Norway, 4/00, 8 p.

[24] P. Vainikainen, J. Ollikainen, O. Kivekäs, I. Kelander “Effects of Phone Chassis on Handset Antenna Performance”, *Helsinki University of Technology Radio Laboratory Report*, 3/00, ISBN 951-22-4928-6, 13 p.

[25] J. DeMarinis, “The antenna Cable as a Source of Error in EMI Measurements”, *Proceedings 1988 IEEE Int’l Symposium on EMC*, Seattle, Washington, 8/88, pp. 9-14.

[26] S. Saario, D.V. Thiel, J.W. Lu, S.G. O’Keefe, “An assessment of cable radiation effects on mobile communications antenna measurements”, *Proceedings of the 1997 IEEE Int’l Symposium Antennas and Propagation*, Montreal, Canada, 7/97, pp. 550-553.

[27] O. Staub, J.-F. Zurcher, and A. Skrivervik, “Some considerations on the correct measurement of the gain and bandwidth of electrically small antennas”, *Microwave and Technology Letters*, Vol. 17, No. 3, 02/98, pp. 156 –160.

[28] S.A. Saario, D.V. Thiel, S.G. O'Keefe, J.W. Lu, “Analysis of ferrite beads for RF isolation on straight wire conductors”, *Electronics Letters*, Vol. 33, No. 16, 07/97, pp. 1359-1360.

[29] K. Sulonen, P. Vainikainen, "Effects of antenna radiation pattern on the performance of the mobile handset", *IEEE AP-S Int'l Symposium Digest*, Boston, 07/01, pp. 354 – 357.

[30] M. D. Migliore, F. Soldovieri, R. Pierri, “Far-field antenna pattern estimation from near-field data using a low-cost amplitude-only measurement setup”, *IEEE Transactions on Instrumentation and Measurement*, Vol. 49, No. 1, 02/00, pp. 71 – 76.

[31] R. Pierri, G. D'Elia, F. Soldovieri, “A two probes scanning phaseless near-field far-field transformation technique”, *Transactions on Antennas and Propagation*, Vol. 47, No. 5, 05/99, pp. 792 – 802.

[32] N.A. Rabou, H. Ikeda, H. Yoshida, S. Shinohara, “Optical fiber wideband RF signal transmission system for remote data sensing”, *Proceedings of the Instrumentation and Measurement Technology Conference*, Irwin, California, 5/93, pp. 777 -780.

[33] C. Laliew, X. Zhang, A. Gopinath, “Linearized optical directional-coupler modulators for analog rf/microwave transmission systems”, *Microwave Symposium Digest*. 2000 IEEE MTT-S International Symposium, Vol. 3, 06/00, pp. 1829 –1832.

[34] J.L. Lasserre et al, “Characterisation of portable communication systems by means of near-field techniques”, *SPIE Proc. Ser.*, 7/95, San Diego, California, Vol. 2556, pp. 50 – 58.

[35] J.C. Aquino, T. Kawashima, M. Tokuda, “Evaluation of anechoic chamber characteristics using optically driven equipment under test”, *Proc. of the 1999 IEEE International Symposium on Electromagnetic Compatibility*, Vol. 1, 8/99, Seattle, Washington, pp. 231 – 233.

[36] A. Stöhr, K. Kitayama, D. Jäger, "Full-Duplex Fiber-Optic RF Subcarrier Transmission Using a Dual-Function Modulator/Photodetector", IEEE Ttrans. on Microwave Theory and Techniques, Vol. 47, No. 7, 7/99, pp. 1338 – 1341.

[37] J.P. Phillips, E.L. Krenz, "Spherical-scan near-field chamber for cellular phones", *Proc. of AMTA'98*, 10/98, Montreal, Canada, pp. 37 – 42.

[38] Y.L. Chow, K.F. Tsang, and C.N. Wong, "An accurate method to measure the antenna impedance of a portable radio", Microwave and Optical Technology Letters, Vol. 23, No. 6, 12/99, pp. 349-352.

[39] C. Icheln, J. Ollikainen, P. Vainikainen, "Reducing the influence of feed cables on small antenna measurements", *Electronics Letters*, Vol. 35, No. 15, 7/99, pp. 1212 – 1214.

[40] C. Icheln, M. Popov, P. Vainikainen, S. He, "Optimal reduction of the influence of RF feed cables in small antenna measurements", *Microwave and Optical Technology Letters*, Vol. 25, No. 3, 5/00, pp. 194-196.

[41] C. Icheln, P. Vainikainen, "Dual-frequency balun to decrease influence of RF feed cables in small-antenna measurements", *Electronics Letters*, Vol. 36, no. 21, 10/00, pp. 1760-1761.

[42] S. Hawlitschka, W. Graf, P. Guidi, H.U. Schmidt, "Untersuchungen des Abstrahlverhaltens von Antennen und Störstrahlern in TEM-Wellenleitern," *Digest of the 5th International Fair and Congress for Electromagnetic Compatibility*, Karlsruhe, Germany, February, 1996, pp. 301 - 308.

[43] E. L. Bronaugh, J.D.M.Osburn, "Measuring Antenna Parameters in a GHz Transverse Electromagnetic (GTEM) Cell," *Proceedings of the 1992 IEEE AP-S International Symposium, URSI, & NEM*, Chicago, IL, July, 1992, pp. 2064 - 2066.

[44] C. Icheln, P. Haapala, P. Vainikainen, "Application of a GTEM cell to small antenna measurements", *Proceedings of the 1997 IEEE AP-S International Symposium and URSI North American Radio Science Meeting*, Montreal, Canada, 7/97, pp. 546 – 549.

[45] P. Erätuuli, P. Haapala, P. Vainikainen, "Dual frequency wire Antennas," *Electronics Letters*, vol. 32, No. 12, 6/96, pp. 1051 – 1052.

[46] P. Erätuuli, P. Vainikainen, P. Haapala, H. Rekonen, "Performance of Internal Handset Microstrip Antennas," *Proc .of the IEEE VTS 46th Vehicular Technology Conference*, Atlanta, Georgia, USA, April 28-May 1, 1996, pp. 344 – 347.

[47] R. De Leo, T. Rozzi, C. Svara, L. Zappelli, "Rigorous analysis of the GTEM cell," *IEEE Transactions on Microwave Theory and Techniques*, Vol.39, No.3, March, 1991, pp. 488 - 499.

[48] C. Icheln, "*The construction and application of a GTEM cell"*, Diploma Thesis at the University of Technology Hamburg-Harburg, 11/95, 53 p.

[49] C. Icheln, J. Ollikainen, P. Vainikainen, "The Effects of RF Absorbers on Measurements of Small Antennas in Small Anechoic Chambers", *Proceedings of the IEEE Instrumentation and Measurement Technology Conference*, Venice, Italy, 5/99, pp. 209 – 212.

[50] C. Icheln, J. Ollikainen, P. Vainikainen, "The Effect of RF Absorbers in the Vicinity of Small Antennas", *Microwave and Optical Technology Letters,* Vol. 22, No. 5, 9/99, pp. 328 – 330.

[51] M. Klingler, J. Rioult, J-P. Ghys, S. Ficheux, "Wideband Total Radiated Power Measurements of Electronic Equipment in TEM and GTEM Cells", *Proceedings of the 13th International Zurich Symposium on EMC*, Zurich, Switzerland, February, 1999, pp. 665 – 670.

[52] D. Green, D. Smith, "Design, construction and performance of a small, low cost anechoic measuring system for research applications," *Proceedings of the 1995 IEEE AP-S International Symposium*, Newport Beach, California, June, 1995, pp. 1738 - 1741.

[53] C.A. Balanis, *Antenna Theory, Analysis and Design*, 2nd Edition, John Wiley & Sons, 1997, 790 p.

[54] T. Macnamara, *Handbook of Antennas for EMC*, Artech House, 9/95, 275 p.

[55] J.D. Kraus, *Antennas*, 2nd Edition, New York, McGraw-Hill Book Company, 3/88, 892 p.

[56] J.S. Hollis, T.J. Lyon, L. Clayton, *Microwave Antenna Measurements*, 2nd ed., Scientific Atlanta, July 1970, p. 14 – 10.

[57] *Emerson&Cuming home page*, www.eccosorb.com/catalog/anechoic/vhp.asp (October 2001)

[58] H. Anzai, M. Saikawa, Y. Naito, T. Mizumoto, "The equivalent representation of pyramidal absorbers and its application to the analysis of electromagnetic wave absorber's characteristics", *Proc. of the 1995 IEEE International Symposium on EMC*, Atlanta, GA, 8/95, pp. 563 – 567.

[59] J. Ollikainen, O. Kivekäs, A. Toropainen, P. Vainikainen, "Internal dual-band patch antenna for mobile phones", *Proc. of the AP2000 Millenium Conference on Antennas & Propagation,* Davos, Switzerland, April 9-14, 2000, CD-ROM SP-444 (ISBN 92-9092-776-3), paper p1111.pdf.

[60] K. Hirasawi, M. Haneishi, *"Analysis, Design, and Measurement of Small and Low-Profile Antennas"*, Artech House, Boston, 1992, pp. 246 – 248.

[61] S. M. Rao, D. R. Wilton, A.W. Glisson, "Electromagnetic Scattering by Surfaces of Arbitrary Shape", *IEEE Trans Antennas Propagat*, Vol. 30, No. 3, 1982, pp. 409 – 418.

[62] S. M. Rao, "*Electromagnetic scattering and radiation of arbitrarily shaped surfaces by triangular patch modelling"*, Ph.D. dissertation, Univ. Mississippi, 8/80.

[63] S. He, J. Cao, "Scattering from a bi-isotropic object of arbitrary shape", *J. Electromagnetic Waves and Applications*, Vol.12, 1998, pp. 1547 – 1574.

[64] D. E. Goldberg, *Genetic Algorithms in Search*, *Optimization and Machine Learning, Reading*, MA, Addison-Wesley, 1989.

[65] D. S. Weile, E. Michielssen, "Genetic Algorithms Optimization applied to Electromagnetics: a review", *IEEE Trans. Antennas Propagat*, Vol. 45, No 3., 1997, pp. 343 – 353.

[66] R. L. Haupt, "An introduction to Genetic Algorithms for Electromagnetics", *IEEE Antennas and Propagat*. *Mag.* , Vol. 37, No. 2, 1995, pp. 7 – 15.

[67] C.A. Jones, "Permittivity and Permeability Measurements Using Stripline Resonator Cavities — A Comparison", Trans. on Instrumentation and Measurements, vol. 48, no. 4, 8/99, pp. 843 – 848.

[68] E.K. Miller, "PCs for AP and other EM reflections", Antennas & Propagation Magazine, Vol. 42, No. 6, 12/00, pp. 92 – 98.